Controlling electron quantum dot qubits by spin-orbit interactions

Dissertation

zur Erlangung des Doktorgrades
der Naturwissenschaften (Dr. rer. nat.)
der Naturwissenschaftlichen Fakultät II-Physik
der Universität Regensburg

vorgelegt von

Peter Stano
aus Partizanske, Slowakei
Januar 2007

The PhD thesis was submitted on 12.01.2007.

The colloquium took place on 23.3.2007.

Board of examiners:

Christoph Strunk	Chairman
Jaroslav Fabian	1st Referee
Milena Grifoni	2nd Referee
Andreas Schaefer	Examiner

Acknowledgments

I would like here to express my gratitude to Prof. Jaroslav Fabian for his invalueable help and support over the whole period of my PhD studies. Without his continual assistance this work would not get much farther than to this page.

Contents

List of Tables

List of Figures

Publications

1. P. Stano and J. Fabian: Spin-orbit effects in single-electron states in coupled quantum dots, Phys. Rev. B 72, 155410 (2005).

2. P. Stano and J. Fabian: Orbital and spin relaxation in single and coupled quantum dots, Phys. Rev. B 74, 045320 (2006).

3. P. Stano and J. Fabian: Theory of phonon-induced spin relaxation in laterally coupled quantum dots, Phys. Rev. Lett. 96, 186602 (2006).

4. P. Stano and J. Fabian: Control of electron spin and orbital resonance in quantum dots through spin-orbit interactions, (submitted to Phys. Rev. B), cond-mat/0611228.

Chapter 1

Introduction

Electron confined in a semiconductor quantum dot is a promising system for potential applications in quantum information processing. The vast progress in semiconductor technology over last fifty years has made it possible to manufacture and manipulate systems small enough to reveal their quantum nature. Especially the spin degree of freedom in quantum dots has attracted attention for two reasons. First, the electron spin provides a natural quantum two level system, suitable for encoding the information bit. Second, the spin is less coupled to the environment than are electron orbital degrees of freedom, thus providing longer coherence time. This is crucial for a quantum processor to work – the time it takes to do a desired manipulation, such as a controlled spin flip, has to be much smaller than a time after which the information initially encoded in the spin is lost in the environment.

Up to now the best experimental achievements show we are still far away from the desired goal of controlling the quantum dot spin qubit to the extend that it can serve as a qubit in a quantum computer. The problem is that when a system is decoupled from the environment (such as the spin in a quantum dot), and consequently the leak of the information is slow, it is also decoupled from possible means of control, making the manipulation time long. And vice versa – a system which is easy to manipulate, since it is strongly coupled to the outside world, is also strongly coupled to all kinds of fluctuations out of our control.

This work follows an idea specific to semiconductor quantum dot spin qubits, where the information is stored in the electron spin, which is decoupled from the fluctuations to a large degree. Easily accessible orbital degrees of freedom are used for a spin manipulation. This manipulation is possible due to spin-orbit interactions, present in certain semiconductor structures, which couple spin and orbital parts of the electron wavefunction. We study the influence of spin-orbit interactions on various properties (energy spectrum, relaxation rates, and frequency of induced coherent oscillations) of a single electron quantum dot qubit, having in mind a possible exploitation of the spin-orbit as a mean of control over the electron spin.

In the first part, we study the energy spectrum of the quantum dot. The differences of eigenenergies give frequencies of inherent oscillations of eigenstate superpositions (such as tunneling in symmetric double quantum dots, or spin precession in magnetic field). Resonant frequencies in manipulation of the states by resonant oscillating field techniques (Rabi oscillations) are also given by the eigenenergies. Apart from the possibility of tuning these frequencies by the spin-orbit interactions, more importantly, the spin-orbit interactions make such frequencies spin dependent. This can be used, for example, for spin manipulations or spin to charge conversion schemes.

Second area of our research is the electron relaxation time induced by phonons, where spin-orbit plays important role. From the perspective of quantum computation, it is desired to keep the relaxation (and even more importantly the decoherence) time as large as possible. The anisotropy of the spin-orbit interactions leads to a modulation of the relaxation time. The goal is to specify conditions, when the relaxation time is maximal.

Third, we inspect the role of the spin-orbit interactions in a coherent manipulation of an electron by resonant oscillating fields. Similarly as before, the anisotropy of the spin-orbit interactions can be used to control the effectiveness of electric and magnetic fields in spin and orbital electron manipulations.

Throughout our work we pay special attention to spin hot spots, which are anti-crossings induced by the spin-orbit interactions. The reason is that the electron wavefunction is drastically changed at such anti-crossings. More precisely, the spin orientation of the anti-crossing states is qualitatively different compared to other states. This has profound consequences on all kinds of spin dependent characteristics of the system, for example, the spin relaxation is enormously enhanced at spin hot spots.

We describe the single electron in a GaAs/AlGaAs quantum dot using the effective mass approximation. The lowest spin dependent corrections, due to couplings to other bands, are included in form of the Bychkov-Rashba and cubic and linear Dresselhaus spin-orbit Hamiltonians. When considering phonons, we describe them as bulk plane waves, while including deformation and piezoelectric potentials of acoustic phonons for the electron-phonon interaction. The resonant oscillating electromagnetic fields are described as classical monochromatic waves. We do all the computation numerically using an exact diagonalization technique (Lanczos diagonalization), fast Fourier transform, and numerical integration. Apart from that, we derive analytical formulas using suitable approximations. Several problems we address were already studied in single dots; however, the exact numerical technique we use allows us to study them also in double dots, without relying on the Fock-Darwin solutions, being usually the basis chosen by other authors.

In the following three chapters we will discuss the role of the spin-orbit interactions in three main areas we studied: energy spectrum, relaxation rates, and

Rabi oscillations induced by resonant fields. The last chapter gives conclusions and a discussion of possible extensions of the work.

Chapter 2

Spectrum of a single electron quantum dot

In this chapter we study the energy spectrum of a single electron in single and double quantum dots in zero and finite perpendicular magnetic field. We first introduce the effective mass approximation that allows us to use a single particle description. We comment on the origin of spin-orbit interactions, stemming from this approximative description. Taking an explicit model of GaAs/AlGaAs quantum dot, we shortly review the most interesting results of other authors, after what we present our contribution. There we first study the spectrum of a single dot, concentrating on the spin-orbit influence on the g-factor. We then continue with a similar analysis of the double dot, separately in zero and finite magnetic field. Here we focus on the spin-orbit influence on the g-factor and the tunneling energy. We construct an effective tunneling Hamiltonian which incorporates the results in a simple form. At the end we derive an effective spin-orbit Hamiltonian and perturbative eigenfunctions which will be used in next chapters.

2.1 Electron in a quantum dot: Single particle approximation

2.1.1 Effective mass approximation

Let us consider a semiconductor with an electron which is free (that is, it is not bound to a certain atom). One supposes that the influence of crystal atoms and other electrons can be attributed to an effective crystal potential V_C, in which the electron moves. The wavefunction of the electron is then given by this crystal potential. The most general property of the wavefunction is that it is of the Bloch form, a fact which follows from the periodicity of the crystal and consequently of the potential V_C. One can suppose that the Bloch functions and their energies are known – detailed band structure calculations have been done for many bulk

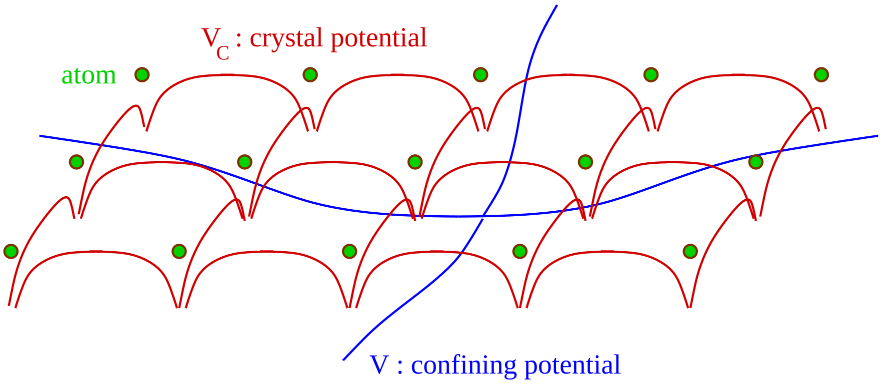

Figure 2.1: Microscopic potential in a quantum dot. The crystal potential V_C has the periodicity of the crystal. The confinement potential V has a local minimum, where an electron can be captured. The characteristic length of the confinement potential is much larger than the period of the crystal.

semiconductor materials.[7]

If the electron is confined to a certain region by an additional confinement potential V, as illustrated in Fig.2.1, one talks about a quantum dot. The confining potential V can be of various origins, such as an electric potential of metallic gates on the surface of the semiconductor, a charged impurity bonding the electron, or a different material composition of the confinement region. The confinement potential V is not periodic as V_C is, and only approximate solutions of the total Hamiltonian with the potential $V_C + V$ can be found. The effective mass approximation[13] exploits the fact that the period of the crystal potential is much smaller than the characteristic length of the confinement potential (a length over which the confinement potential changes appreciably). The total electron wavefunction can be in this case approximated by a product of a Bloch function $\xi_{\mathbf{k},n}(\mathbf{r})$ with a fixed momentum and band index, and a modulating envelope function $\Psi(\mathbf{r})$. An effective Hamiltonian can be then derived for the envelope function, in which the crystal potential is present only through a redefinition of the mass of the electron:

$$H = \frac{1}{2m}\mathbf{p}^2 + V, \tag{2.1}$$

here m is the effective electron mass which is different from the free electron mass m_e.

Equation (2.1) is called single band, since the electron is described as a two component spinor. A generalization of the single band effective mass approximation is the multi-band $\mathbf{k}.\mathbf{p}$ theory, where the quickly oscillating Bloch part of the electron wavefunction is still not present explicitly, but more bands are taken into account and the electron is described by a vector of envelope functions for which an effective matrix Hamiltonian equation is derived. From such a description, the influence of couplings between different Bloch bands through the potential

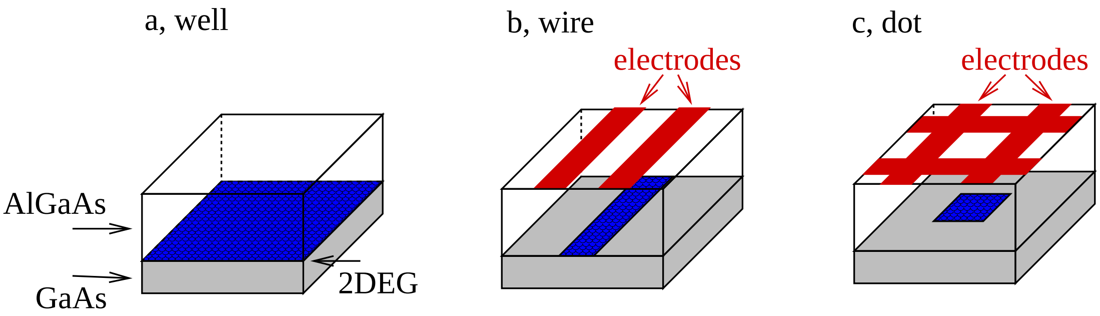

Figure 2.2: a, Quantum well: At the heterostructure interface a two dimensional electron gas (2DEG) is formed. By confining electrons further b, a quantum wire and c, a quantum dot is formed.

V can be obtained perturbatively. These couplings lead to a change of the band structure compared to the bulk; for example, degenerate bands are split. In the context of this work, an important consequence of the band couplings is the appearance of spin-dependent interactions in the effective electron Hamiltonian. Using 14×14 Kane model in bulk GaAs (that is considering 7 bands, each for the two spin indexes), one can derive the Dresselhaus spin-orbit Hamiltonian.[168] The Dresselhaus Hamiltonian is the lowest order (in momentum operator) spin-dependent interaction appearing in the conduction band effective Hamiltonian for material without bulk inversion symmetry (such as GaAs, a III-V compound, it is not present in Si). Higher order corrections can be derived,[26] these however play only a minor role near the band minimum.

Further step that we make in the approximative description of the electron is considering a heterostructure. A heterostructure is a composition of two different materials (such as GaAs and AlGaAs) on top of each other – the interface is a plane perpendicular to z direction. Due to different band gaps, a steep potential dip with approximately triangular shape is formed along $\hat{z}$. This is a part of the confining potential V. Similarly as for the Dresselhaus interaction, now the asymmetry of the interface potential along $\hat{z}$ leads to another spin-dependent correction – the Bychkov-Rashba spin-orbit interaction. It can be obtained considering the conduction and three valence band in 8×8 Kane model. At the heterostructure interface, the conduction electrons (say the material is doped) form a two dimensional electron gas. They are free to move along $\hat{x}$ and $\hat{y}$, while confined along $\hat{z}$ by the heterostructure – one speaks about a quantum well. The confinement length in $\hat{z}$ is typically a few nanometers, being still large enough for the effective mass approximation to hold. A quantum wire means electrons are confined further, say in x direction (for example, by etching a narrow line from the material or placing gates above). A quantum dot is formed, if the confinement is in both lateral dimensions and electron states are completely spatially localized, see Fig. 2.2.

We will consider the lateral confinement to be achieved by placing metallic gates on the top of the sample, which is typically $\sim$ 100 nm above the two dimensional electron gas at the heterostructure interface. By a voltage applied to the gates it is possible to tune the confinement. In this case the lateral confinement length is typically tens to hundreds nanometers, therefore much larger than the confinement in z direction. We can then approximate the electron states as $\Psi(x,y,z) = \Psi(x,y)\phi_0(z)$, where $\phi_0(z)$ is the ground state of a Hamiltonian with the confinement potential of the heterostructure. In the total Hamiltonian we can then replace all operators dependent on z variable by their expectation values in the ground state: $\hat{O}(z) \to \langle \phi_0(z)|\hat{O}(z)|\phi_0(z)\rangle$ (quantum averaging). Such averaging allows us to describe the electron as two dimensional (2D approximation). The 2D approximation is valid as long as the considered energy of the electron is much smaller than the excitation energy in the z confinement (that is a difference of energies of excited state ϕ_1 and ground state ϕ_0).

Finally, we consider that a magnetic field is applied. It couples to the electron spin through the Zeeman term, where again the strength of the interaction (g-factor) is renormalized from the free electron value through the hidden Bloch function part of the electron wavefunction. Second, the magnetic field enters the momenta operators through the minimal coupling. However, the orbital effects of the in-plane field can be neglected in the 2D approximation, if the in-plane magnetic field is not too high, say ≤ 10 T, for the further used material parameters. It is possible to include the orbital effects of the in-plane field, while keeping the two dimensional description. However this leads to much more complicated form of the spin-orbit Hamiltonians.[62]

Summarizing, under the above discussed approximations the electron confined in a quantum dot can be described by a two dimensional effective Hamiltonian containing the spin-orbit interactions. The basic question is how does the energy spectrum and the states of this Hamiltonian look like? The analytical solution for a general confining potential does not exist. If one is able to solve the Schrödinger equation with the Hamiltonian without the spin-orbit interactions, they can be then treated as a perturbation. Their most important property is that they mix the orbital and spin degrees of freedom, thus changing the spin character of the states and renormalizing the states' energies. The difference of energies of the two spin opposite states is, without the spin-orbit interactions, given by the Zeeman term only. The influence of the spin-orbit interactions can be then described as an effective change of the strength of the Zeeman term, which is denoted as g-factor.

2.1.2 Overview of known results

Most of the existing works quantifying the spin-orbit influence on the quantum dot spectrum work with a harmonic confinement potential, where an analytical solution of the Hamiltonian without the spin-orbit terms exists in the form of Fock-Darwin states[67, 32] with Pauli spin quantized along the magnetic field direction.

Due to the circular symmetry of the confining potential definite rules exist for the coupling of the Fock-Darwin states through the spin-orbit Hamiltonians.[34] The deformations of the parabolic potential, thus loosing the circular symmetry, does not allow for specific selection rules anymore.[155] Symmetry of the parabolic potential causes in zero magnetic field high degeneracy, which is partially lifted by the spin-orbit interactions.[43] The Dresselhaus and Bychkov-Rashba term act independently and the g-factor, comparing to the bulk value, is enhanced if Bychkov-Rashba dominates and suppressed if Dresselhaus terms dominate.[34] The g-factor change is up to several percent for typical spin-orbit strengths in GaAs. A complicated behavior occurs for stronger spin-orbit interactions, or larger magnetic fields, where an anti-crossing is present and the spin structure is disturbed heavily.[42, 43, 156, 34, 40, 161, 108] Spatially dependent spin-orbit interaction induces bounding of the electron also in the absence of any confining potential,[153] and a shallow potential well with only one possible bound state is, in the presence of the spin-orbit interactions, turned into a system with infinitely many possible bound states.[27] The spin-orbit can reveal itself also through the properties of the wavefunction – it was shown that the spin-orbit causes discreet steps in the magnetization.[160]

In zero magnetic field the spin-orbit interactions are not effective in the lowest order of the perturbation theory. It is a consequence of the time reversal symmetry of the spin-orbit Hamiltonians.[158] A unitary transformation (Schieffer-Wolff) was found that explicitly removes the lowest order contribution of the linear spin-orbit terms.[5] A generalization of this transformation in finite magnetic field was found to exist for a specific case of the parabolic potential.[154]

If the potential is a cylindrical hard-wall, the Hamiltonian with only one of the linear spin-orbit terms has analytical solution.[22] The solution in the same potential has been further generalized by allowing for a finite magnetic field.[151] Another strategy in the parabolic potential was followed in Ref. [37] – an analog of the rotating wave approximation leads to a simple analytical solution. With the exception of the analytical solution for a hard-wall, however, all discussed works were based on the Fock-Darwin states, thus applicable only to the case of a parabolic potential, possibly with only small deviations. The parabolic potential is in fact a very good approximation to experimental data from single quantum dots,[150] but perturbation approaches based on Fock-Darwin solutions are not suitable for more general potentials. An example of such is the double dot, where the potential has two symmetric minima.

For a general potential exact diagonalization techniques were used, such as studying the potential profile in a 3D simulated Si device as a function of gate voltage,[132] or 3D simulation of GaAs/AlGaAs device with realistic gates, where few electron ground states were modeled.[166] However such methods lack the simplicity of results obtained using few levels from the Fock-Darwin spectrum.

2.1.3 Parameters of the model

The effective mass Hamiltonian contains several material parameters (effective mass, g-factor, spin-orbit couplings) that have to be obtained from microscopic calculations or measured experimentally. Microscopic calculations are based on the **k**.**p** model where a specific confinement in z direction has to be included.[31, 129, 130, 93, 25, 33] The parameters show a nontrivial behavior as functions of the doping density, material composition, width of the well, or applied electric field. However, the existing calculations neglect the lateral confinement which also influences the effective parameters. It would be therefore desirable to be able to measure the parameters directly for a given quantum dot. Unfortunately this is not a straightforward task, since the parameters' influence on easy measurable quantities is complicated. From the energy spectrum of the quantum dot measured by a resonant tunneling technique,[157] the g-factor can be obtained directly.[103, 131] The effective mass and the strength of the cubic Dresselhaus term are supposed to have the bulk value. The most complicated is to obtain the couplings of the linear spin-orbit terms. In a quantum well they can be fitted from Shubnikov-de Haas oscillations,[122, 57, 84, 85, 79, 141] weak localization,[100, 119, 120, 167] and spin interferometry.[102] Recently, the spin relaxation anisotropy[10] and spin-galvanic effect[73] allowed to find the ratio of the linear spin-orbit couplings in a quantum well. The values obtained here are then used for a quantum dot. Recent measurements of single dot spin relaxation offered a first possibility to fit the strength of the spin-orbit interactions directly from a quantum dot measurement.[118, 6]

2.2 Spin-orbit influence on the energy spectrum

Further in this chapter, we investigate the role of spin-orbit interactions, represented by the Dresselhaus (both linear and cubic) and Bychkov-Rashba terms, in spin and charge properties of two laterally coupled quantum dots based on GaAs materials parameters. We perform numerically exact calculations of the energy spectrum using the method of finite differences. We first study the general structure of the energy spectrum and the spin character of the states of the double dot system. We construct the group theoretical correlation diagram for the single and double dot states and indicate the possible transitions due to spin-orbit interaction. This group theoretical classification is used in combination with Löwdin perturbation theory to explain analytically our numerical results. In particular, we show that while allowed by symmetry, the specific forms of the linear spin-orbit interactions do not lead to spin hot spots in the absence of magnetic field (spin hot spots are nominally degenerate states lifted by spin-orbit interaction[60]). Only the cubic Dresselhaus term gives spin hot spots. If identified experimentally, the strength of the cubic term can be detected.

We next focus on two important measurable parameters: electronic g-factor and tunneling amplitude. In single dots the variation of the effective g-factor with the strength of the spin-orbit interaction has been investigated earlier.[34] The effect is not large, amounting to a fraction of a percent. Similar behavior is found for double dots. In our case of GaAs the contribution to the g-factor from spin-orbit interaction is typically about 1%, due to the linear Dresselhaus term.

More exciting is the prospect of influencing coherent tunneling oscillations between the dots by modulating the spin-orbit interaction strength. Two effects can appear: (i) the tunneling amplitude or frequency can be modulated by spin-orbit interaction and, (ii) the tunneling amplitude can be spin dependent. We show how a naive application of perturbation theory leads to a misleading result that (i) is present in the second order in linear spin-orbit interaction strengths, giving rise to an effective tunneling Hamiltonian involving spin-flip tunneling at zero magnetic field. Both numerical calculations and an analytical argument, presented here, show that this is incorrect and that there is no correction to the tunneling Hamiltonian in the second order of linear spin-orbit terms. The dominant correction in the second order comes from the interference of linear and cubic Dresselhaus terms. We propose to use this criterion, that the corrections due to linear terms vanish in the second order, to distinguish between single and double dots as far as spin-orbit interaction is concerned. Indeed, at very small and very large interdot couplings the states have a single dot character and the correction to energy due to linear spin orbit terms depends on the interdot distance (except for the two lowest states which provide tunneling). We find that dots are "coupled" up to the interdot distance of about five single-dot confinement lengths.

In the presence of magnetic field the time reversal symmetry is broken. The presence of spin-orbit interaction then in general leads to a spin dependent tunneling amplitude. Spin up and spin down states will oscillate between the two dots with different frequencies (for our GaAs dots the relative difference of the frequencies is at the order of 0.1%, but is higher in materials with larger spin-orbit coupling). This leads to a curious physical effect, namely, that of a spatial separation of different spin species. Indeed, starting with an electron localized on one dot, with a spin polarized in the plane (that is, a superposition of up and down spins), after a sequence of coherent oscillations the electron state is a superposition of spin up localized on one, and spin down localized on the other dot. A single charge measurement on one dot collapses the wave function to the corresponding spin state, realizing a spin to charge conversion. There exist several alternative schemes,[53, 135, 76, 88] some of them being pursued experimentally.[52, 82, 81] We construct an effective, four state (two spin and two sites) tunneling Hamiltonian for the single electron double dot system, which takes into effect the above results. Such a Hamiltonian should be useful for constructing realistic model theories of spin dephasing, spin tunneling, and kinetic exchange coupling in coupled quantum dot systems.

2.3 Model

We consider two dimensional electron system confined in a [001] plane of a zinc-blende semiconductor heterostructure, with an additional confinement into lateral dots given by appropriately shaped top gates. A magnetic field $\mathbf{B}$ is applied perpendicular to the plane. We denote the perpendicular component of the magnetic field as $B_\perp$ and in-plane component as $\mathbf{B}_{||}$. In the effective mass approximation the single-electron Hamiltonian of such a system, taking into account spin-orbit interaction, can be decomposed into several terms:

$$H = \underbrace{T + V + H_Z}_{H_0} + \underbrace{H_{BR} + H_D + H_{D3}}_{H_{SO}}. \tag{2.2}$$

Here $T = \mathbf{P}^2/2m$ is the kinetic energy with the effective electron mass m and kinetic momentum $\mathbf{P} = \mathbf{p} + e\mathbf{A} = -i\hbar\nabla + e\mathbf{A}$; e is the proton charge and $\mathbf{A} = B_\perp(-y/2, x/2)$ is the vector potential of $\mathbf{B} = B_\perp \hat{z}$. Only the in-plane components of vectors of position and momentum are relevant, due to the electron being two dimensional. Operators of angular momentum with mechanical and canonical momenta are denoted as $L_z = xP_y - yP_x$ and $l_z = xp_y - yp_x$. The quantum dot geometry is described by the confining potential $V(\mathbf{r})$. Single dots will be described here by a parabolic potential $V = (1/2)m\omega_0^2 r^2$, characterized by confinement energy $E_0 = \hbar\omega_0$ and confinement length $l_0 = (\hbar/m\omega_0)^{1/2}$, setting the energy and length scales, respectively. Coupled double dots will be described by two displaced (along $\mathbf{d}$) parabolas:

$$V = \frac{1}{2}m\omega_0^2[\min(\mathbf{r} - \mathbf{d}l_0)^2 + (\mathbf{r} + \mathbf{d}l_0)^2]; \tag{2.3}$$

the distance between the minima is $2d$ measured in the units of l_0. The Zeeman energy is given by $H_Z = (g^*/2)\mu_B \boldsymbol{\sigma}.\mathbf{B}$, where g^* is the conduction band g-factor, μ_B is the Bohr magneton, and $\boldsymbol{\sigma}$ is a vector of the Pauli matrixes. In order to relate the magnetic moment of electrons to their orbital momentum, we will use dimensionless parameter $\alpha_Z = g^* m/2m_e$, where m_e is the free electron mass, and we also define a renormalized magneton as $\mu = (g^*/2)\mu_B$.

Spin-orbit interaction gives additional terms in confined systems.[168] The Bychkov-Rashba Hamiltonian,[133, 23]

$$H_{BR} = (\tilde{\alpha}_{BR}/\hbar)\,(\sigma_x P_y - \sigma_y P_x)\,, \tag{2.4}$$

appears if the confinement is not symmetric in the growth direction (here $\hat{z}$). The strength $\tilde{\alpha}_{BR}$ of the interaction can be tuned by modulating the asymmetry by top gates. Due to the lack of spatial inversion symmetry in zinc-blende semiconductors, the spin-orbit interaction of conduction electrons takes the form of the Dresselhaus Hamiltonian[47] which, when quantized in the growth direction $\hat{z}$ of

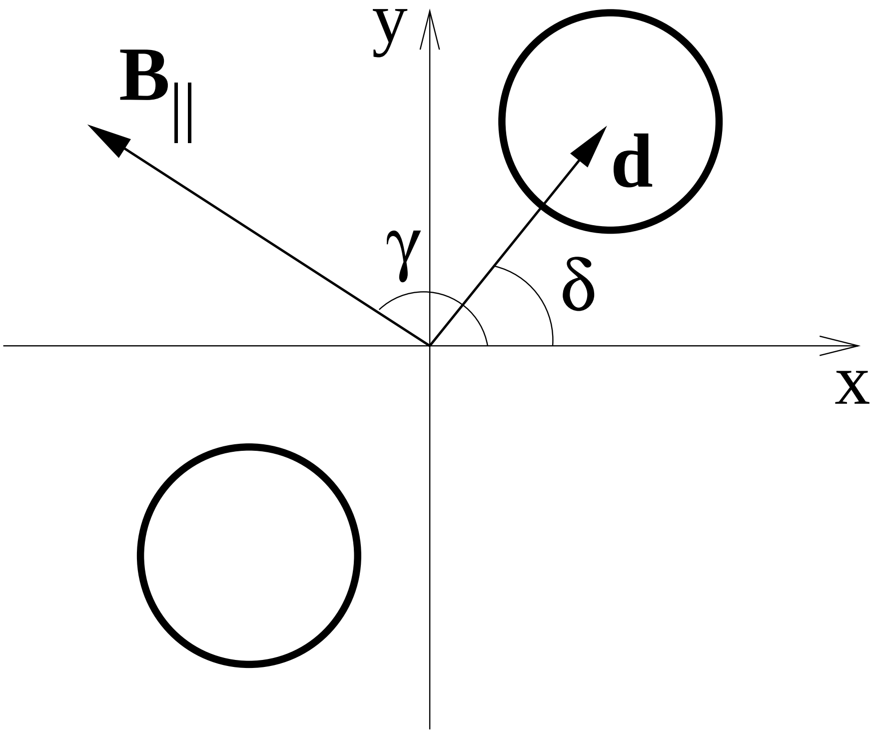

Figure 2.3: The orientation of the potential dot minima (denoted as the two circles) with respect to the crystallographic axes (x = [100] and y = [010]) is defined by the angle δ. The orientation of in-plane component of the magnetic field is given by the angle γ. Throughout this chapter $B_{||} = 0$ and only the perpendicular magnetic field component $B_{\perp}$ can be nonzero.

our heterostructure gives two terms, one linear and one cubic in momentum:[49]

$$\begin{aligned} H_D &= (\gamma_c/\hbar^3)\langle P_z^2\rangle\left(-\sigma_x P_x + \sigma_y P_y\right), & (2.5)\\ H_{D3} &= (\gamma_c/2\hbar^3)\left(\sigma_x P_x P_y^2 - \sigma_y P_y P_x^2\right) + H.c., & (2.6) \end{aligned}$$

where γ_c is a material parameter and *H.c.* denotes Hermitian conjugation. The angular brackets in H_D denote quantum averaging in z direction – the magnitude of H_D depends on the confinement strength. We will denote the sum of the two linear spin-orbit terms by $H_{\rm lin} = H_D + H_{BR}$. The complete spin-orbit interaction is then $H_{SO} = H_{\rm lin} + H_{D3}$. We find it useful to introduce strengths of the individual terms of the spin-orbit interaction in length units. We denote $l_{BR} = \hbar^2/(2m\tilde{\alpha}_{BR})$, $l_D = \hbar^4/(2m\gamma_c\langle P_z^2\rangle)$ for the linear terms, and $l_{D3} = (\hbar^2 l_0^2/2\gamma_c m)$ for the cubic Dresselhaus term.

In our numerical examples we use the confinement length of $l_0 = 20$ nm, which corresponds to the confinement energy $E_0 \approx 2.9$ meV. We further use bulk GaAs materials parameters: $m = 0.067\, m_e$, $g^* = -0.44$, and $\gamma_c = 27.5$ eVÅ^3. For $\langle P_z^2\rangle$ we choose 5.3×10^{-4}Å$^2\hbar^2$, which corresponds to $\gamma_c\langle P_z^2\rangle/\hbar^2 = 14.6$ meV Å. This value of $\langle P_z^2\rangle$ corresponds to the ground state of a 6 nm thick triangular potential well.[34] For $\tilde{\alpha}_{BR}$ we choose a generic value of 4.4 meVÅ, which is in line of experimental observations.[119, 100] The dimensionless parameter of the Zeeman splitting is $\alpha_Z = -0.015$ (expressing it in length units as $\alpha_Z \equiv l_0/l_Z$ would give $l_Z \approx -1.3\mu$m), while the strengths of the spin-orbit interactions in length units are $l_{BR} \approx 1.3\mu$m, $l_D \approx 0.4\mu$m, and $l_{D3} \approx 8\mu$m. Except for anti-crossings, the spin-orbit interaction is a small perturbation to the electronic structure; it is, however, essential for investigating spin structure.

Our analytical calculations will often refer to the Fock-Darwin[67, 32] spectrum, which is the spectrum of Hamiltonian (2.2) for a single dot with $H_{SO} = 0$. The corresponding wave functions Ψ (expressed in polar coordinates r and ϕ), and energies ϵ are

$$\begin{aligned} \Psi_{n,l,\sigma}(r,\phi) &= C\rho^{|l|}e^{-\rho^2/2}L_n^{|l|}(\rho^2)e^{il\phi}\xi(\sigma), & (2.7)\\ \epsilon_{n,l,\sigma} &= \frac{\hbar^2}{ml_B^2}(2n+|l|+1) + B_\perp\frac{\hbar e}{2m}(l+\alpha_Z\sigma), & (2.8) \end{aligned}$$

where $\rho = r/l_B$ is the radius in the units of the effective confinement length l_B, defined by $l_B^2 = l_0^2/\sqrt{(1 + B_\perp^2 e^2 l_0^4/4\hbar^2)}$; n and l are the principal and orbital quantum numbers, respectively, C is the state dependent normalization constant, and $L_n^{|l|}$ are associated Laguerre polynomials. Spinors $\xi(\sigma)$ describe the spin σ state of the electrons. Since the parabolic dot has rotational symmetry in the plane, the states have well defined orbital momentum l and spin σ in the z direction. We also introduce a useful dimensionless measure θ of the strength of the magnetic field induced confinement compared to the potential confinement: $\theta = B_\perp e l_B^2/2\hbar$, $0 < \theta < 1$. The parameter θ gives the number of magnetic flux quanta through a circle with radius l_B. For large magnetic fields $\theta \approx 1 - (2\hbar/Bel_0^2)^2/2$. The confining length can be expressed as $l_B = l_0(1-\theta^2)^{1/4}$.

As it is not possible to solve for the spectrum of Hamiltonian (2.2) analytically, we treat it numerically with the finite differences method using Dirichlet boundary conditions (vanishing of the wave function at boundaries). The magnetic field is included via the Peierls phase: if $H(\mathbf{r}_i, \mathbf{r}_j)$ is the discretized Hamiltonian connecting grid points $\mathbf{r}_i$ and $\mathbf{r}_j$ at $B_\perp = 0$, the effects of the field are obtained by adding a gauge phase: $H(\mathbf{r}_i, \mathbf{r}_j)\exp[i(e/\hbar)\int_{\mathbf{r}_i}^{\mathbf{r}_j}\mathbf{A}.\mathbf{dl}]$. In our simulations we typically use 50 × 50 grid points. The resulting matrix eigenvalue problem is solved by Lanczos diagonalization. The achieved accuracy is about 10^{-5}.

2.4 Single dots

As a starting point we review the effects of spin-orbit interaction in single dots. We are interested in the changes to the spectrum and, in particular, to the magnetic moment of the lowest states, that is, to the effective g-factor. The calculated spectrum of a single dot is shown in Fig. 2.4. There are three ways in which spin-orbit interaction influences the spectrum: (i) First, the levels are shifted, in proportion to l_{SO}^{-2} (by l_{SO} here we mean any of l_{BR}, l_D, or l_{D3}). (ii) Second, the degeneracy at $B_\perp = 0$ is lifted, again in proportion to l_{SO}^{-2} (2.4b). (iii) Finally, at some magnetic field the level crossing of the Fock-Darwin levels is lifted by spin-orbit interaction. The resulting level repulsion is linear in l_{SO}^{-1} (2.4c). The states here are the spin hot spots, that is states in which both Pauli spin up and down species contribute significantly.[60, 21, 43]

The above picture can be understood from general symmetry considerations within the framework of perturbation theory. All spin-orbit terms commute, at $B_\perp = 0$, with the time inversion operator $T = i\sigma_y\hat{C}$, where $\hat{C}$ is the operator of complex conjugation. Therefore Kramer's degeneracy is preserved so that the states are always doubly degenerate. The linear terms can be transformed into each other by a unitary transformation $(\sigma_x + \sigma_y)/\sqrt{2}$ (spin rotation around [110] by π), which commutes with H_0. Therefore the effects on the energy spectrum induced individually by the linear Dresselhaus and the Bychkov-Rashba terms are identical at $B_\perp = 0$. At finite magnetic fields the two interactions give qualitatively different effects in the spectrum, especially for spin hot spots, as discussed below.

For any $B_\perp$ the following commutation relations hold for the linear terms:

$$[H_{BR}, l_z + s_z] = 0, \quad [H_D, l_z - s_z] = 0. \tag{2.9}$$

This means that H_{BR} commutes with the angular momentum, while H_D does not. This will influence the interference between the two terms in the energy spectrum. We can use the Fock-Darwin states as a basis for perturbation theory.

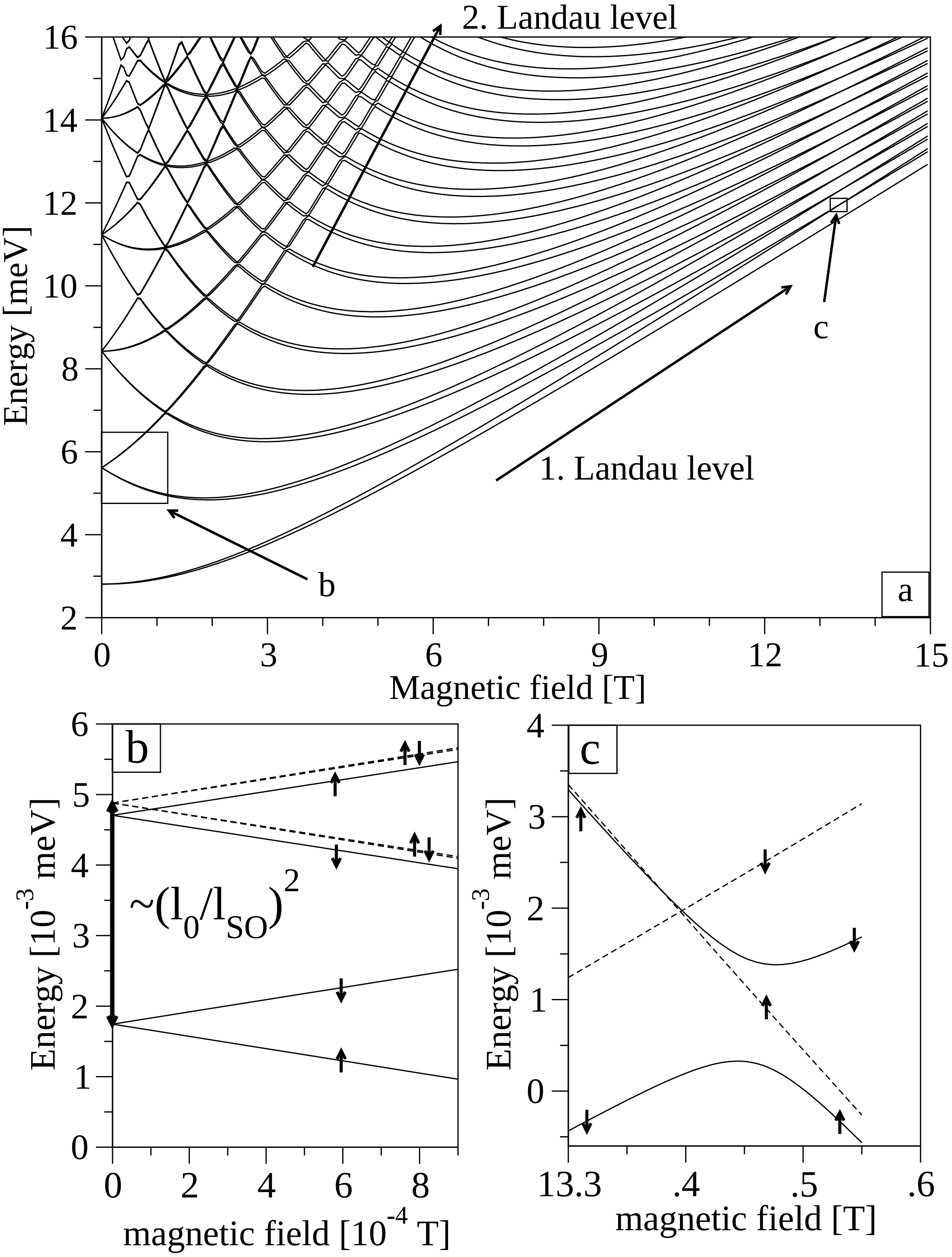

Figure 2.4: Energy spectrum of a single dot in magnetic field. a) The Fock-Darwin spectrum, Eq. (2.8). b) Lowest orbital excited levels ($n = 0$, $|l| = 1$) without (dashed) and with (solid) spin-orbit interaction. Arrows indicate the spin states. For clarity the energy's origin here is shifted relative to case a). Both the shift in energy levels as well as the splitting at $B_\perp = 0$ grow as l_{SO}^{-2}. c) Anti-crossing at the critical magnetic field (here about 13 T). For clarity, a linear trend was subtracted from the data.

Up to the second order the energy of state $|i\rangle = \Psi_{n,l,\sigma}$ is

$$E_i = \epsilon_i + \langle i|H_{SO}|i\rangle + \sum_{j\neq i} \frac{\langle i|H_{SO}|j\rangle\langle j|H_{SO}|i\rangle}{\epsilon_i - \epsilon_j}. \tag{2.10}$$

The first order correction is zero for all spin-orbit terms since H_{SO} contains only odd powers of $\mathbf{P}$ whose expectation values in the Fock-Darwin states vanish. If the perturbation expansion is appropriate, the spin-orbit interactions have a second order (in l_{SO}^{-1}) effect on energy.

Both linear spin-orbit terms couple states with orbital momenta l differing by one. It then follows from the commutation relations (2.9) that H_{BR} preserves the total angular momentum $l+s$, while H_D preserves the quantity $l-s$. As a result, there is no correction to the energy from the interference terms between H_{BR} and H_D in Eq. (2.10): $\langle i|H_{BR}|j\rangle\langle j|H_D|i\rangle = 0$. As for the cubic Dresselhaus term, only the following orbital states are coupled: $(l,\uparrow) \to \{(l+3,\downarrow),(l-1,\downarrow)\}$ and $(l,\downarrow) \to \{(l-3,\uparrow),(l+1,\uparrow)\}$. Due to these selection rules there are no interference terms $\sim H_{D3}H_{BR}$, but terms $\sim H_{D3}H_D$ will contribute to energy perturbation. The Bychkov-Rashba and Dresselhaus Hamiltonians act independently on the Fock-Darwin spectrum (up to the second order).

To gain more insight into the perturbed structure of the spectrum at $B_\perp = 0$, we rewrite Eq. (2.10) using an auxiliary anti-hermitian operator H_{SO}^{op} defined by the commutation relation $[H_0, H_{SO}^{op}] = H_{SO}$. If such an operator exists, the second order correction in (2.10) is then

$$\sum_{j\notin\mathcal{N}} \frac{\langle i|H_{SO}|j\rangle\langle j|H_{SO}|i\rangle}{\epsilon_i - \epsilon_j} = \langle i|\frac{1}{2}[H_{SO}^{op}, H_{SO}]|i\rangle + Re(\langle i|H_{SO}P_{\mathcal{N}}H_{SO}^{op}|i\rangle), \tag{2.11}$$

where $P_{\mathcal{N}}$ is the projector on the subspace $\mathcal{N}$ of the states excluded from the summation. In our case here it is just one state, $\mathcal{N} = \{|i\rangle\}$. The last term in (2.11) then vanishes. The auxiliary operator for H_{D3} is not known and if found, it must depend on the confining potential. Operators for the linear terms are:[5]

$$\begin{aligned} H_D^{op} &= -(i/2l_D)(x\sigma_x - y\sigma_y), &(2.12)\\ H_{BR}^{op} &= (i/2l_{BR})(y\sigma_x - x\sigma_y). &(2.13)\end{aligned}$$

The corresponding commutators are (in the zero magnetic field $\mathbf{P} = \mathbf{p}$, $L_z = l_z$, $\theta = 0$; the last expression will be useful later)

$$\begin{aligned} [H_D^{op}, H_D] &= -\frac{\hbar^2}{2ml_D^2}(1 - \sigma_z L_z/\hbar), &(2.14)\\ [H_{BR}^{op}, H_{BR}] &= -\frac{\hbar^2}{2ml_{BR}^2}(1 + \sigma_z L_z/\hbar), &(2.15)\\ [H_D^{op}, H_{D3}] &= -\frac{\gamma_c}{4\hbar^3 l_D}\Big(\hbar\mathbf{P}^2 + 2\sigma_z[xP_yP_x^2 - yP_xP_y^2 - \\ &\quad -2i\theta(xP_x + yP_y)]\Big) + H.c.. &(2.16)\end{aligned}$$

Because $[H_D^{op}, H_{BR}] + [H_{BR}^{op}, H_D] = 0$, the corrections to the second order perturbation add independently for H_{BR} and H_D (as also noted above from the selection rules), we can introduce $H_{\rm lin}^{op} = H_D^{op} + H_{BR}^{op}$. An alternative route to Eq. (2.11) is to transform the Hamiltonian with[5] $U = \exp(-H_{SO}^{op})$ to $H' = H_0 - (1/2)[H_{SO}, H_{SO}^{op}]$ in the second order of l_{SO}^{-1}. The final result can be also obtained in a straightforward way by using the Thomas-Reiche-Kuhn sum rule in the second order of perturbation theory with the original spin-orbit terms. The resulting effective Hamiltonian is (terms depending on H_{D3} are omitted here)

$$H' = H_0 - \frac{\hbar^2}{4m}\left[l_D^{-2} + l_{BR}^{-2} + \sigma_z L_z (l_D^{-2} - l_{BR}^{-2})/\hbar\right]. \tag{2.17}$$

This Hamiltonian, in which the spin-orbit interaction appears in its standard form, neatly explains point (ii) about the lifting of the degeneracy at $B_\perp = 0$. The levels in Fig. 2.4b, for example, are four fold degenerate ($|l| = 1$, $|\sigma| = 1$) without spin-orbit interaction. Turning on, say, H_D, will split the levels into two groups: energy of the states with $l\sigma > 0$ would not change in the second order, while the states with $l\sigma < 0$ will go down in energy by $\hbar^2/2ml_D^{-2}$, as seen in Fig. 2.4b.

2.4.1 Spin hot spots

Spin hot spots are states formed by two or more states whose energies in the absence of spin-orbit coupling are degenerate or close to being degenerate, while turning on the coupling removes the degeneracy.[60] Such states are of great importance for spin relaxation, which is strongly enhanced by their presence.[61, 21] The reason is that the degeneracy lifting mixes spin up and spin down states and so transitions between states of opposite magnetic moment will involve spin flips with a much enhanced probability compared to normal states.

Figure 2.4c shows an interesting situation where two degenerate levels are lifted by spin-orbit interaction.[43, 21] The lifting is of the first order in l_{SO}^{-1}, unlike the lifting of degeneracy at $B_\perp = 0$ in which case the degenerate states are not directly coupled by H_{SO}. In a finite magnetic field, at a certain value $B_{\rm acr}$, the states of opposite spins and orbital momenta differing by one cross each other, as follows from the equation (2.8). The crossing field is $B_{\rm acr} \approx |\alpha_Z|^{-1/2}\hbar/(el_0^2)$, which is about 13.4 T for our parameters (making the confinement length larger the magnitude of the field would decrease). Spin-orbit interaction couples the two states thereby lifting the degeneracy. For GaAs, where $g^* < 0$, only the Bychkov-Rashba term couples the two states. The Dresselhaus terms are not effective (H_{D3} would introduce such a splitting at $3B_{\rm acr}$). The energy splitting due to H_{BR} is

$$\Delta = c\frac{\sqrt{2}\hbar^2}{ml_0 l_{BR}}|\alpha_Z|^{5/4}, \tag{2.18}$$

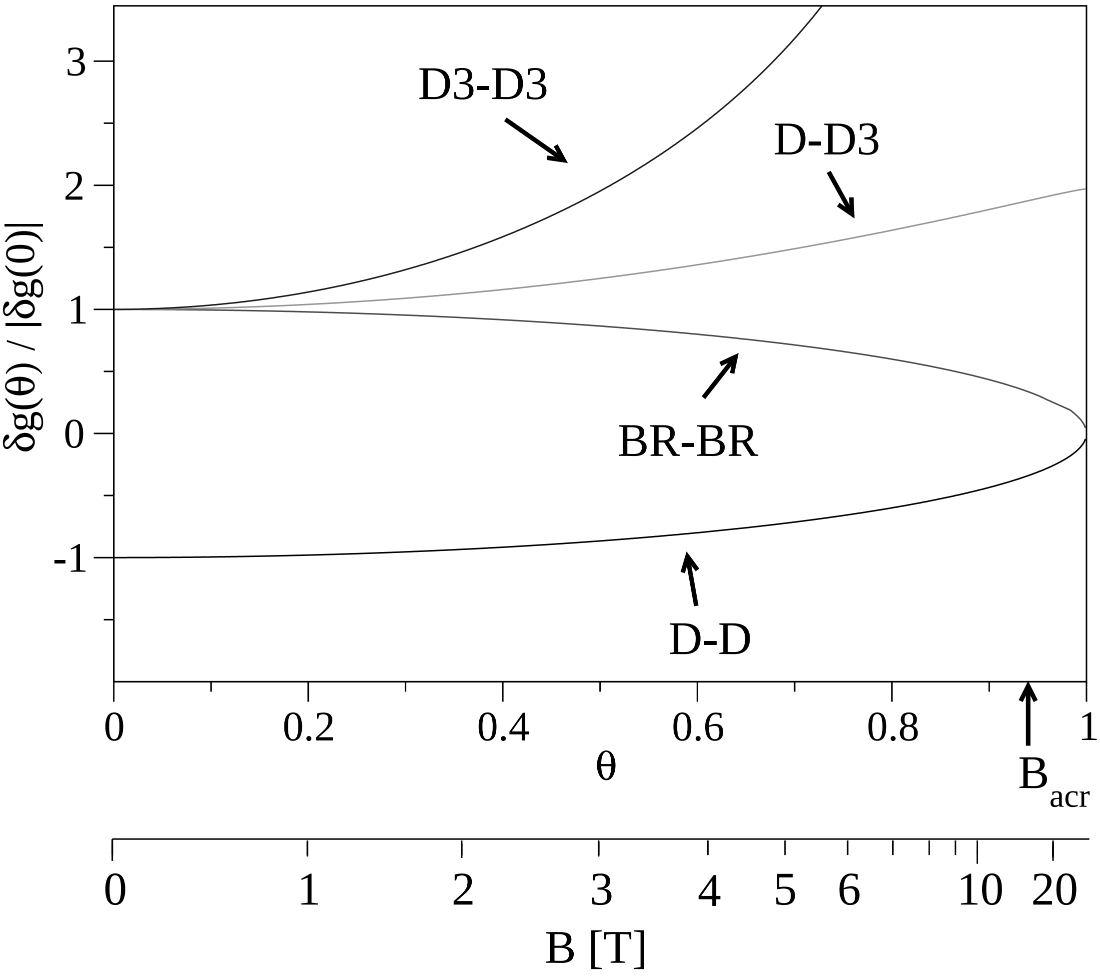

Figure 2.5: Calculated corrections to the effective g-factor by spin-orbit interactions. Formulas (2.19) scaled by the values at $B_\perp = 0$ (and thus independent on l_{SO}) are plotted. The actual numerical values of δg at $B_\perp = 0$ are: $\delta g_{D-D}(0) = 1.0 \times 10^{-2}$, $\delta g_{BR-BR}(0) = 8.6 \times 10^{-4}$, $\delta g_{D-D3}(0) = 9.4 \times 10^{-4}$, $\delta g_{D3-D3}(0) = 2.5 \times 10^{-5}$. At the anti-crossing $\delta g_{D-D}(B_{\rm acr}) = 2.4 \times 10^{-3}$, $\delta g_{BR-BR}(B_{\rm acr}) = 1.0 \times 10^{-4}$, $\delta g_{D-D3}(B_{\rm acr}) = 1.8 \times 10^{-3}$, $\delta g_{D3-D3}(B_{\rm acr}) = 3.4 \times 10^{-4}$.

where c, which is a number of order 1, depends on the quantum numbers of the two states. Since spin hot spots at B_{acr} are due only H_{BR}, the splittings could help to sort out the Bychkov-Rashba versus Dresselhaus contributions. Figure 2.4c shows the calculated level repulsion for states $n = 0, l = 0, \sigma =\downarrow$ and $n = 0, l = -1, \sigma =\uparrow$. The magnitude of Δ, though being linear in l_{BR}, is on the order of 10^{-3} meV and thus comparable to the energy scales associated with quadratic spin-orbit perturbations.

2.4.2 Effective g-factor

When probing spin states in quantum dots with magnetic field, important information comes from the measured Zeeman splitting. We will focus here on the two lowest spin states and calculate the effective g-factor as $g = (E_{0,0,\downarrow} - E_{0,0,\uparrow})/(\mu_B B_\perp)$. If $H_{SO} = 0$, then in our model the effective g-factor equals to the conduction band value g^*. In fact the g-factor is modified by also other confinement effects,[18] but here we consider only spin-orbit interactions. The actual value in the presence of spin-orbit interaction is important for understanding single spin precession in magnetic field, which seems necessary to perform single qubit operations in quantum dots. We have obtained the following contributions to the g-factor from non-degenerate (that is, excluding spin hot spots) second-order perturbation theory [Eq. (2.10)] (for linear spin-orbit terms these are derived also in[34, 156]):

$$\begin{aligned}
\delta g_{D-D} &= -\frac{m_e l_0^2}{2ml_D^2}\frac{\sqrt{1-\theta^2}[1-\theta^2-2(1+\theta^2)\alpha_Z]}{1-\theta^2(1+4\alpha_Z+4\alpha_Z^2)}, \\
\delta g_{BR-BR} &= \frac{m_e l_0^2}{2ml_{BR}^2}\frac{\sqrt{1-\theta^2}[1-\theta^2+2(1+\theta^2)\alpha_Z]}{1-\theta^2(1-4\alpha_Z+4\alpha_Z^2)}, \\
\delta g_{D-D3} &= \frac{2\gamma_c m_e}{\hbar^2 l_D}\frac{(1+\theta^2)[1-\theta^2-2(1+\theta^2)\alpha_Z]}{1-\theta^2(1+4\alpha_Z+4\alpha_Z^2)}, \\
\delta g_{D3-D3} &= \frac{4\gamma_c^2 m m_e}{\hbar^4 l_0^2\theta\sqrt{1-\theta^2}}\left(\frac{2(1-\theta)^2(1+\theta^2)^2}{1-\theta(1+2\alpha_Z)}+\frac{(1-\theta)^4(1+\theta)^2}{3-\theta(1+2\alpha_Z)}+\right. \\
&+ \frac{-3(1-\theta)^6}{3-\theta(3-2\alpha_Z)}+\frac{3(1+\theta)^6}{3+\theta(3-2\alpha_Z)}- -\frac{2(1+\theta)^2(1+\theta^2)^2}{1+\theta(1+2\alpha_Z)}- \\
&- \left.\frac{(1-\theta)^2(1+\theta)^4}{3+\theta(1+2\alpha_Z)}\right). \qquad (2.19)
\end{aligned}$$

Here δg_{A-B} stands for a correction that is proportional to $1/l_A l_B$.

The functions (2.19) are plotted in Fig. 2.5. We can understand the limits of δg at $B_\perp \to \infty$ ($\theta \to 1$) if we notice that in the natural length unit l_B the momentum $P_x = -i\hbar\partial_x - yBe/2 = \hbar l_B^{-1}[-i\partial_{x/l_B} - \theta(y/l_B)]$. In the limit $B_\perp \to \infty$ the matrix elements of H_D, which is linear in P, scale as l_B^{-1}, while the Fock-Darwin energies scale as l_B^{-2}. The second order D-D correction to $E_{0,0,\downarrow} - E_{0,0,\uparrow}$ is thus

magnetic field	SO terms	symmetries of H
$B_\perp = 0$	none	I_x,I_y,I,T,$R_{\mathbf{n}}$
	BR	$-\mathrm{i}\sigma_x I_x$,$-\mathrm{i}\sigma_y I_y$,$-\mathrm{i}\sigma_z I$,T
	$D, D3$	$-\mathrm{i}\sigma_y I_x$,$-\mathrm{i}\sigma_x I_y$,$-\mathrm{i}\sigma_z I$,T
	all	$-\mathrm{i}\sigma_z I, T$
$B_\perp > 0$	none	$-\mathrm{i}\sigma_z I$,R_z
	any	$-\mathrm{i}\sigma_z I$

Table 2.1: Symmetries of the double dot Hamiltonian for different spin-orbit terms present at $B_\perp = 0$ and $B_\perp > 0$. Here $I_x(I_y)$ means reflection $x \to -x$ $(y \to -y)$, $I = I_x I_y$, and $R_z = \exp(-\mathrm{i}\phi\sigma_z/2)$ is the rotation of a spinor by angle ϕ around z-axis; $R_{\mathbf{n}}$ is a spinor rotation around an arbitrary axis $\mathbf{n}$ and T is the time reversal symmetry. The identity operation is not listed.

independent of l_B; it converges to $-(\hbar^2/2ml_D^2)/(1+\alpha_Z)$. The BR-BR correction is analogous, with the limit $(\hbar^2/2ml_{BR}^2)/(1-\alpha_Z)$. To get the g-factor we divide the energy differences by $\mu_B B_\perp$ and get $\delta g_{D-D}\,(\theta \to 1) \propto B_\perp^{-1}$; similarly for H_{BR}. Since H_{D3} scales as l_B^{-3} one gets $\delta g_{D-D3}\,(\theta \to 1) \to 2(\gamma_c m_e/\hbar l_D)/(1+\alpha_Z)$ and $\delta g_{D3-D3}(\theta \to 1) \propto B_\perp$. It seems that for increasing $B_\perp$ there inevitably comes a point where the influence of H_{D3} on the g-factor dominates. But at $B_\perp = B_{\mathrm{acr}}$ there is an anti-crossing of the states $(0,0,\downarrow)$ and $(0,-1,\uparrow)$ so for larger $B_\perp$ the g-factor does not describe the energy difference between the two lowest states, but between the second excited state and the ground state. The value of $B_\perp$ where $\delta g_{D3-D3} = \delta g_{D-D}$ is given by $B_\perp \approx (\hbar/el_0^2)(\gamma_c m_e/\sqrt{2}\hbar l_D)$. For GaAs parameters it is ≈ 25 T.

2.5 Double dots

A double dot structure comprises two single dots close enough for their mutual interaction to play an important role. Here we consider symmetric dots modeled by V of Eq. (2.3). Such a potential has an advantage that in the limits of small $d \to 0$ and large $d \to \infty$, the solutions converge to the single dot solutions centered at $\mathbf{r} = 0$ and $\pm l_0 \mathbf{d}$, respectively. We denote the displaced Fock-Darwin states as $\Psi_{n,l,\sigma}^{\pm d}(\mathbf{r}) \equiv \Psi_{n,l,\sigma}(\mathbf{r} \pm \mathbf{d})$. In further we put $\mathbf{d} = d\hat{x}$. We comment on the more general case later and will see that the main results presented in this chapter are independent on the direction of $\mathbf{d}$.

The symmetries of the double dot Hamiltonian with the spin-orbit interactions are listed in Tab. 2.1. The time reversal symmetry is always present at $B_\perp = 0$, giving Kramer's double degeneracy. The rotational space symmetry from the single dot case is lost; instead there are two discrete symmetries – reflections I_x about y and I_y about x. In zero magnetic field and without spin-orbit terms, the Hamiltonian has both I_x and I_y symmetries. If only Bychkov-Rashba or

representation	under I_x, I_y transforms as	numbers for $g^{n,l}_{i,\sigma}$			
		l - even		l - odd	
		L	D	L	D
Γ_1	1	1	1	1	-1
Γ_2	x	1	-1	1	1
Γ_3	xy	-1	1	-1	-1
Γ_4	y	-1	-1	-1	1

Table 2.2: Notation and transformation properties of C_{2v} representations. L and D are the coefficients of the dependence of $g^{n,l}_{i,\sigma}$ on the single dot functions (see text).

Dresselhaus terms are present, we can still preserve symmetries I_x and I_y by properly defining the symmetry operators to act also on the spinors (forming the double group). The Bychkov-Rashba term, $H_0 + H_{BR}$, is invariant to operations defined by the spatial invariance. This is not the case of H_D, since here the operators $-\mathrm{i}\sigma_y I_x$ and $-\mathrm{i}\sigma_x I_y$ do not describe a spatial reflection of both the orbital and spinor parts. The symmetry operations for H_{BR} and H_D are connected by the unitary transformation $(\sigma_x + \sigma_y)/\sqrt{2}$, which connects the two Hamiltonians themselves. Finally, if both spin-orbit terms are present, or at $B_\perp > 0$, the only space symmetry left is $I = I_x I_y$.

In the following we consider separately the cases of zero and finite magnetic fields.

2.5.1 Energy spectrum in zero magnetic field, without spin-orbit terms

If no spin-orbit terms are present the group of our double dot Hamiltonian is $C_{2v} \otimes SU(2)$. The $SU(2)$ part accounts for the (double) spin degeneracy. The orbital parts of the eigenstates of the Hamiltonian therefore transform according to the irreducible representations of C_{2v}. The representations[106] Γ_i, $i = 1...4$, along with their transformation properties under the symmetries of C_{2v}, are listed in Tab. 2.2. The symmetry properties will be used in discussing the perturbed spectrum.

We denote the exact eigenfunctions of the double dot Hamiltonian as $\Gamma^{ab}_{i\sigma}$ where $a(b)$ is the single dot level to which this eigenfunction converges as $d \to 0\,(\infty)$; i labels the irreducible representation, σ denotes spin. We have chosen the confining potential to be such, that at $d \to 0(\infty)$ the solutions of the double dot H_0 converge to the (shifted) Fock-Darwin functions, if properly symmetrized according to the representations of C_{2v}. These symmetrized functions will be denoted as $g^{n,l}_{i,\sigma}$, where (up to the normalization)

$$g^{n,l}_{i,\sigma} = (\Psi^d_{n,l,\sigma} + D_i \Psi^{-d}_{n,l,\sigma}) + L_i(\Psi^d_{n,-l,\sigma} + D_i \Psi^{-d}_{n,-l,\sigma}). \qquad (2.20)$$

The numbers $D_i(L_i)$ for different irreducible representations are in Tab. 2.2.

Generally, up to a normalization, an exact solution can be written as a linear combination of any complete set of functions (we omit the spin index which is the same for all terms in the equation)

$$\Gamma_i^{ab} = \sum_{n,l} \widetilde{c}(n,l) g_i^{n,l} = g_i^{n_0,l_0} + \sum_{n,l} c(n,l) g_i^{n,l}. \qquad (2.21)$$

The last equation indicates the fact, that for a function Γ_i^{ab} in the limit $d \to 0(\infty)$, there will be a dominant g-function in the sum with the numbers n_0, l_0 given by the level $a(b)$ and the coefficients c for the other functions will converge to zero. We term the approximation $c(n,l) = 0$ as a linear combination of single dot orbitals (LCSDO).

Knowing the representations of the double dot Hamiltonian and the fact that Fock-Darwin functions form $SO(2)$ representations (reflecting the symmetry of single dot H_0) we can decompose all single dot levels into the double dot representations and thus formally construct the energy spectrum of a double dot using the symmetry considerations only. Following the standard technique for constructing such correlation diagrams (connecting states of the same representation and avoiding crossing of lines of the same representation) we arrive at the spectrum shown in Fig. 2.6. The ground state transforms by the symmetry operations according to Γ_1 (identity), while the first excited state according to Γ_2 (x). This is expected for the symmetric and antisymmetric states formed by single dot ground states. The symmetry structure of the higher excited states is important to understand spin-orbit interaction effects. Indeed, the spin-orbit terms couple two opposite spins according to certain selection rules. Since H_D, for example, transforms similarly to $x \oplus y$, it couples the ground state Γ_1 with Γ_2 and Γ_4. In general, odd numbered representations can couple to even numbered representations. The same holds for H_{BR} and H_{D3}. If we include either H_{BR} or H_D into the Hamiltonian, and consider spinors as the basis for a representation, the states would transform according to Γ_5, the only irreducible representation of the double group of C_{2v}.

The calculated numerical spectrum for our model structure is shown in Fig. 2.7. There is a nice qualitative correspondence with Fig. 2.6. In Fig. 2.7 by vertical bars we denote coupling through H_D or H_{BR} ($|\langle i|H_D|j\rangle| = |\langle i|H_{BR}|j\rangle|$, if $l_D = l_{BR}$). The couplings follow the selection rule described above. Since there are several level crossings in the lowest part of the spectrum, a question arises if spin hot spots are formed in the presence of spin-orbit interaction. It turns out, that there is no first-order level repulsion at the crossings due to the linear spin-orbit terms because the levels are not coupled by the linear terms, even though such couplings are allowed by symmetry. *There are no spin hot spots due to the linear spin-orbit terms at zero magnetic field.* For example Γ_4^{11} and Γ_1^{21} are not coupled by spin-orbit terms, and therefore their degeneracy (at $2d \approx 50$

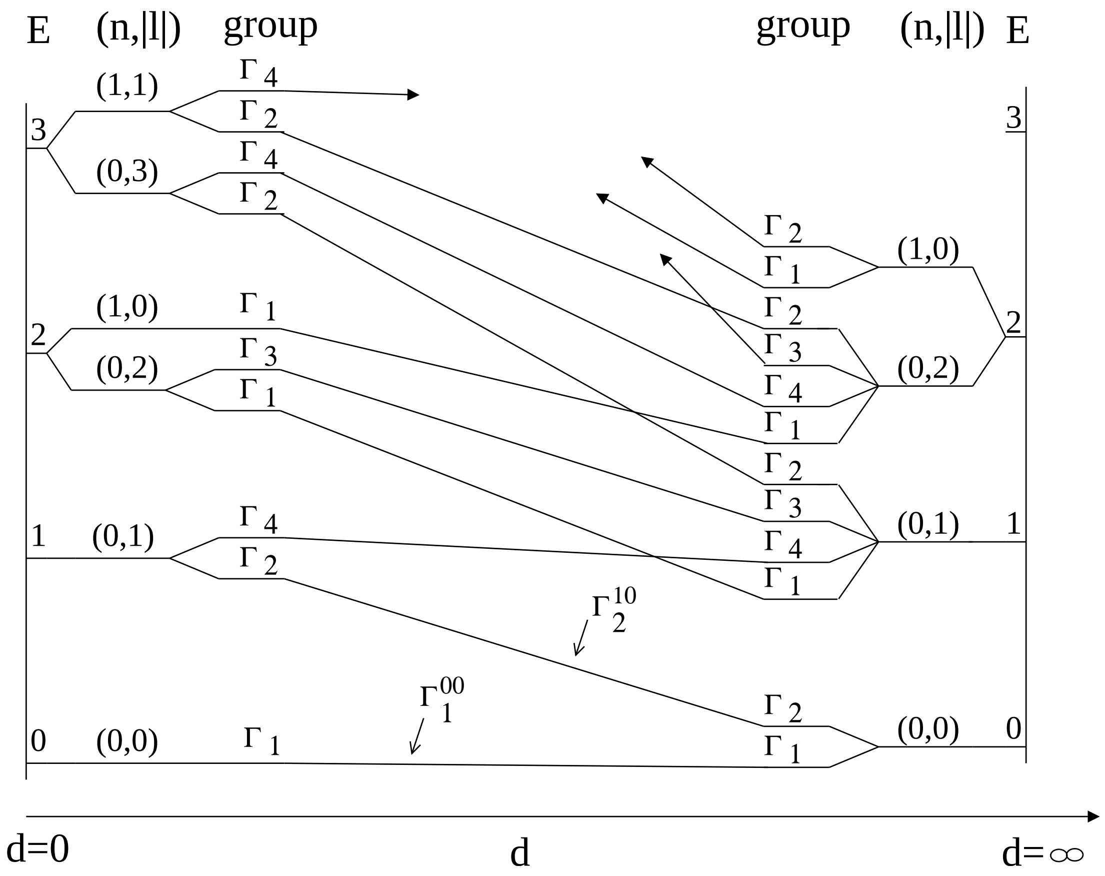

Figure 2.6: Single electron spectrum of a symmetric (C_{2v}) lateral double dot structure as a function of the interdot separation, at $B_\perp = 0$, derived by applying group theoretical considerations. Single dot states at $d = 0$ and $d = \infty$ are labeled by the principal (n) and orbital (l) quantum numbers, while the double dot states are labeled according to the four irreducible representations Γ_i of C_{2v}. The lowest double dot states have explicitly written indices showing the excitation level of the $d = 0$ and $d = \infty$ states they connect. Every state is doubly (spin) degenerate, and spin index is not given.

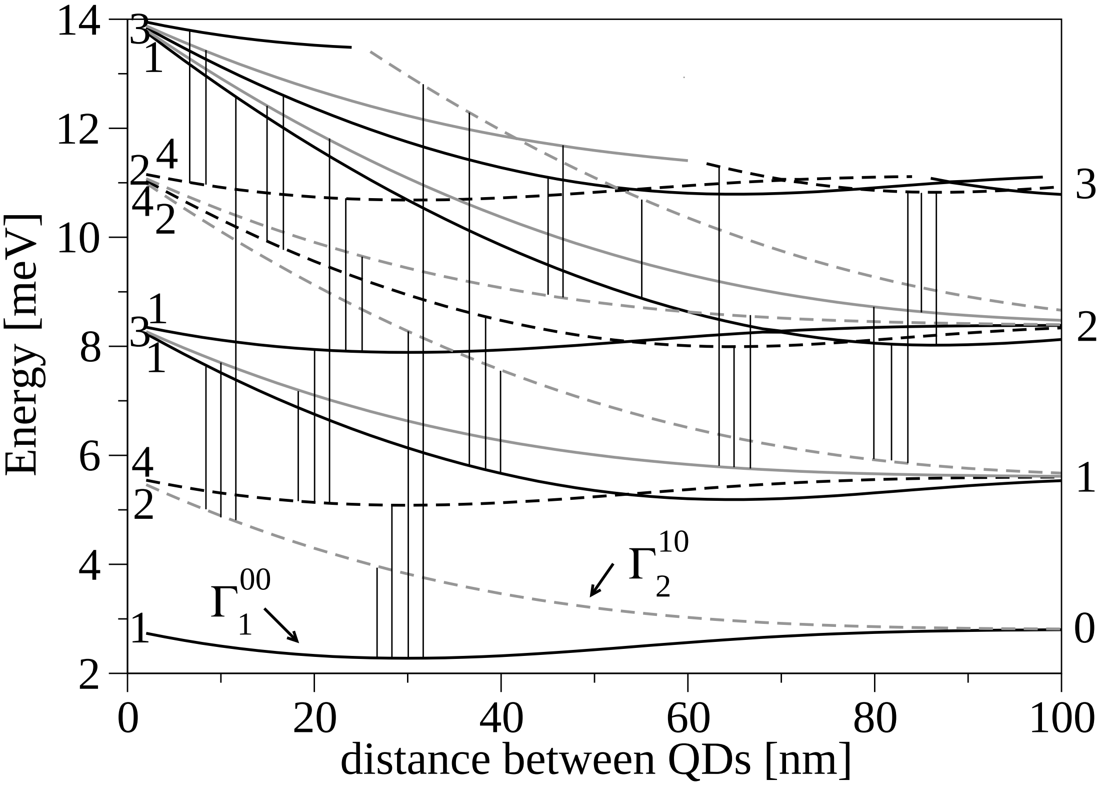

Figure 2.7: Calculated energy spectrum of a double quantum dot at $B_\perp = 0$, as a function of interdot distance. Spin-dependent terms are not included in the Hamiltonian. Vertical bars indicate couplings due to spin-orbit interactions. Group theoretical symbols are shown with the lines on the left. Single dot levels are denoted by the highest orbital momentum (0, 1, 2, ...) present in the degenerate set. This labeling is on the right. Every state is doubly degenerate, and spin index is not given.

nm) is not lifted by linear spin-orbit terms as we would expect from symmetry (actually, there is an anti-crossing which is of the order $l_{\rm lin}^{-3}$, instead of the expected $l_{\rm lin}^{-1}$). The cubic Dresselhaus term gives here (and also in other crossings that conform to the selection rules) a linear anti-crossing, as one expects. The absence of anti-crossings from the linear spin-orbit terms will be explained in the next section.

Since our main goal here is to study the effects of spin-orbit interaction on the tunneling between the two dots, we first look at the tunneling for $H_{SO} = 0$. We use the LCSDO approximation for the wavefunction Γ_i and compute energy as $E_i = \langle \Gamma_i | H \Gamma_i \rangle / \langle \Gamma_i | \Gamma_i \rangle$. We denote the energies of the two lowest orbital double dot states $\Gamma_{1\sigma}^{00} \equiv \Gamma_S^\sigma$, $\Gamma_{2\sigma}^{10} \equiv \Gamma_A^\sigma$ as $E_S^{(0)}, E_A^{(0)}$, where index zero indicates the absence of spin-orbit interaction. We obtain:

$$\begin{aligned} E_S^{(0)} &= E_0 \frac{1 + [1 - 2d/\sqrt{\pi}]e^{-d^2} + d^2 \mathrm{Erfc}(d)}{1 + e^{-d^2}}, \\ E_A^{(0)} &= E_0 \frac{1 - e^{-d^2} + d^2 \mathrm{Erfc}(d)}{1 - e^{-d^2}}. \end{aligned} \tag{2.22}$$

In the limit of large interdot separation the tunneling energy, $T = (E_A - E_S)/2$, becomes,

$$T^{(0)} \approx E_0 \frac{1}{\sqrt{\pi}} d e^{-d^2}. \tag{2.23}$$

It turns out that going beyond LCSDO does not improve the calculated $T^{(0)}$ significantly. The tunneling computed by full formulas, Eq. (2.22), does not differ from the numerically obtained value by more than 2% for any value of the interdot distance; the leading order becomes an excellent approximation for interdot distances larger than 50 nm.

2.5.2 Corrections to energy from spin-orbit interaction in zero magnetic field

When we add H_{SO} to H_0, the structure of the corrections to the energies of the two lowest states up to the second order in spin-orbit interactions can be expressed as

$$E_i^{(2)} = \frac{\hbar^2}{2m} \left[-\mathcal{A}_i (l_D^{-2} + l_{BR}^{-2}) - \mathcal{B}_i l_{D3}^{-2} + \mathcal{C}_i l_D^{-1} l_{D3}^{-1} \right], \tag{2.24}$$

where i is either S or A. For the two lowest states the coefficients $\mathcal{A}, \mathcal{B}$, and $\mathcal{C}$ are positive for all values of the interdot distance and the differences $\mathcal{A}_A - \mathcal{A}_S, \ldots$ approach zero as $d \to \infty$. We will argue below that $\mathcal{A}_S = \mathcal{A}_A = 1/2$ with the exception of a very small interdot distance (less than 1 nm). *There are thus no contributions from the linear spin-orbit interactions to the tunneling energy in the second order.* Only the cubic Dresselhaus term contributes, either by itself or in combination with the linear Dresselhaus term. Spin-dependent tunneling is greatly inhibited.

Numerical calculation of the corrections to the tunneling energy from spin-orbit interactions are shown in Fig 2.8. The dominant correction is the mixed D-$D3$ term, followed by $D3$-$D3$. These are the only second order corrections. For GaAs, and our model geometry, these corrections are about 4 and 5 orders of magnitude lower than $T^{(0)}$. The corrections, when only linear spin-orbit terms are present, are much smaller since they are of the fourth order. The dramatic enhancement of the corrections from linear spin-orbit terms close to $d = 0$ is due to the transition from coupled to single dots. We will explore this region in more detail later.

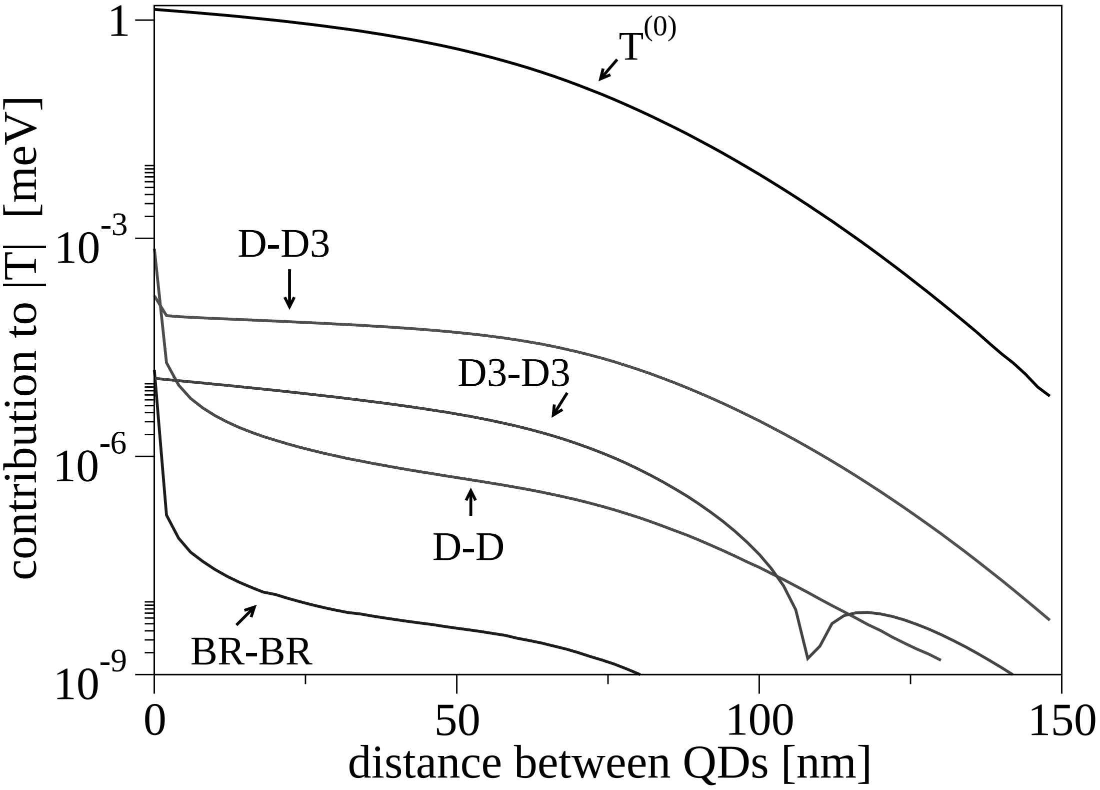

Figure 2.8: Calculated corrections to the tunneling energy T from spin-orbit terms at $B_\perp = 0$. The labels indicate which spin-orbit terms are involved. Only D-$D3$ and $D3$-$D3$ are of the second order. The remaining contributions are of the fourth order.

We first show that a naive approach to calculate spin-orbit contributions to the tunneling fails to explain the above results. We use the example of the linear Dresselhaus term. The simplest way to include this term is to begin with the two lowest orbital states (that are four states including spin), $g^{00}_{1\sigma}$ and $g^{00}_{2\sigma}$ and diagonalize the Hamiltonian in this basis. Because of the time reversal symmetry the resulting 4×4 matrix block diagonalizes into two equal 2×2 matrices with elements $H_{11} = E^{(0)}_S$, $H_{22} = E^{(0)}_A$, and $H_{12} = \langle g^{00}_{1\uparrow}|H_D|g^{00}_{2\downarrow}\rangle = -\mathrm{i}E_0(l_0/l_D)de^{-d^2}$. Using the large d limit for $T^{(0)}$, Eq. (2.23), we obtain the perturbed energies $E_{S(A)} = E_0 \pm E_0\sqrt{1/\pi + l_0^2/4l_D^2}de^{-d^2}$ with the minus (plus) sign for S (A). In the second order of $1/l_D$ the symmetric and antisymmetric level energies have opposite contributions, giving $T \approx [(E_0/\sqrt{\pi}) + (E_0\sqrt{\pi}/8)(l_0^2/l_D^2)]d\exp(-d^2)$, in contrast to the numerical results where there is no dependence on $1/l_D$ in the second order. A larger basis, as well as a small basis comprising single dot states including spin-orbit interaction, still yield the l_D^{-2} dependence.

From the previous example one can see that to get a correct (constant) spin-orbit contribution to the energy of a state, it is not enough to include finite number of terms in the sum in Eq. (2.10). Instead we employ the operators H^{op} given in Eqs. (2.12,2.13). To get a contribution for a particular state, say $|i\rangle$, we apply the Löwdin perturbation theory.[112] For this one has to identify states $|j\rangle$ which are degenerate with $|i\rangle$ with respect to the perturbation H_{SO} and these have to be treated exactly. The rest of the states can be treated perturbatively. The condition for a degeneracy of two states can be taken as $|E^{(0)}_i - E^{(0)}_j| \lesssim E_0 l_0/l_{\mathrm{lin}}(l_{D3})$, when one considers linear (cubic) terms. The finite set of the degenerate states will be denoted by $\mathcal{N}$. The effective Hamiltonian H^{eff} acting in $\mathcal{N}$ is

$$H^{\mathrm{eff}}_{ij} = (H_0 + H_{SO})_{ij} + \frac{1}{2}\sum_{k\notin\mathcal{N}}[\frac{(H_{SO})_{ik}(H_{SO})_{kj}}{E^{(0)}_i - E^{(0)}_k} + \frac{(H_{SO})_{ik}(H_{SO})_{kj}}{E^{(0)}_j - E^{(0)}_k}]. \tag{2.25}$$

For the example of the linear Dresselhaus term, we can now use Eq. (2.11) and (2.14) to obtain

$$H^{\mathrm{eff}}_{ij} = (H_0 + H_D)_{ij} - \frac{\hbar^2}{4ml_D^2}(1 - \sigma_z l_z/\hbar)_{ij} + R_{ij}, \tag{2.26}$$

where

$$R_{ij} = \frac{1}{2}\langle i|H_D P_{\mathcal{N}} H^{op}_D - H^{op}_D P_{\mathcal{N}} H_D|j\rangle. \tag{2.27}$$

First we note that existence of the operator H^{op}_D means that the coupling through H_D between any two states is always much smaller then the difference of the unperturbed energies of these two states, since $(H_D)_{ij} = (E^{(0)}_i - E^{(0)}_j)(H^{op}_D)_{ij} \sim (E^{(0)}_i - E^{(0)}_j)(l_0/l_D)$. Then one can partially diagonalize the effective Hamiltonian to eliminate the off-diagonal H_D terms. It turns out, that this leads to a cancellation of the terms H_D and R. The effective Hamiltonian is then

$$H_{ij}^{\mathrm{eff}} = (H_0)_{ij} - \frac{\hbar^2}{4ml_D^2}\left(1 - \sigma_z l_z/\hbar\right)_{ij}. \tag{2.28}$$

This completes the way to get Eq. (2.17) using Löwdin perturbation theory. There are no linear effects on the double dot energy spectrum from linear spin-orbit terms, which explains the absence of spin hot spots even though symmetry allows that.

The spin-orbit interaction influences the energy only through the operator l_z, which is of the symmetry Γ_3, from where we get selection rule – the allowed coupling is between functions of representations Γ_1 – Γ_3 and Γ_2 – Γ_4. Looking at Fig. 2.7, accidental degeneracies of states with such representations are not present in the lower part of the spectrum. The crossing of Γ_1^{21} with Γ_4^{11} considered in the discussion to Fig. 2.7 also does not follow the selection rule, hence why the anti-crossing is of the third order. From the selection rules one can immediately see that also the expectation value of l_z is zero in any state. This result is more general and holds also if the symmetry of the potential is lower (or none), since it follows from the fact that the Hamiltonian H_0 is real, so one can choose eigenfunctions to be real. Then the expectation value of any imaginary operator, such as l_z, must vanish. We conclude, that apart from degeneracies following from the single dot [that is limits $d \to 0(\infty)$] and possible accidental degeneracies respecting the selection rule, double dot states are non-degenerate and described by a 1×1 effective Hamiltonian

$$H_{ii}^{\mathrm{eff}} = E_i^{(0)} - \frac{\hbar^2}{4ml_D^2}. \tag{2.29}$$

Particularly, the energies of the two lowest states are given by this equation, with an exception for the state Γ_A in the region of small d where it is coupled to Γ_4^{11} through l_z and we have to describe it here by a 2×2 effective Hamiltonian.

An illustration of the l_z influence on the spectrum is in Fig. 2.9, where the linear Dresselhaus spin-orbit contribution to the energy for several states as a function of the interdot distance is shown. One can see at what interdot distances the l_z operator causes the qualitative change between the double dot case (where the functions are characterized by a definite representation Γ_i and the energy contribution from the spin-orbit is a uniform shift) and the single dot case (where the functions are numbered according to the orbital momentum and the spin-orbit contribution to the energy depends on $\sigma_z l_z$). This happens when $\hbar^2/ml_D^2$ is comparable to the energy difference of the nearly degenerate states. If the criterion for the coupling between the dots is the constant contribution, $-\hbar^2/4ml_D^2$, to the energy, then the double dot region, as far as the spin-orbit interaction is concerned, is between 1 to 100 nm, that is up to 5 times of the

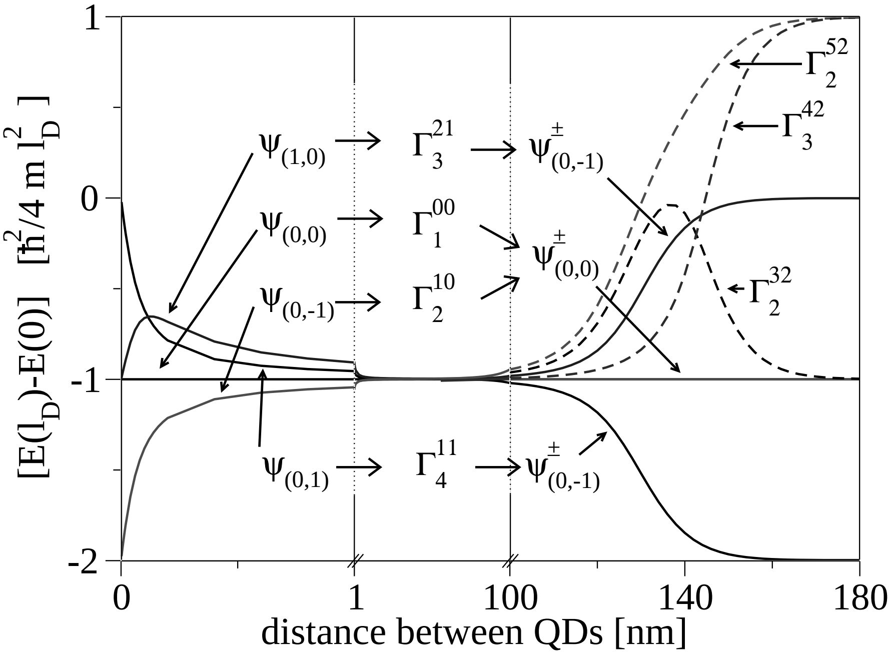

Figure 2.9: Calculated corrections to selected lowest energy levels due to H_D. All states have spin $\sigma = +1$. The graph demonstrates a transition between the symmetry group of the double dot H_0 (states Γ) and that of single dots (states Ψ). The transition is induced by l_z which by symmetry couples states $\Gamma_1 \leftrightarrow \Gamma_3$ and $\Gamma_2 \leftrightarrow \Gamma_4$. Thus the anti-crossing mechanism will induce transition $\Gamma_{1(3)} \leftrightarrow \Gamma_1 \pm \Gamma_3$ and $\Gamma_{2(4)} \leftrightarrow \Gamma_2 \pm \Gamma_4$. These linear combinations are equal to a single dot solution $\Psi_{n,l,\sigma}$ in the case $d \rightarrow 0$ and a combination $\Psi^{\pm}_{n,l,\sigma} \equiv \Psi^{d}_{n,l,\sigma} \pm \Psi^{-d}_{n,l,\sigma}$ of functions with the same orbital momenta in the case $d \rightarrow \infty$.

confinement length of 20 nm. As an example, for the function Γ_4^{11} the coupling in the effective Hamiltonian through l_z to Γ_2^{31} is equal to the unperturbed energy difference if $l_D^2 \sim l_0^2 d^3 e^{-d^2}$, giving $d \approx 3$, corresponding to the interdot distance of $6l_0$. Due to the exponential, this result is only slightly sensitive to l_D.

The Bychkov-Rashba term can be treated analogously. The effective Hamiltonian is $H^{\mathrm{eff}}_{ij} = [H_0 - (\hbar^2/4ml_{BR}^2)(1 + \sigma_z l_z/\hbar)]_{ij}$. The absence of a linear influence on the energy was based on the existence of H_D^{op}. Since we found a case where H_{D3} causes linear anti-crossing (see discussion to Fig. 2.7), it follows that H_{D3}^{op} can not exist for our double dot potential. However, if one approximates $E_i - E_k \approx E_j - E_k$ in (2.25), one can use H_D^{op} to simplify the mixed D-$D3$ correction. This, according to Fig. 2.8, is the dominant spin-orbit correction for the tunneling energy T. One gets an analogous expression as Eq. (2.26), where the needed commutator is stated in Eq. (2.16). Concluding, if we neglect the mixed $D3$-$D3$ term, we can write the spin-orbit contribution to the energy for the lowest orbital states to be

$(i = S, A)$

$$\delta E_i^{SO} = -\frac{\hbar^2}{4m}(l_D^{-2} + l_{BR}^{-2}) + \frac{\gamma_c}{2\hbar^2 l_D}(\mathbf{p}^2)_{ii}. \tag{2.30}$$

One note to the eigenfunctions: The matrix elements of the effective Hamiltonian are computed using the eigenfunctions of H_0. But the functions that correspond to the solutions are transformed by the same unitary transformation that leads from H_0 to H^{eff}. The sum rule can be used also here to express the influence of H_{lin} on the eigenfunctions of H_0. If $H_0\Gamma_{i\sigma} = E_i\Gamma_{i\sigma}$, the eigenfunctions corresponding to the effective Hamiltonian, Eq. (2.26), are

$$\overline{\Gamma}_{i\sigma} = [\mathbb{I} + \sum_{j\notin\mathcal{N}} \frac{(H_{\text{lin}})_{ji}}{E_i - E_j}]\Gamma_{j\sigma} = [\mathbb{I} - (\mathbb{I} - P_{\mathcal{N}})H_{\text{lin}}^{op}]\,\Gamma_{i\sigma}. \tag{2.31}$$

Partial diagonalization of the effective Hamiltonian, to go from Eq. (2.26) to Eq. (2.28), means we finish the unitary transformation completely and get $\overline{\Gamma}_{i\sigma} = \Gamma_{i\sigma} - H_{\text{lin}}^{op}\Gamma_{i\sigma}$ for the eigenfunctions corresponding to the effective Hamiltonian, Eq. (2.28).

2.5.3 Finite magnetic field, no spin-orbit terms

The presence of a perpendicular magnetic field lowers the symmetry of the Hamiltonian without spin-orbit terms. The only nontrivial symmetry operator is the inversion I (see Tab. 2.2). As a consequence the double dot states fall into two groups (representations of C_2): Γ_1 and Γ_3 become Γ_S (symmetric under I) and Γ_2 and Γ_4 become Γ_A (antisymmetric under I). Symmetrized functions $g_{i\sigma}^{n,l}$ now are

$$g_{i\sigma}^{n,l} = \Psi_{n,l,\sigma}^{-d} + D_i\Psi_{n,l,\sigma}^{d}, \tag{2.32}$$

where the irreducible states $i = S$ and A, while the permutation coefficients $D_S = -D_A = 1$. The shifted single-dot wave functions acquire a phase:

$$\Psi_{n,l,\sigma}^{\pm d}(\mathbf{r}) = \Psi_{n,l,\sigma}(\mathbf{r} \pm \mathbf{d})e^{\pm(iel_0/2\hbar)\mathbf{B}.(\mathbf{d}\times\mathbf{r})}, \tag{2.33}$$

depending on which dot they are located.

The double dot energy spectrum of H_0 as a function of magnetic field is shown in Fig. 2.10 for the interdot distance of 50 nm. Indicated are two crossings and one anti-crossing induced by magnetic field. States Γ_1 and Γ_2 (notation from the $B_\perp = 0$ case) are not coupled because they have opposite spins. The second crossing is between Γ_2 and Γ_3, which behave differently under I. An example of anti-crossing induced by magnetic field is between Γ_2 and Γ_4, which are both antisymmetric under I.

In analogy with Eq. (2.22) we derive analytical expressions for the energies of the lowest symmetric and antisymmetric state in the presence of magnetic field using the LCSDO approximation:

$$\begin{aligned} E_S^{(0)} &= \frac{E_0}{\eta^2}\Big(\frac{1+[1-d\eta(1-\theta^2)/\sqrt{\pi}]e^{-(d\eta)^2(1+\theta^2)}}{1+e^{-(d\eta)^2(1+\theta^2)}} - \\ &\quad -\frac{d\eta(1-\theta^2)[e^{-(d\eta)^2}/\sqrt{\pi}-d\eta\,\mathrm{Erfc}(d\eta)]}{1+e^{-(d\eta)^2(1+\theta^2)}}\Big), \\ E_A^{(0)} &= \frac{E_0}{\eta^2}\Big(\frac{1-[1-d\eta(1-\theta^2)/\sqrt{\pi}]e^{-(d\eta)^2(1+\theta^2)}}{1-e^{-(d\eta)^2(1+\theta^2)}} - \\ &\quad -\frac{d\eta(1-\theta^2)[e^{-(d\eta)^2}/\sqrt{\pi}-d\eta\,\mathrm{Erfc}(d\eta)]}{1-e^{-(d\eta)^2(1+\theta^2)}}\Big). \end{aligned} \tag{2.34}$$

Here $\eta = l_0/l_B = (1-\theta^2)^{-1/4}$. In the limit $d \to \infty$, we can then deduce the tunneling energy in the leading order to be

$$T^{(0)} = E_0\frac{1}{\sqrt{\pi}}(1-\theta^2)^{5/4}e^{-d^2(1+\theta^2)/\sqrt{1-\theta^2}}. \tag{2.35}$$

If $\theta = 0$, the above expressions reduce to Eq. (2.22,2.23). On the other hand, if $B_\perp \to \infty$, then $T^{(0)} \sim B_\perp^{-5/2}e^{-B_\perp/B_0}$.

At a finite magnetic field we have also a new term in the Hamiltonian, the Zeeman term. Since it commutes with H_0 the only consequence of this term is a shift of the energy of the states by a value $\sigma\mu B_\perp$ according to their spin σ. Therefore it is this term that breaks the Kramer's degeneracy and introduces crossings of the states with opposite spin. An example of this can be seen in Fig. 2.11, where we plot energies of the four lowest states in the region where the Zeeman shift is comparable to the energy differences of the considered states.

2.5.4 Effective spin-orbit Hamiltonian

We now study the influence of the spin-orbit interactions on the spectrum of double dots in a finite magnetic field. We will see that the spin-orbit terms lead to new spin hot spots even at magnetic fields of the order of 1 T, and that the linear spin-orbit terms will influence tunneling in the second order.

Although the presence of the Zeeman term complicates the analysis of the perturbation theory using operators H^{op}, one can still apply the previously developed formalism if the Zeeman term is treated as a part of perturbation. (For a harmonic potential describing single dots, operators H^{op}_{lin} have been derived[154] for the case of finite magnetic field, so that the Zeeman term can be included into H_0). Up to the second order in the perturbation couplings (being now l_{SO} and α_Z), there is no coupled Zeeman-spin-orbit term. This means that in the effective Hamiltonians H^{eff} that we already derived for the case of zero magnetic field, the

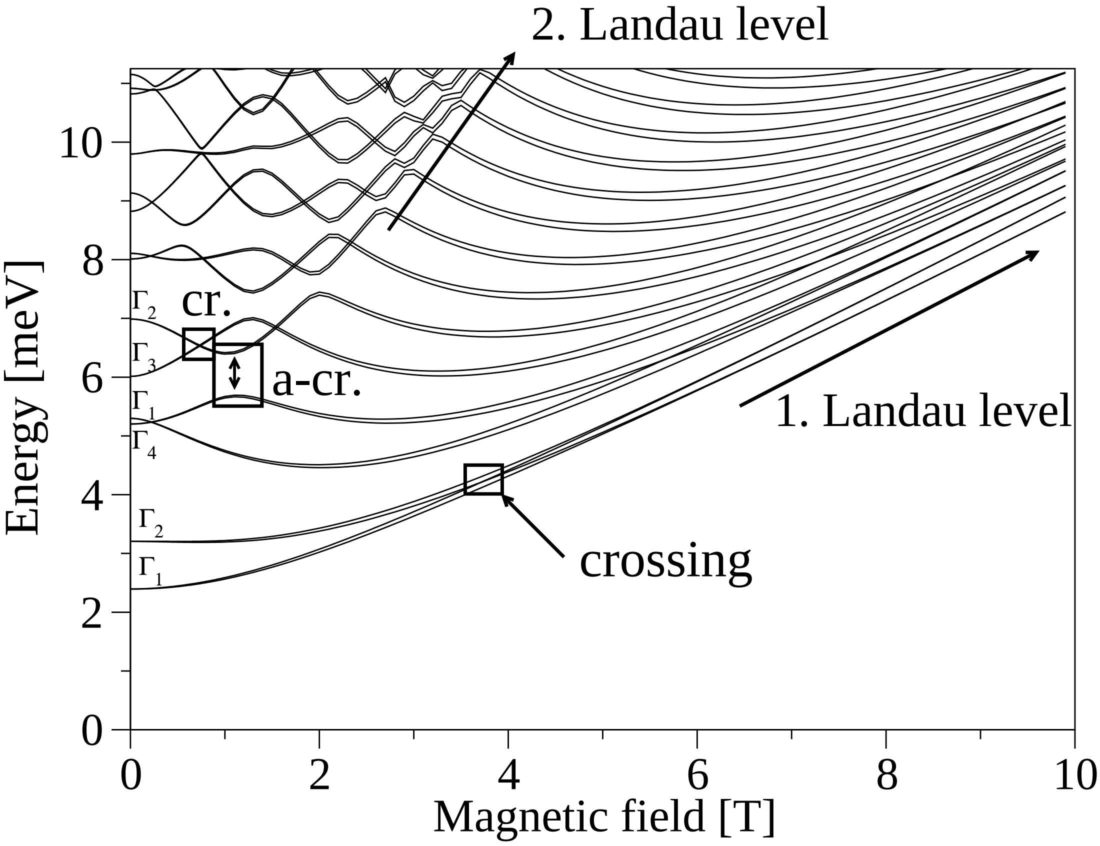

Figure 2.10: Computed energy spectrum of the double dot Hamiltonian without H_{SO}, as a function of magnetic field. The quantum dot separation is 50 nm (single dot confinement length is 20 nm). The energy levels are labeled according to the symmetry of the states at $B_\perp = 0$. Two crossings (one between Γ_2 and Γ_3, the other between Γ_1 and Γ_2) and one anti-crossing (between Γ_2 and Γ_4) are indicated. In the limit $B_\perp \to \infty$ the states merge to Landau levels.

Zeeman term appears as a shift of the energies on the diagonal without bringing any new couplings (non-diagonal terms). But an important consequence is that the shift can change the number of states we have to include into the basis where the effective Hamiltonian acts, because their energy difference to the considered state is comparable to the spin-orbit interaction.

First, in analogy with Eq. (2.29), if the energy of a state is far enough from others, we can consider the basis to consist of one term only and the spin-orbit correction to the energy of state $|i\rangle$ is

$$\delta E_i^{SO} = -\frac{\hbar^2}{4ml_D^2}(1-\sigma\overline{L_z}/\hbar) - \frac{\hbar^2}{4ml_{BR}^2}(1+\sigma\overline{L_z}/\hbar) + \overline{[H_D^{op}, H_{D3}]}, \tag{2.36}$$

where the averaging means the expectation value in the state $|i\rangle$ and σ is the spin of the state. Since the presence of magnetic field lowers the symmetry, the last commutator, [Eq. (2.16)], can not be simplified according to the symmetry as was the case before in Eq. (2.30), and, more important, we no longer have $\overline{L_z} = 0$. As a result, there are now corrections to the tunneling that are of the second order in the linear spin-orbit interactions. These corrections depend on $\alpha_-^{(2)} \equiv l_0^2(l_D^{-2} - l_{BR}^{-2})$.

Second, we look how the energies of the four lowest states are changed, using again the example of the linear Dresselhaus term. They are plotted in Fig. 2.11. Here in the main figure one can see the shift caused by the Zeeman term. The anti-crossing induced by the spin-orbit interaction is magnified in the inset, the anti-crossing states being $\Gamma_S^\downarrow$ and $\Gamma_A^\uparrow$. In the case of zero magnetic field we described each of the four basis states by Eq. (2.29). Now, in principle, we have to describe them by a 4×4 effective Hamiltonian Eq. (2.26). Due to symmetry we can simplify this Hamiltonian into two 2×2 Hamiltonians, $H_1^{\rm eff}$, $H_2^{\rm eff}$, acting in the bases $\Gamma_S^\uparrow, \Gamma_A^\downarrow$ and $\Gamma_S^\downarrow, \Gamma_A^\uparrow$ respectively. The four components of the effective Hamiltonian matrix are

$$\begin{aligned}
(H^{\rm eff})_{11} &= E_S^{(0)} - \frac{\hbar^2}{4ml_D^2}[1-\sigma(L_z)_{11}/\hbar] - \sigma\mu_B B_\perp - R_{11},\\
(H^{\rm eff})_{22} &= E_A^{(0)} - \frac{\hbar^2}{4ml_D^2}[1+\sigma(L_z)_{22}/\hbar] + \sigma\mu_B B_\perp + R_{11},\\
(H^{\rm eff})_{12} &= (H^{\rm eff})_{21}^\dagger = (H_D)_{12},
\end{aligned} \tag{2.37}$$

where $\sigma = 1$ for $H_1^{\rm eff}$ and $\sigma = -1$ for $H_2^{\rm eff}$, while indices 1,2 denote the first and the second term in the corresponding basis. Comparing to the case of zero magnetic field the Zeeman term increases the difference of the diagonal elements in $H_1^{\rm eff}$ and decreases them in $H_2^{\rm eff}$. The ground and the fourth excited states which are described by $H_1^{\rm eff}$ stay isolated, and we can do the perturbative diagonalization to get rid of the off-diagonals. The energy of the two states is then up to the second order in the spin-orbit interaction accurately described by Eq. (2.36). Concerning the states $\Gamma_S^\downarrow$ and $\Gamma_A^\uparrow$, there is a region in the interdot distance of a

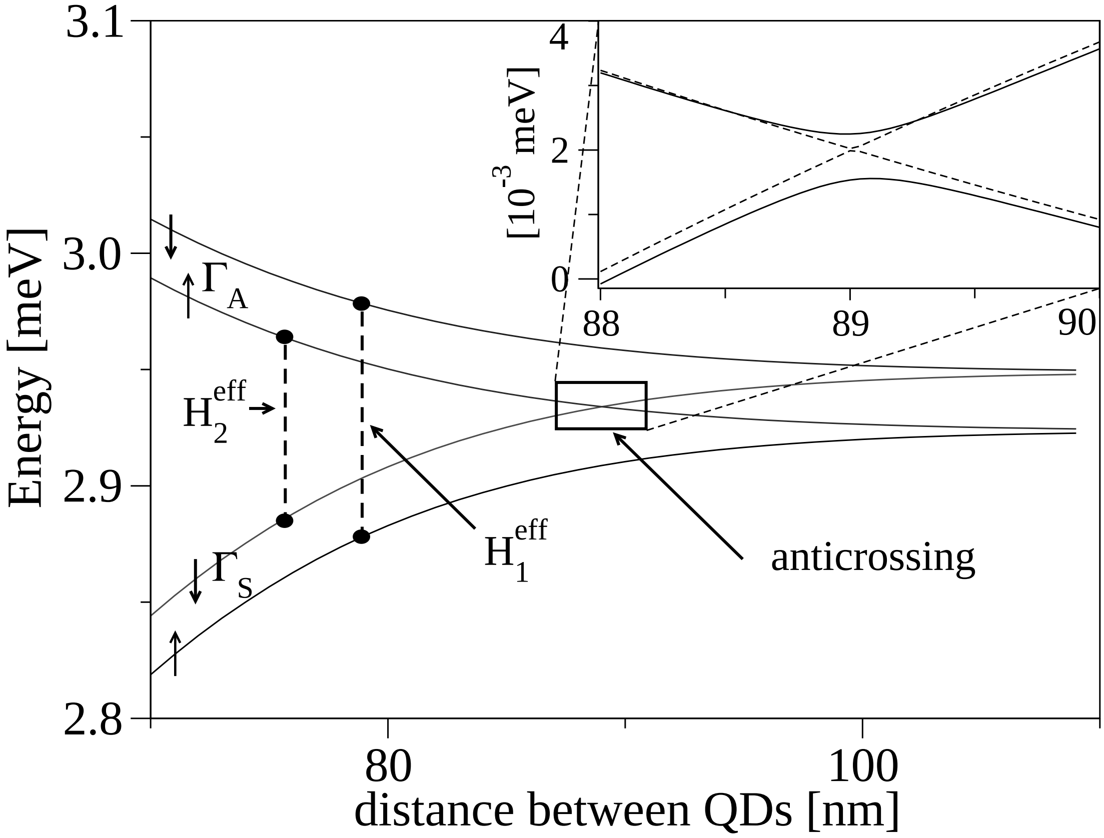

Figure 2.11: Calculated energies of the four lowest states of Hamiltonian $H_0 + H_Z$ at $B_\perp = 1$ T. The vertical dashed lines indicated doublets in the effective Hamiltonian. The inset displays the anti-crossing at 89 nm due to H_D. Here, the dashed lines are energies of $H_0 + H_Z$, solid lines of $H_0 + H_Z + H_D$.

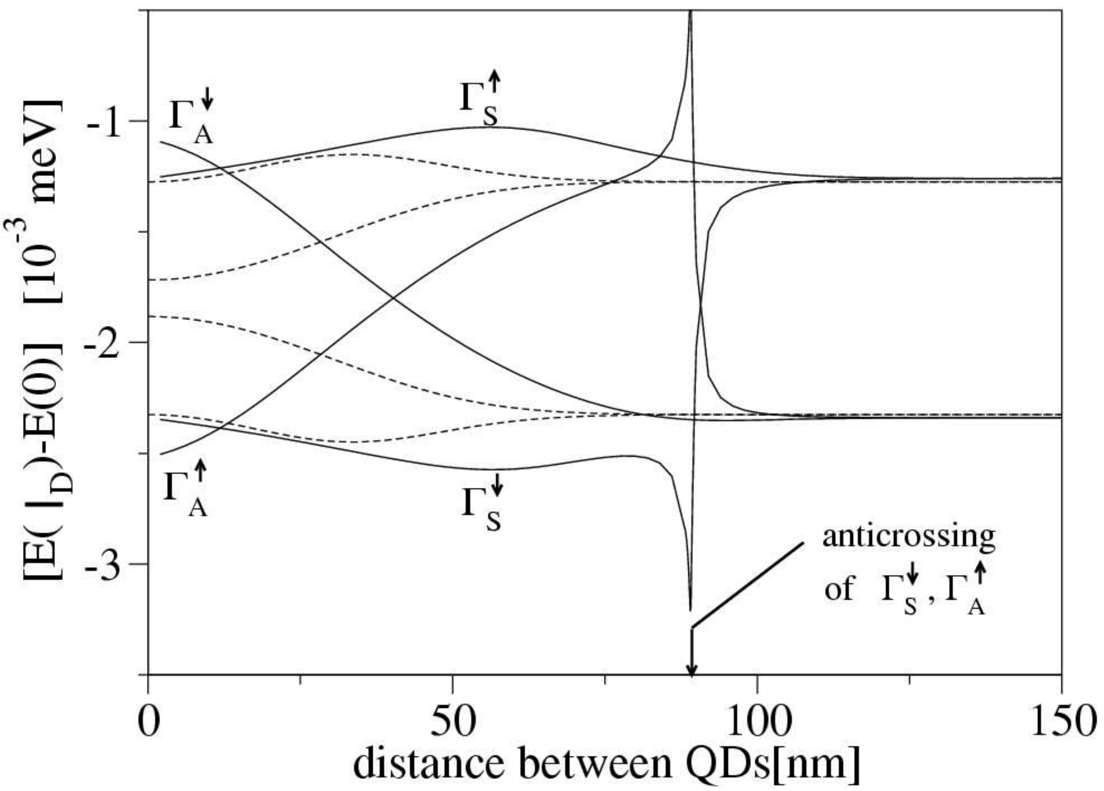

Figure 2.12: Calculated corrections to the energies of the four lowest states due to the linear Dresselhaus term H_D, at $B_\perp = 1$ T. Solid lines are numerical data, dashed lines are analytical expressions computed by Eq. (2.36) using the LCSDO approximation for the states.

few nanometers, where the two states must be described by the two dimensional H_2^{eff} to account for the anti-crossing, which is caused by the the matrix element $\langle \Gamma_S^\downarrow | H_D | \Gamma_A^\uparrow \rangle$. LCSDO gives for this element a result correct only in the order of magnitude. This is because even in the limit $d \to \infty$ this matrix element is of the same order as the neglected coefficients $c(n,l)$ in the LCSDO approximation, Eq. (2.21).

The spin-orbit corrections to the energies from H_D for the four lowest states as functions of the interdot distance are in Fig. 2.12. Also shown are analytical values computed by Eq. (2.36), that is, ignoring anti-crossing. The scale implies that the corrections are of the second order in $1/l_D$ and for the states $\Gamma_S^\downarrow$ and $\Gamma_A^\uparrow$ are enhanced in the anti-crossing region.

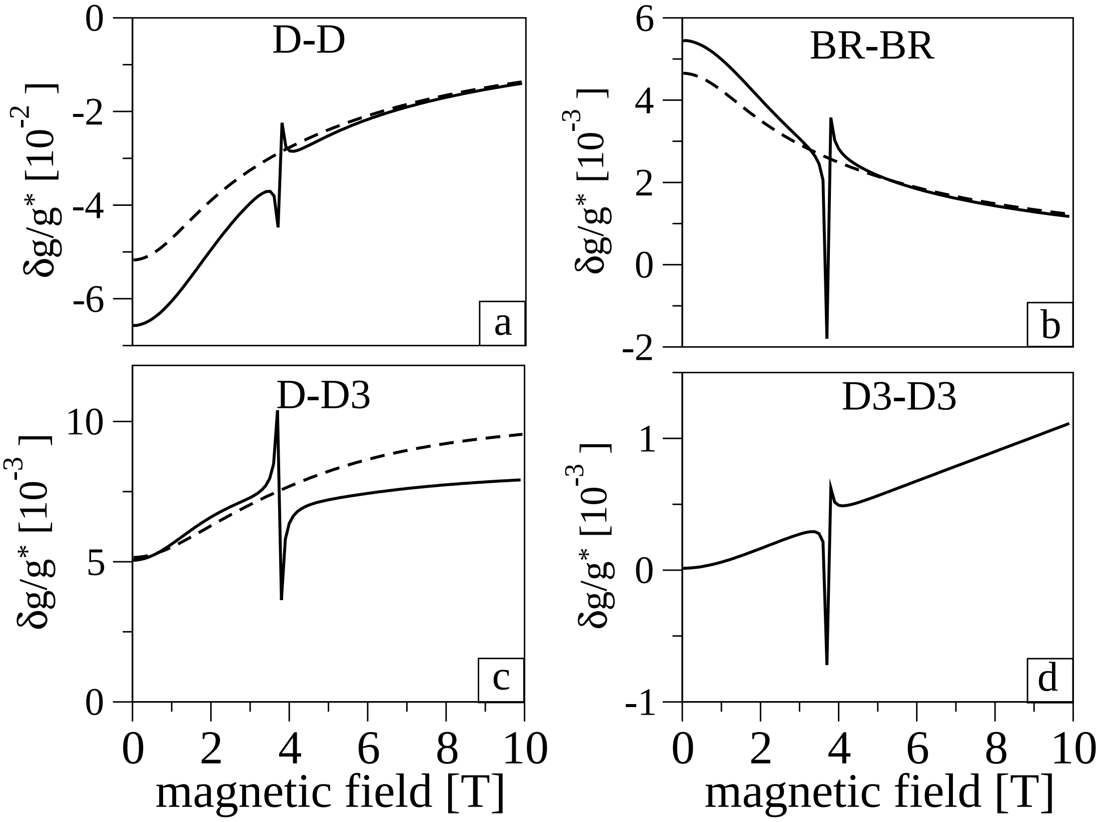

Figure 2.13: Calculated spin-orbit corrections to the effective g-factor (relative to the conduction band value g^*) as a function of magnetic field. The distance between the dots is 50 nm. Solid lines are numerical data, dashed lines are analytical values computed using Eq. (2.36). Contributions come from linear spin-orbit terms (a, b), the mixed Dresselhaus correction from H_D and H_{D3} (c) and the cubic Dresselhaus H_{D3} correction (d).

2.5.5 Spin-orbit corrections to the effective g-factor and tunneling frequency

We next analyze spin-orbit corrections to the g-factor, $\delta g \equiv [\delta E(\Gamma_S^{\downarrow}) - \delta E(\Gamma_S^{\uparrow})]/\mu_B B_\perp$, which characterizes the energy cost of a spin flip in the ground state, or the frequency of a spin precession. Another kind of oscillation is electron tunneling, when electron oscillates between the left and the right dot without changing its spin. The frequency of this oscillation, T/h, is given by the energy difference $T^{\uparrow} = [E(\Gamma_A^{\uparrow}) - E(\Gamma_S^{\uparrow})]/2$. Corrections to this energy difference induced by the spin-orbit interaction are denoted by δT^{σ}.

First, we take a look at the spin-orbit corrections to the g-factor. Contributions in the second order of the spin-orbit interactions are shown in Fig. 2.13, as functions of magnetic field at a constant interdot distance. The spin-orbit contribution to the g-factor in the double dot case has the same qualitative dependence on the magnetic field as in the single dot case (see discussion to Fig. 2.5). However, at finite interdot distances, there is an enhancing effect on the spin-orbit contributions. This can be seen in Fig. 2.12, where at a certain magnetic field, the spin-orbit contribution to the g-factor is enhanced for a finite d compared to the case of $d = 0(\infty)$. We found numerically, that the enhancement can be up to 50% of the value of the correction in $d = 0$ at magnetic fields of the order of 1 T.

At the anti-crossing the spin-orbit contributions show cusps. At magnetic fields bellow the anti-crossing, the dominant spin-orbit contribution is D-D which reduces the conduction band g-factor by several percent. Contributions D-$D3$ and BR-BR are one order of magnitude smaller. Using Eq. (2.36), that is ignoring the anti-crossing, we get for the contribution from the linear spin-orbit terms

$$\delta g_{\mathrm{lin-lin}} = -\frac{E_0}{2\mu_B B_\perp}\alpha_-^{(2)}\overline{L_z}/\hbar, \tag{2.38}$$

where, in the limit $d \to \infty$, ($\eta = l_0/l_B = (1-\theta^2)^{-1/4}$),

$$\overline{L_z} \approx \hbar\theta[1 + (d/\eta)^2 e^{-(d\eta)^2(1+\theta^2)}]. \tag{2.39}$$

From Fig. 2.13 one can see that the analytical result agrees with numerics.

Finally, we look at the tunneling energy in the presence of both magnetic field and spin-orbit couplings. The spin-orbit corrections, as a function of magnetic field, are shown in Fig. 2.14. At zero magnetic field there is no contribution from the linear terms (result of the section 2.5.2) and the dominant contribution is D-$D3$. Similarly to $T^{(0)}$, the corrections decay exponentially with increasing magnetic field. Anti-crossing strongly influences the tunneling energy. Using LCSDO for $d \to \infty$ we obtain in the leading order

$$\delta T^\sigma = -\sigma(E_0/4)\alpha_-^{(2)}\theta(d/\eta)^2 e^{-(d\eta)^2(1+\theta^2)}. \tag{2.40}$$

This analytical formula underestimates the corrections from the linear spin-orbit terms by a factor of ~ 3. Nevertheless the analytical expression for D–$D3$ is reasonably good. In the magnetic field below anti-crossing, the relative change of the tunneling energy stemming from the spin-orbit terms is of order 10^{-3}. In the inset b, there are contributions to the tunneling from the linear Dresselhaus term for both spin states. The importance of their difference will be explained in the next section.

2.5.6 Tunneling Hamiltonian

We now use our results to describe the influence of the spin-orbit interaction on the lowest part of the spectrum. We restrict our Hilbert space on the four lowest states $\Gamma^\sigma_{S(A)}$, the eigenstates of the total double dot Hamiltonian. Because of the

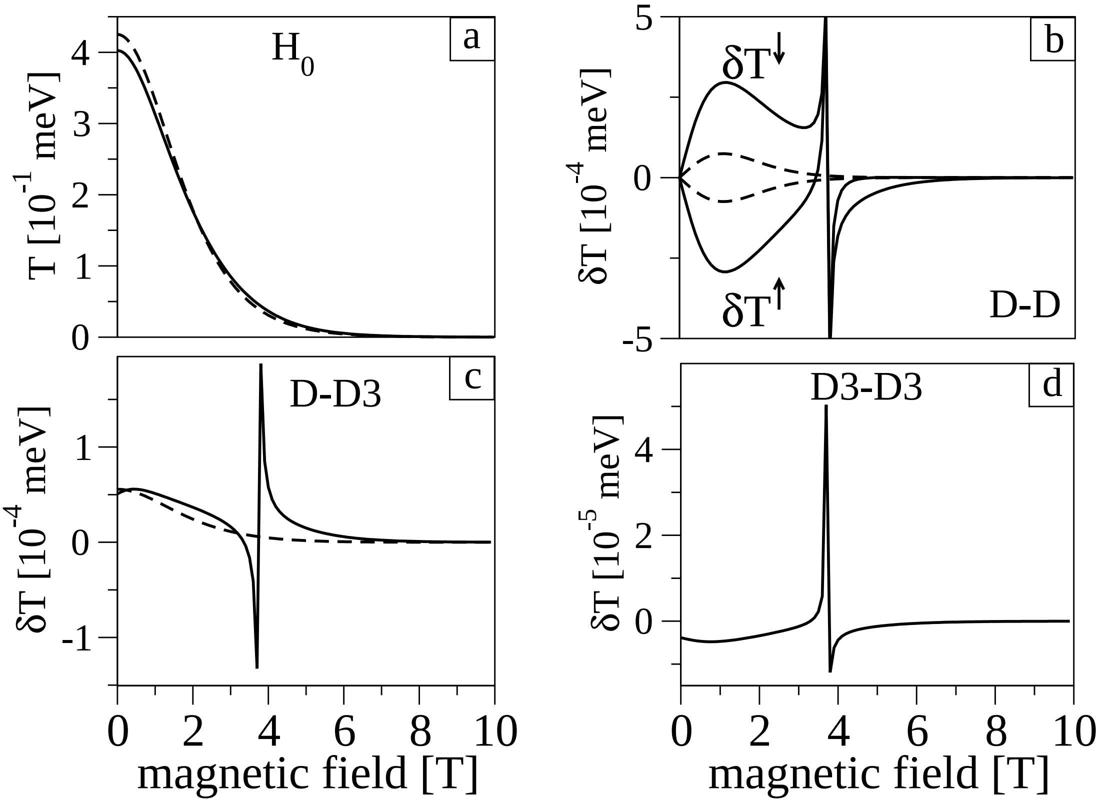

Figure 2.14: Calculated spin-orbit corrections to the tunneling energy T as a function of magnetic field. The interdot distance is 50 nm. Solid lines are numerical data, dashed lines are analytical expressions computed by Eq. (2.36). a) Tunneling without spin-orbit interactions present. b) Contribution to the tunneling from linear Dresselhaus for both spin up and down. c) The mixed linear – cubic and d) cubic – cubic Dresselhaus contributions.

transformation Eq. (2.31) these four states have neither definite symmetry with respect to inversion I, nor a definite spin in z direction. In this section we will denote them as spin 'up' and spin 'down' states. For description of a transport through the double dot it is useful to define the following left and right localized functions

$$L^\sigma(R^\sigma)=\frac{1}{\sqrt{2}}(\Gamma^\sigma_S\pm\Gamma^\sigma_A), \tag{2.41}$$

where plus and minus holds for L and R, respectively. In the limit $d\to\infty$ these functions converge to single dot solutions localized in the left and right dot.

The effective Hamiltonian of our system in the second quantization formalism is

$$H=\sum_{\sigma=\uparrow,\downarrow}E^\sigma(n_{L\sigma}+n_{R\sigma})-T^\sigma(a^\dagger_{L\sigma}a_{R\sigma}+a^\dagger_{R\sigma}a_{L\sigma}), \tag{2.42}$$

where $E^\sigma=(E^\sigma_S+E^\sigma_A)/2$, $T^\sigma=(E^\sigma_A-E^\sigma_S)/2$, while $a^\dagger$, and a are creation and annihilation operators, and $n=a^\dagger a$. We can get both localized and spin-pure states if we diagonalize σ_z in a chosen basis. For example, taking $L^\uparrow$ and $L^\downarrow$, we get $L^{\mathrm{pure}\uparrow}\sim(L^\uparrow+oL^\downarrow)$ and $L^{\mathrm{pure}\downarrow}\sim(L^\downarrow-o^+L^\uparrow)$, up to normalization $(1-|o|^2/2)$. That is, the left pure spin state is a linear superposition of both left states with spin 'up' and 'down'. The coefficient o is proportional to l^{-1}_{SO}.

In the following we are interested in the time evolution of localized states given by Hamiltonian Eq. (2.42). First we note, that due to the non-diagonal terms, the electron which is in a localized state will tunnel into the other localized state after the tunneling time $t^\sigma_{\mathrm{tun}}=h/2T^\sigma$, resulting in coherent oscillations. For our parameters $t_{\mathrm{tun}}\approx 1$ ps. In the Hamiltonian there is no mixing between spin 'up' and 'down' states. However, there will be mixing (or spin-flip) if we work with localized pure spin states. Electron being originally in $L^{\mathrm{pure}\uparrow}$ will, after the tunneling time $t^\uparrow_{\mathrm{tun}}$, contain $R^{\mathrm{pure}\downarrow}$ with the probability amplitude

$$c=\mathrm{i}o\pi(T^\downarrow-T^\uparrow)/4T^\uparrow, \tag{2.43}$$

assuming that the difference in T for different spins is much smaller that T itself.

In the case of zero magnetic field, because of Kramer's degeneracy, the tunneling frequencies are the same for both spin orientations. Then whatever is the initial combination of spin 'up' and 'down' (let it be, for example, $L^{\mathrm{pure}\uparrow}$), during the time evolution (oscillations) there will be no relative change in the coefficients in this linear combination. Therefore spin-orbit interaction does not lead to spin-flipping and $c=0$ in Eq. (2.43).

In a finite magnetic field, the tunneling frequency for spin 'up' and 'down' are different. The difference is caused by spin-orbit terms only, and is of order $\alpha^{(2)}_-=l_0^2(l_D^{-2}-l_{BR}^{-2})$, see Eq. (2.40) and Fig. 2.14b for numerics. We conclude, that spin-flip during tunneling induced by spin-orbit interaction is proportional to the third power in spin-orbit interactions and depends linearly on the magnetic field if the magnetic field is small $[c\sim(l_0/l_{\mathrm{lin}})^3\theta]$.

The different tunneling frequency can be exploited for separation of different spin states in a homogeneous magnetic field. Starting with some combination of 'up' and 'down' states localized in one dot, after time $t_{\rm sep} = h/2(T^{\uparrow} - T^{\downarrow}) = t_{\rm tun}T^{\uparrow}/(T^{\uparrow} - T^{\downarrow})$ the part with spin 'up' will be localized in the left, and the spin 'down' will be in the right dot. From Fig. 2.14 one can see that about 10^3 coherent oscillations are needed to get the spatial spin separation. Although the relaxation and decoherence times for spin-flip in quantum dots (of the order of 1 ms - 1μs [21, 98]) are much longer than the separation time, for this scheme to work we need to retain also the orbital coherence during the separation. The orbital relaxation time is comparable to the separation time (0.1 ns in[145]). We note that the separated states will not be pure spin states, but will contain a small (linearly proportional to l_{SO}^{-1}) admixture of opposite pure spin states.

2.6 Summary: effective Hamiltonian, perturbative eigenfunctions

The numerical results of previous sections can be reproduced qualitatively from the lowest order of the perturbative solution of the Hamiltonian Eq. (2.2). We derive an effective spin-orbit Hamiltonian, with the help of which the spin-orbit influence on the energies and wavefunctions can be understood.

2.6.1 Effective spin-orbit Hamiltonian

We assume that the spin-orbit interaction is a small perturbation and that one can solve the Schrödinger equation for Hamiltonian $H_0 = T + V + H_Z$. As already mentioned, the analytical solution of H_0 for the single dot case is known – the Fock-Darwin states, $\Psi_{n,l,\sigma}$, where n is the principal quantum number, l is the orbital quantum number, and σ is the spin. For the double dot case the analytical solution is not known, but for our double dot potential the eigenfunctions can be approximated by a properly symmetrized linear combination of Fock-Darwin functions centered at the potential minima, see Eq. (2.21).

It is useful to unitary transform[5] the Hamiltonian to remove the linear spin-orbit terms

$$H \to H' = e^{H^{op}} H e^{-H^{op}} = H_0 + H_1, \tag{2.44}$$

where

$$H_1 = H_{D3} + H_{\rm lin}^{(2)} + H_Z^{(2)} + H_{D3}^{(2)} \tag{2.45}$$

is an effective spin-orbit interaction. In addition to the cubic Dresselhaus term

H_{D3}, H_1 comprises the following parts:

$$\begin{aligned} H_{\rm lin}^{(2)} &= \frac{\hbar}{4m}\left(l_D^{-2}-l_{BR}^{-2}\right)\sigma_z L_z - \frac{\hbar^2}{4m}\left(l_D^{-2}+l_{BR}^{-2}\right), && (2.46)\\ H_Z^{(2)} &= -\mu B_{||}\sigma_z(xh_1^x+yh_1^y)+\mu B_\perp(x\hat{h}_2^x+y\hat{h}_2^y), && (2.47)\\ H_{D3}^{(2)} &= -\frac{\gamma_c}{4\hbar^3 l_{BR}}\left[4\hbar P_xP_y-\sigma_z(\{y,P_yP_x^2\}-\{x,P_xP_y^2\})\right]- \\ &\quad -\frac{\gamma_c}{4\hbar^3 l_D}\left[\hbar\mathbf{P}^2+\sigma_z(\{x,P_yP_x^2\}-\{y,P_xP_y^2\})\right]+H.c.. && (2.48)\end{aligned}$$

Higher order terms were omitted in H_1. The curly brackets denote the anticommutator. Vectors $\mathbf{h_1}$ and $\hat{\mathbf{h}}_\mathbf{2}$ are effective spin-orbit vectors due to in-plane ($B_{||}$) and perpendicular ($B_\perp$) components of the magnetic field:

$$\begin{aligned} h_1^x &= l_{BR}^{-1}\cos\gamma - l_D^{-1}\sin\gamma, && (2.49)\\ h_1^y &= l_{BR}^{-1}\sin\gamma - l_D^{-1}\cos\gamma, && (2.50)\\ \hat{h}_2^x &= l_{BR}^{-1}\sigma_x - l_D^{-1}\sigma_y, && (2.51)\\ \hat{h}_2^y &= l_{BR}^{-1}\sigma_y - l_D^{-1}\sigma_x. && (2.52)\end{aligned}$$

In previous we had positioned the vector connecting the double dots to be parallel to the crystallographic x axis. For a general orientation of the double dot, to take advantage of the spatial symmetry of the confinement we need to rotate the (originally crystallographic axes) coordinates such that the new $\hat{x}$ lies along $\mathbf{d}$. The coordinates change accordingly to

$$x \to x\cos\delta - y\sin\delta, \quad y \to y\cos\delta + x\sin\delta, \qquad (2.53)$$

and similarly for P_x and P_y. The rotation leaves Eq. (2.46) unchanged. In Eq. (2.47) the effective linear spin-orbit couplings $\mathbf{h_1}$ and $\hat{\mathbf{h}}_\mathbf{2}$ are renormalized and similarly are the prefactors in Eq. (2.48). We will give explicit results of the rotation later, when particular terms are needed.

The influence of the spin-orbit interactions on the state energy can be understood by looking at the effective spin-orbit Hamiltonian. The spin-orbit correction to the energy of a state Γ_i is in the lowest order given by $\langle\Gamma_i|H_1|\Gamma_i\rangle$. Since at zero magnetic field the states of the double dot belong to a particular symmetry representation of C_{2v} and have definite x and y symmetries, the only consequence of the linear spin-orbit terms, Eqs. (2.46)-(2.47), is a constant shift. Therefore the tunneling is not changed by the linear spin-orbit terms in the lowest order. Only in the true single dot case the operator L_z in Eq. (2.46) shifts the energy of a state according its orbital quantum number, as was discussed when explaining Fig. 2.9. In the double dot regime the dominant spin-orbit correction in zero perpendicular magnetic field comes from operator $\mathbf{P}^2$ in Eq. (2.48) which has symmetry Γ_1, as seen in Fig. 2.8. If the magnetic field has finite perpendicular component, the dominant contribution to both the tunneling and g-factor comes from L_z operator (having now symmetry Γ_S) in Eq. (2.46), as shown in Fig. 2.11.

2.6.2 Perturbative expressions for eigenfunctions

In next chapters we will also need, apart form energies, the explicit form of the wavefunctions. Again, the lowest order of the degenerate theory allows to get analytical results close to numerics. We use the notation for the eigenfunctions and eigenenergies of H_0 from Sec. 2.5.1 and Eq. (2.31), meaning an eigenfunction of the full transformed Hamiltonian H' is denoted by an overline and can be written as a combination of the solutions of H_0 which are denoted by Γ. The four lowest states (the ground state and the lowest orbital excited state, both with spin up and down) in the lowest order of the degenerate perturbation theory are

$$\begin{aligned}
\overline{\Gamma}^{00}_{1\uparrow} &\approx \Gamma^{00}_{1\uparrow} + \frac{\langle \Gamma^{10}_{2\downarrow} H_1 \Gamma^{00}_{1\uparrow}\rangle}{E^{00}_{1\uparrow} - E^{10}_{2\downarrow}} \Gamma^{10}_{2\downarrow} + \ldots, && (2.54)\\
\overline{\Gamma}^{00}_{1\downarrow} &\approx \alpha\Gamma^{00}_{1\downarrow} + \beta\Gamma^{10}_{2\uparrow} + \frac{\langle \Gamma^{11}_{4\uparrow} H_1 \Gamma^{00}_{1\downarrow}\rangle}{E^{00}_{1\downarrow} - E^{11}_{4\uparrow}} \Gamma^{11}_{4\uparrow} + \ldots, && (2.55)\\
\overline{\Gamma}^{10}_{2\uparrow} &\approx \alpha\Gamma^{10}_{2\uparrow} - \beta^*\Gamma^{00}_{1\downarrow} + \frac{\langle \Gamma^{11}_{4\downarrow} H_1 \Gamma^{10}_{2\uparrow}\rangle}{E^{00}_{2\uparrow} - E^{11}_{4\downarrow}} \Gamma^{11}_{4\downarrow} + \ldots, && (2.56)\\
\overline{\Gamma}^{10}_{2\downarrow} &\approx \Gamma^{10}_{2\downarrow} + \frac{\langle \Gamma^{00}_{1\uparrow} H_1 \Gamma^{10}_{2\downarrow}\rangle}{E^{10}_{2\downarrow} - E^{00}_{1\uparrow}} \Gamma^{00}_{1\uparrow} + \ldots, && (2.57)
\end{aligned}$$

where the dots denote the rest of an infinite sum through the eigenfunctions of H_0. The anti-crossing of states $\Gamma^{00}_{1\downarrow}$ and $\Gamma^{10}_{2\uparrow}$ is described by coefficients

$$\begin{aligned}
\beta &= \mathrm{Arg}(\triangle\,\delta E)\sin[\arctan(|4\triangle/\delta E|)/2] = \\
&= \mathrm{Arg}(\triangle\,\delta E)\sqrt{\frac{1}{2} - \frac{|\delta E|}{2\sqrt{\delta E^2 + |2\triangle|^2}}}, && (2.58)\\
\alpha &= \sqrt{1-|\beta|^2} = \sqrt{\frac{1}{2} + \frac{|\delta E|}{2\sqrt{\delta E^2 + |2\triangle|^2}}}, && (2.59)
\end{aligned}$$

which depend on the energy difference $\delta E = E^{00}_{1\downarrow} - E^{10}_{2\uparrow}$ and the coupling $\triangle = \langle \Gamma^{10}_{2\uparrow} H_1 \Gamma^{00}_{1\downarrow}\rangle$ between the unperturbed crossing states. If $|\delta E| \gg |\triangle|$, then $\alpha \sim 1$ and $\beta \ll 1$ – a result of the non-degenerate perturbation theory is recovered. The other case, when $|\delta E| \lesssim |\triangle|$, describes the anti-crossing – the spin hot spot.[60, 61] In the limiting case, when $\delta E = 0$, we get $\beta = 1/\sqrt{2} = \alpha$.

2.7 Conclusions

In this chapter, we have performed numerically exact calculation of the spectrum of a single electron localized by a confining potential in single and double GaAs quantum dots. We have studied the influence of the spin-orbit terms, namely the Bychkov-Rashba and the linear and cubic Dresselhaus terms, on the energy spectrum. In the single dot case we have elaborated on previous results and shown that the spin-orbit interaction has three principal effects on the spectrum: first, the interaction shifts the energy by a value proportional to the second order in the spin-orbit interactions, second, it lifts the degeneracy at zero magnetic field, and, third, the Bychkov-Rashba term gives rise to spin hot spots at finite magnetic fields.

In the double dot case we have addressed the symmetries of the Hamiltonian. For zero magnetic field without spin-orbit terms we have constructed the correlation diagram, between single and double dot states, of the spectrum. We have used a properly symmetrized linear combination of shifted single dot solutions as an approximation for a double dot solution and found that for the four lowest states it gives a good approximation for the energy. As for the contributions to the energy from the linear spin-orbit terms, we have found that in zero magnetic field a typical feature of a double dot is a uniform shift of the energy proportional to the second order in the coupling strengths without any dependence on the interdot distance. This is true also if the potential has lower (or none) symmetry (for example biased dots). Therefore, in zero magnetic field, there is no influence on the tunneling frequency up to the second order in the linear spin-orbit interactions and the dominant contribution comes from the mixed linear and cubic Dresselhaus second order term. We have found, that spin hot spots in zero magnetic field exist in the double dot, but are solely due to the cubic Dresselhaus term. This means also, that for our potential, for the cubic Dresselhaus term there can not exist a unitary transformation to eliminate its contribution in the first order.

The effective g-factor, on the other hand, is influenced by the second order linear spin-orbit interactions even at $B_\perp \sim 0$, so the dominant contribution here is the linear Dresselhaus term for GaAs. In finite magnetic fields the uniform shift does not hold any more and there is a contribution to the tunneling frequency in the second order of the linear spin-orbit interactions. We have derived an effective Hamiltonian, using Löwdin's perturbation theory, with which analytical results up to the second order in perturbations (Zeeman and spin-orbit terms with the exception of cubic Dresselhaus-cubic Dresselhaus contribution) can be obtained provided one has exact solutions of the double dot Hamiltonian without Zeeman and spin-orbit terms. From this effective Hamiltonian we have derived the uniform shift in zero magnetic field. In a finite magnetic field we used linear combinations of single dot solutions to obtain analytical expressions for the spin-orbit contributions to the energy for the four lowest states. We have analyzed them as functions of the interdot distance and magnetic field and compared them with exact numerical values. The spin-orbit relative contribution to the g-factor and the tunneling frequency is of the order of $\sim 10^{-2}$ and $\sim 10^{-3}$, respectively. Due to the degeneracy of the energy spectrum at large interdot distance the spin hot spots exist also at smaller magnetic fields compared to the single dot case.

As an application of our results we have constructed an effective Hamiltonian acting in a restricted Hilbert space of four states – electron localized on either dot with spin up and down (these are effective spins in the presence of spin-orbit interaction). For these effective spins there is only spin-conserving tunneling between the localized states, no spin-flip tunneling. In zero magnetic field the spin-orbit interaction does not significantly influence the tunneling frequency, nor it implies spin-flip tunneling even for Pauli spin states. In finite magnetic fields the tunneling frequency is spin dependent, the difference being of second order in linear spin-orbit terms. This leads to a spin flip amplitude for Pauli spins proportional to the third power in spin-orbit interactions (it is linear in magnetic field). We propose to use this difference of the tunnelings to spatially separate electron spin in homogeneous magnetic field.

Chapter 3

Adding dissipation

In this chapter we study transitions between eigenstates of an electron localized in a quantum dot, which are induced by interactions of the electron with the environment. We first define spin and orbital relaxation and discuss main mechanisms of such relaxation processes in quantum dots. In the second part we review the recent experimental progress in, first, detecting a single spin in solid state environment and, second, measuring the single electron spin relaxation time. In the third part we give our results for electron spin and orbital relaxation induced by acoustic phonons.

3.1 Environment induces transitions

If the electron in the quantum dot is isolated and whole its' interaction with the rest of the world is described by Hamiltonian H, Eq.(2.1), the time dependence of the electron wavefunction is

$$\Gamma(t) = \sum_j \alpha_j e^{-\mathrm{i}\omega_j t} \Gamma_j \tag{3.1}$$

Here, at time $t = 0$ the wavefunction is a certain superposition, given by the coefficients α_j, of eigenstates Γ_j of the Hamiltonian H. The whole time dependence is a phase linearly growing with time and energy of each eigenstate in the expansion. The probability to find the electron in a certain eigenstate will be time independent – there will be no transitions. The electron is however immersed in a condensed matter environment. Phonons, crystal boundaries and imperfections, electromagnetic fields, nuclei magnetic momenta are few examples of entities interacting with the electron whose influence is not included in H. Such interactions will change the electron wavefunction non-trivially. A change is called inelastic if the energy of the electron is changed and elastic if it is not changed. A typical time of an inelastic change is called relaxation time – it is a time over which the modulus of a certain coefficient α_j in Eq.(3.1) is changed appreciably. A decoherence time is a time over which the phase starts to differ considerably from its linear evolution in Eq. (3.1). Such a definition of transition times is not unambiguous. For example, transition times can be different for changes of different coefficients in Eq. (3.1) and more time scales expressing the environment influence on the electron are used.[168]

The relaxation and decoherence times are critical parameters determining the possibility to use the electron in a quantum dot as a qubit. If the qubit states encode a classical information, the manipulation has to be accomplished on a much shorter time scale than the relaxation time, after which the information is lost. Requirements on quantum information processing are even more stringent - here the information is encoded also in the phase of states, not only the occupation, therefore the information lifetime is the decoherence time, which can easily be orders of magnitude smaller than the relaxation time. It is thus a crucial task to quantify these timescales and find conditions under which they are maximal.

3.1.1 Spin relaxation

To be able to induce non-trivial time-dependent behavior, the environment has to have dynamical degrees of freedom and has to interact with the electron strongly enough. For the next discussion we take an example of the spin relaxation. This means we consider an initial state of the electron in Eq. (3.1) to be an eigenstate, let it be an excited state, with the projection of the spin along certain axis $-\hbar/2$. We define the spin relaxation time to be a time after which the wavefunction spin projection is $\hbar/2$, let it be the ground state where the electron finally ends. We first discuss phonons as the source of the spin relaxation, since, compared to other environment fluctuations, phonons can not be get rid off in the crystal and define a fundamental upper limit for the spin relaxation time.

Phonons

A phonon is an oscillating wave-like displacement of the crystal atoms from their equilibrium positions. With such a displacement, the energy of the electron is changed due to the changed band structure. This is known as deformation potential. If the crystal is piezoelectric, the deformation of the crystal lattice induces an electric field which interacts with the charged electron – piezoelectric potential. If the crystal atoms are ions, a relative displacement of charged ions also induces the electric field – Fröhlich coupling. All three listed interactions[77, 114] can be viewed as an electric field induced by phonons. However, the electric field does not couple directly to the electron spin. A further spin dependent mechanism is needed for transitions which do not preserve the electron spin. Such mechanisms can be divided into two main groups.[97, 98, 96]

First, suppose there is a term in the electron Hamiltonian which does not allow to define a common spin quantization axis – it either does not commute with the Zeeman term, or mixes the spin and orbital degrees of freedom. The most important example is the spin-orbit interaction. Then the electron eigenstates are not exactly Pauli spin like. However, one can always attach labels to a state, such as “spin up” or “spin down”, according to the state spin expectation value along the applied magnetic field. If the spin-orbit interaction is small, what is usually the case, such “spin” will be well defined since the spin expectation values will be close to $\pm\hbar/2$. A “spin down” state is in fact a Pauli spin down state plus a small amount of Pauli spin up state. This small admixture of Pauli spin opposite state allows the transition to a “spin up” through spin preserving phonons and gives the name to the admixture mechanism.

Second, say one neglects the influence of the spin mixing terms in the electron Hamiltonian and considers the electron eigenstates to be Pauli spins. The phonon can, under certain conditions, induce spin dependent coupling to the electron[68] called direct spin-phonon coupling. This happens if the environment where the electron is localized is anisotropic in such a way that the phonon induces fluctuations of the parameters of the spin-dependent part in the electron Hamiltonian. An anisotropic g-factor is the most natural example.[24] The phonon induced electric field induces a spin-orbit coupling[4] in a similar way as the electric field from the confinement has induced the Bychkov-Rashba interaction. At the heterostructure interface, phonon will induce fluctuation of every parameter in the electron Hamiltonian which is different in the two materials forming the heterostructure – ripple coupling.[101, 164, 3] A phonon modulation of hyperfine coupling is another possibility.[142]

Phonons are usually described as bulk with the corresponding power law dependence of the density of states. The bulk model is justified for phonons in quantum dot, unless the acoustic properties in the vicinity of the dot are strongly anisotropic. A counter example is a dot located in a small sustained slab, where the discreteness of the phonon density of states, as a consequence of the boundary conditions,[36] is observable in the electron spin relaxation time.[111] Most experiments dealing with single electron quantum dots were done at very low temperature (mostly under one Kelvin, at maximum at 4.2 Kelvins) where the single phonon processes dominate. At higher temperatures (say tens of Kelvin) multi phonon processes have to be taken into account.[146]

The role of phonons can be taken over by fluctuations of the electric potential of the leads defining the electron confinement[116, 16] or the background charge fluctuations.[72] Similar is the absence of the direct coupling to the electron spin and the main difference is the density of states – while phonons density drops with smaller phonon energy as a power law, the leads’ potential fluctuation are mostly described as a white noise with a constant spectral density. Other baths can play role, such as ohmic fluctuations from a nearby current and 1/f background charge fluctuations.[137] In analogy with the phonons, also the fluctuating fields can couple to the electron spin directly: time dependent currents in the leads induce magnetic field, the spins of the electrons in the leads interact with the electron through the exchange interaction (which requires the overlap of the confined and lead electrons) or dipole-dipole coupling[125] (no overlap is needed).

Atomic nuclei

The second very important spin relaxation source are magnetic moments, if present in the area of the quantum dot. They have dynamical freedom and couple directly to the electron spin through the dipole interaction. In magnetic diluted semiconductors, electrons confined at some crystal atoms have unpaired magnetic moments.[165] However, even in non-magnetic materials an important spin thermal bath is present if some of the constituent atoms of the material have nucleus magnetic moments. It would seem that nuclei spins are much more efficient in spin relaxation than second-order processes including spin-preserving phonons. Fortunately from the perspective of long spin relaxation time, the energy conservation blocks a direct process where the electron and a nucleus flip their spins, since the electron and nucleus magneton differ by a factor of ~ 2000. Another coacting interaction, for example, electron-phonon, is thus needed for providing the energy conservation.[59, 1]

Compared to phonons in the previous section, now the thermal bath elements (the nuclei spins) are static in space. Several timescales[117] can be identified in the mutual interaction between the electron and an ensemble of nuclei spins – a typical electrically defined quantum dot in GaAs contains $\sim 10^5$ of nuclei spins. The fastest timescale, being ~ 1 ns, is the precession time of an electron spin in the magnetic field of the nuclei spins. On this timescale, the nuclei spins can be considered frozen and described by an effective magnetic field, leading to the electron spin relaxation[58] and decoherence.[95, 30]

The second time scale is the time of precession of a nucleus spin in the magnetic field of the electron, being three orders of magnitude smaller due to smaller nuclei magneton. A simultaneous flip of the spin of both the electron and a nucleus flip can be used for a dynamical polarization of the nuclei spins.[50, 109] Due to the large number of the nuclei spins, some sort of a cut-off scheme is inevitable for analytical description of such mutually influencing nuclei-electron dynamics. Taking into account only pair wise interactions of the electron spin with a picked nucleus,[39] instead of considering the whole set of nuclei spins, seems a possible way. A systematic formulation of such approximation was recently done by a cluster expansion.[163]

The slowest important time[87] is a nucleus spin precession in the dipole magnetic field of neighbor nuclei, being ~ 100 μs. It is responsible for the thermalization of the nuclei spins and can be viewed as spin diffusion. The electron in the quantum dot strongly influences this diffusion,[113, 38] but for the back action of the diffusion on the electron, no theoretical work exists, apart from an exact numerical simulation that can encompass only up to 20 nuclei spins.[45] In experiments,[124] one has observed a complicated electron behavior over long-times, mirroring the mutual influence between the three discussed processes with different time-scales.

The most important channel how the nuclei spins cause the electron decoherence is due to non-uniform hyperfine couplings induced by space dependence of the electron wavefunction. Based on this finding, several schemes were proposed to suppress this decoherence channel by polarization or narrowing the quantum state of the nuclei spins.[147, 99]

Dominant channels

While many possible ways of spin relaxation exist, fortunately only few of them turn out to play an important role. It is agreed that in magnetic fields above ~ 1 Tesla, the acoustic phonon combined with the admixture mechanism due to the spin-orbit coupling is the dominant channel for the spin relaxation. The spin relaxation time is of order of 0.1 ms and analytical results fit experiments neatly.[6] The spin relaxation rate is greatly enhanced[21] nearby an anti-crossing where the spin-orbit influence on the electron spin is much more profound. The anisotropy of the spin-orbit terms with respect to the crystallographic axes leads to dependence of the spin relaxation rate on the orientation of the magnetic field[75] or electron momentum[9] (the latter is meaningful only for electrons in a quantum well) which can be used to control the spin relaxation. Another possibility of control is to use the dependence of the phonon density on the energy.[162] If the spin-orbit interaction can not be considered as a small perturbation the spin relaxation shows complicated behavior.[41] Despite its practical perspectiveness, spin relaxation in quantum dots in silicon attained much less theoretical attention[2, 149] than in III-V compounds, such as GaAs, because the analysis for silicon is complicated by the degeneracy of the bands minima.

In sub-Tesla fields nuclei spins combined with phonons are believed to dominate the spin relaxation. However, only a preliminary experimental data exist in this range of the magnetic field and the analytical predictions can not be verified yet. It is believed that also the decoherence is dominated by the interaction of the electron with the nuclei spins, for which spin echo[128] and a suppression of the decoherence by magnetic fields[92] seem to be strong indications.

Spin relaxation in two electron QD

From the quantum computation point of view the most interesting case is the spin relaxation in a two electron quantum dot – a transition between singlet and triplet states. Surprisingly, it still lacks a comprehensive quantitative analysis. In a parabolic quantum dot the linear spin-orbit terms couple the ground state to different states according selection rules,[29] which are loosen if the potential looses the circular symmetry.[66, 65] The recent experiment[118] suggests that the double electron case is not qualitatively different from the single electron case. Further analytical work is needed to clarify the role of cubic Dresselhaus spin-orbit term, influence of the higher excited states,[29] appearance of a new spin-orbit interaction originating in the Coulomb electric field[11] or the possible non-spin-orbit origin of the spin relaxation.[86]

3.1.2 Orbital relaxation

To complete the discussion, we now shortly comment on transitions between spin alike electron states which are not blocked by the spin conservation. The above discussed spin-dependent mechanisms can be neglected and the transition is induced by any fluctuation producing electric field. The main possible sources of such fluctuations are phonons, potential of the circuitry (confinement gates, measuring units like a quantum point contact), heterostructure background charge fluctuations,[64] and interactions with the leads if the dot is opened and the current is allowed to flow through. Apart from phonons, the previous mechanisms can be suppressed: improving the circuit, putting the dot farther apart from the doped region, lowering the current through the dot, respectively, for the three listed sources. Phonons are always present and can be regarded as principally the dominant source of the orbital relaxation. The single electron relaxation time due to phonons is mainly given by the energy difference between the initial and final state. Other details, such as the shape of the potential and the magnetic field, have only minor influence. Apart from the single dot confining energy, in the double dot there is an additional handle to influence the relaxation – the distance between the two potential minima.[63, 145] If the dot is populated by more electrons, the transition rates tend to decrease comparing to single electron case, since the Coulomb interaction mixes the lowest states with higher single electron orbitals.[14, 28]

Concerning the orbital decoherence, it is not dominated by phonons,[159, 110] but the true source of the orbital decoherence is not yet clear, the most probable candidate are circuit potential fluctuations, making the decoherence rate strongly dependent on sample details.

3.2 Experiments on single electron spin relaxation

To measure the electron spin relaxation and/or decoherence time, it is first of all necessary to be able to measure the state of the electron spin. However, the magnetic moment of an electron is very small, making a direct detection of its magnetic field difficult. Even though this direct detection was realized, more convenient methods are usually used. The optical methods based on spin selective optical transition rules are usually used if an ensemble of spins is being studied. On the other hand, in single electron systems, spin to charge conversion schemes are used. They take advantage of the fact that the spin is not completely decoupled from the orbital degrees of freedom and therefore the electron spin state can be deduced by measuring the charge of the system. In fact, here it is used that the spin is just (a part of) the label (quantum numbers) for the electron wave function – different states (wave functions) have all kinds of different properties not connected directly to the spin (energy, spatial extent of the wave function, ...). By measuring these properties, one can deduce about the spin.

In the next sections we present several experiments divided into two groups. We review, first, experiments aiming at a single electron spin detection in solid state environment, and, second, experiments reporting on measurements of the spin relaxation time of few electron states in a quantum dot.

3.2.1 Detecting the presence of a spin

Nuclear magnetic resonance (NMR)

Nuclear magnetic resonance is a long known method of detecting a magnetic moment with very important practical applications. The principle is sketched in Fig. 3.1. A large static magnetic field is applied. The magnetic moments in the sample (being the spins of nuclei of atoms in the material or spins of electrons) align along the applied magnetic field, thus producing a magnetic domain. Then a microwave radiation is applied. If the frequency of the microwave matches the Zeeman splitting of the spins, each spin starts to precess with the Larmor frequency. The rotating magnetic field of the domain at the Larmor frequency is detected. Important thing is that different nuclei have different g factors and therefore can be identified by their characteristic Larmor frequency. A three dimensional images of a bulk sample can be thus obtained. However, the domain has to possess some minimal total magnetic moment, so that it is possible to detect the signal. Nowadays, a smallest domain consists of $\sim 10^{12}$ nuclei or $\sim 10^{7}$ electrons, corresponding to a spatial resolution of several micrometers.

Scanning tunneling microscope (STM)

The scanning tunneling microscope is able to produce images with an atomic resolution. The task was how to make it sensitive to spin, since usually the current extracted from the surface of a sample depends on the local density of states of electrons, but not on their spin. The idea that lead to a successful observation of a single spin on SiO_2 surface[115] resembles the magnetic resonance and is explained in Fig. 3.2. A static magnetic field is applied (a small magnet bars were mounted on the STM tip, producing a field of $\sim 200G$). The electrons extracted from the sample precess in the magnetic field. If there is a confined spin located nearby, one can expect a modulation of the STM current at the Larmor frequency due to an interaction of the static confined spin and the precessing spins of tunneling

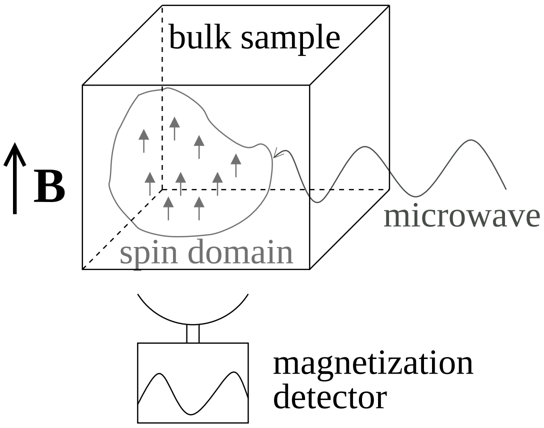

Figure 3.1: Nuclear magnetic resonance. A magnetic domain created in an applied magnetic field precesses if a resonant microwave field is applied. The precession of magnetic moments is detected.

electrons. The modulation of the current was really observed, even though the origin of the spin-spin interaction was not clear. The experiment was done at a room temperature and the spin sensitive signal was observed within a spatial region of $\sim$ 10 Å. Thus STM has proven to be able to see an individual spin, however only if the spin is located near the surface. Later, an observation of a single spin in an organic molecule was done by the same method.[48]

Optical detection of the spin of nitrogen vacancy defect in diamond

The nitrogen vacancy defect is a charged defect produced by an electron irradiation of a diamond sample. The energy level diagram of the defect is in Fig. 3.3a. The ground state, denoted as ^{3}A, includes singlet and triplet states split by a small energy difference, while ^{3}E is an excited state. Important is that only the ground singlet state is active in the dipole optical transition, while the triplet is a dark state.

In the first experiment[78] the sample was irradiated by a resonant laser, driving the optical transition between the ground and excited state. The luminescence was observed through a small aperture behind which a single photon detector was located, see Fig. 3.3b. By lowering the concentration of the defects in different samples, it was possible to get to the regime where a single fluorescing defect was observed. The spatial resolution was $\sim$ 300 nm.

The group worked on the system further and in Ref. [90] they reported on an observation of time dependence of the fluorescence of a single defect, as depicted in Fig. 3.3c. If the signal is being detected (on), it means the laser excites the defect from the singlet ground state, followed by a relaxation back, along with an emitted photon. If there is no signal (off), it means the defect is in triplet ground state and no excitations by the laser are possible. From time to time the system

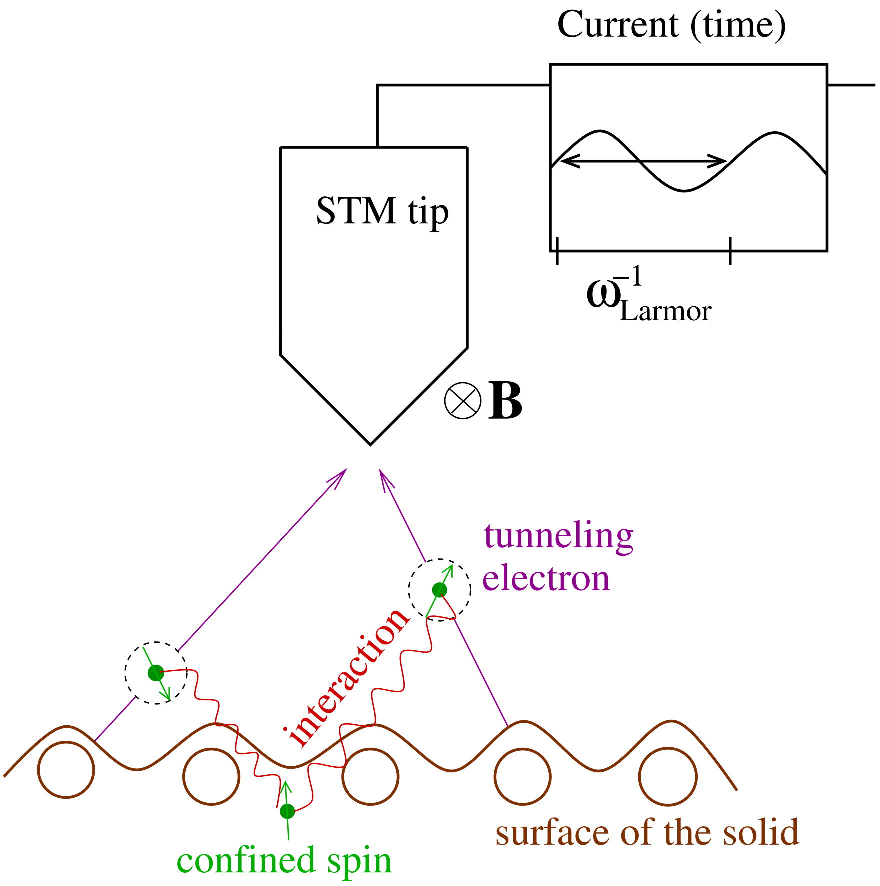

Figure 3.2: Observation of a single spin located on a surface of a sample by the scanning tunneling microscope. The tunneling electrons precess in the magnetic field nearby the STM tip. Interaction between these precessing spins and a spin located at the surface modulates the detected signal at the Larmor frequency.

undergoes a spin-flip transition between the ground singlet and triplet states, switching the signal between on and off. The average time between the switches is the spin relaxation time, measured between milliseconds at room temperature and seconds at the temperature of 2K.

In the most elaborated experiment with this system,[89] coherent Rabi oscillations were observed. An applied resonant microwave field induces coherent oscillations between the ground singlet and triplet states, which were again detected by the laser induced fluorescence. The oscillations are damped by the decoherence, as seen in Fig. 3.3d. From the decay of the oscillations a decoherence time of 1 μs at 2K was obtained.

Magnetic resonant force microscopy (MRFM)

The recently invented method of magnetic resonant force microscopy[136] is based on the magnetic resonance, however is capable to detect a single electron spin. The operation principle is demonstrated in Fig. 3.4a. Comparing to the usual magnetic resonance, here the static magnetic field defining the resonant frequency is spatially dependent, allowing to address a specifically located spin. The static magnetic field consists of a uniform external field and a field of a magnetic tip fastened to a cantilever. Similarly as in the usual magnetic resonance a microwave field is applied. The detection of the located spin is done by detecting the spin-spin dipole interaction of the magnetic tip and the located spin. Since this interaction is very small, a delicate method is used. The cantilever oscillates above the located spin. If the microwave field is applied, the located spin undergoes a transition (flip) each time the magnetic field at its position is resonant – that is twice in a period of the cantilever oscillation. Thus the located spin oscillates with the same frequency as is the frequency of the cantilever. This leads to a small difference in the cantilever oscillation frequency depending on the initial state of the spin. Every $\sim$ 100th period the microwave field is turned off leading to an effective flip of the confined spin and a subsequent change in the cantilever frequency. These periodic small changes (mHz) in the frequency of the cantilever (kHz) are detected. In addition to induced spin flips, the spin undergoes intrinsic flips due to the intrinsic relaxation. This is seen as additional random switches of the cantilever frequency. A typical time evolution of the cantilever frequency is in Fig. 3.4b. If the modulation of the cantilever frequency is observed, a confined spin is present in the sample. In addition to a detection of the spin, the intrinsic spin relaxation time of 760 ms (bulk silicon sample was used) was measured from the noise in the cantilever frequency. The great advantage of this method comparing to usual NMR is its resolution (here a single spin can be detected). Comparing to previously demonstrated STM methods, MRFM can detect the spin also underneath the surface.

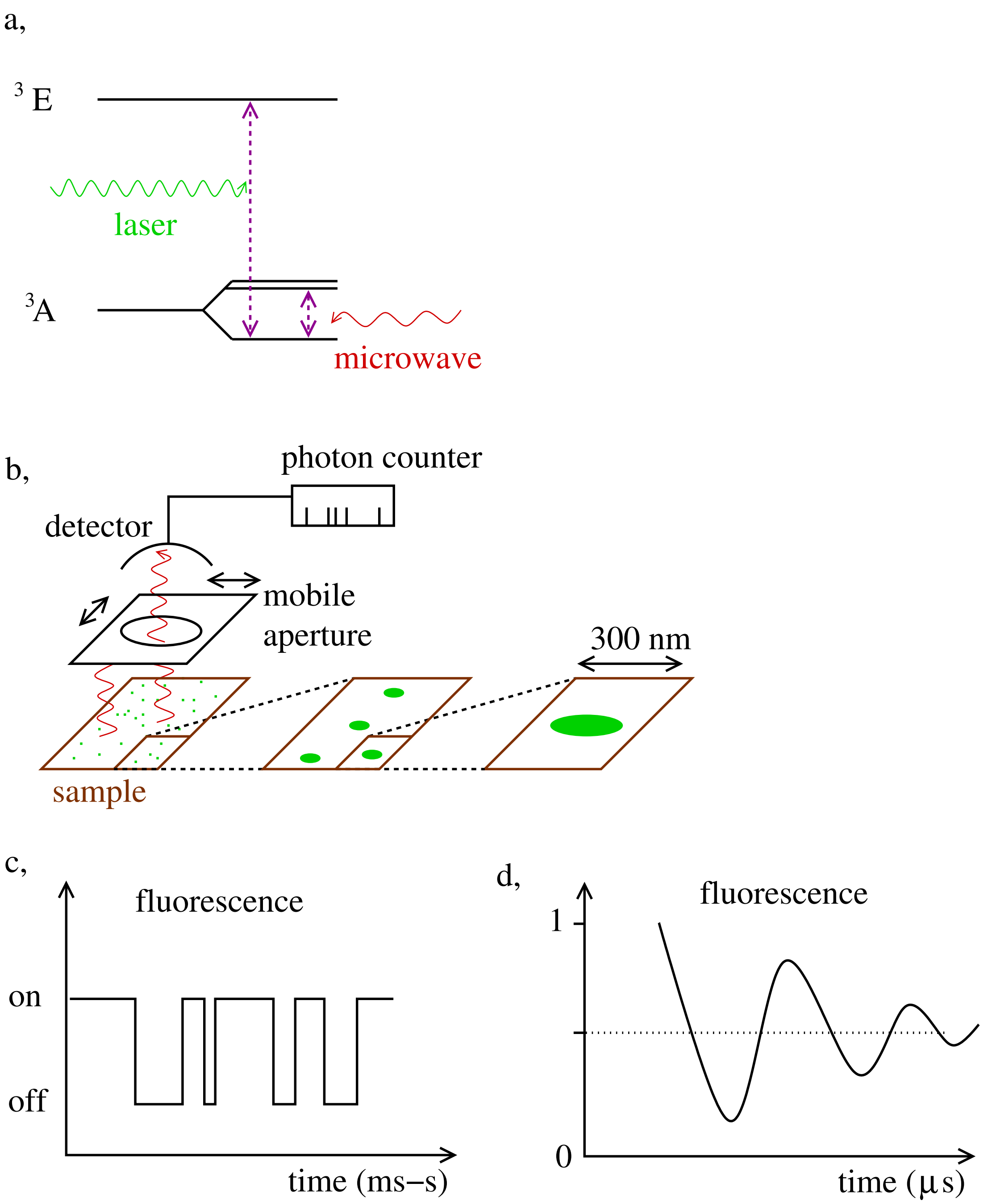

Figure 3.3: Optically detected spin state of a nitrogen vacancy defect in diamond. a, Energy level diagram and the transitions induced by applied fields. b, Detecting an individual center in subsequent samples with diminishing defect density. c, Measuring the spin relaxation time from the switches between the fluorescence signal. d, Measuring the decoherence time from the damping of the Rabi oscillations.

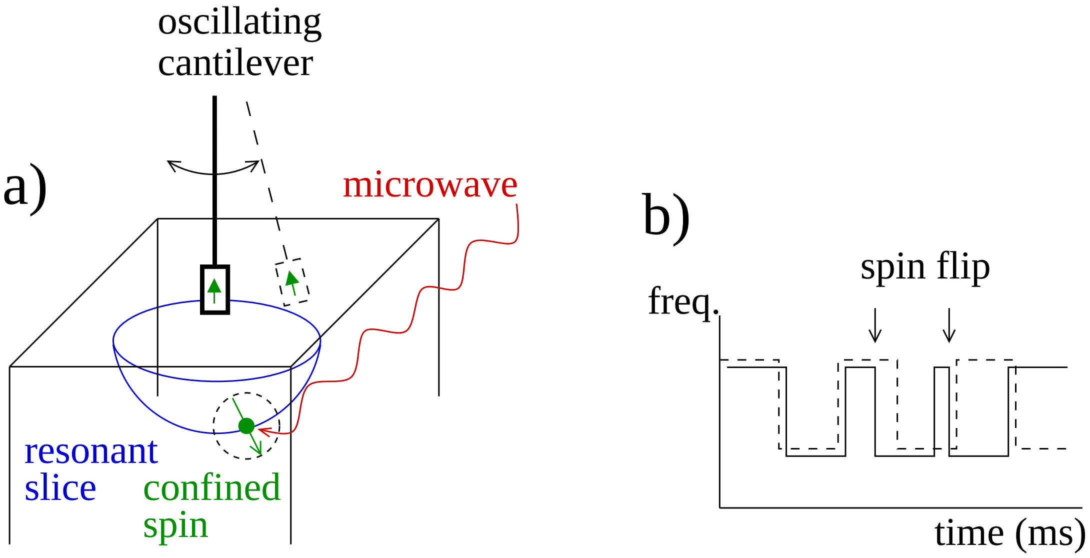

Figure 3.4: Magnetic resonance force microscopy. a, The change of the frequency of mechanical oscillations of a cantilever detects the spin. See text for the explanation. b, Frequency of the cantilever as a function of time: dashed – if no intrinsic spin flips occur, the frequency changes at regular intervals, solid – intrinsic flips bring additional changes at random times.

3.2.2 Measuring spin relaxation and decoherence

Transient current method: two step ERO

A successful measurement of the single electron spin relaxation time in a quantum dot was achieved using a spin to charge conversion method proposed and demonstrated in Ref. [71]. A spin to charge conversion means the spin of the electron is identified by measuring the presence of the electron (that is electrical charge) after a specially designed sequence of voltage pulses applied on the gates. The principle of the method is illustrated in Fig. 3.5. The quantum dot is connected to leads and operated in a regime, where only the ground and first excited states are relevant when considering a possible tunneling through the dot. A two step pulse (a low voltage followed by a voltage enhanced by a certain amount – high voltage) is applied repeatedly. The current through the dot is measured by averaging over many cycles. By changing the basis gate voltage (that is by changing the relative position of the energy levels with respect to the chemical potential of the leads) there are three possible configurations when a current can flow. The first configuration is such that the current flows through the ground state during the high voltage pulse. If the bias voltage is enhanced enough, a second stable configuration is reached, when the current flows through the ground state during the low voltage pulse. For a bias voltage in between these two there is a regime where the current can flow through the excited state during the high voltage pulse. However, now the current flows only until the ground state is populated. If this happens, the current is blocked until the low voltage pulse, when the ground state is emptied and the cycle is repeated. The idea is that by prolonging the time interval of the high voltage pulse, a decay of the transient current should be observed and the relaxation time for the transition from the excited to the ground states could be deduced.

The method is based on the fact that in the transient current regime the ground and excited states are discriminated during the high voltage pulse since they have different energies. In between these energies the chemical potential of the right dot is placed. Only if the electron is in the excited state, it can leave the dot into the right lead and contribute to the current. Since the energy difference is used, the method is called energy resolved readout (ERO). If the excited and ground states have different spins, the method is an example of a spin to charge conversion.

In the transient current configuration, the low voltage pulse is in further denoted as empty step, since the dot, possibly initially occupied, is emptied during this pulse. The high voltage pulse is denoted as probe step, since the state of the electron is measured. Figure 3.6a summarizes the two steps (the fill&wait step will be discussed later). Figure 3.6b introduces definitions of the tunneling rates needed for quantitative description. The relaxation rate from the excited to the ground state is denoted as W, while the tunneling rates to/from the leads are denoted by Γ, with indexes L and R standing for the left and right leads, and E and G for the excited and ground states. It is assumed that the tunneling rates are independent on the applied gate voltage and that the left lead is strongly coupled to the dot, $\Gamma_L \gg \Gamma_R$, W. The lead position defines whether the electron can tunnel to/from the dot. For example, for the probe configuration the electron can tunnel to the excited state only from the left lead, while from the excited state it can tunnel only to the right lead or to the ground state. The last assumption is that there can be only one electron in the dot, meaning the charging energy (the energy needed to add another electron) is much larger than the chemical potentials of the leads. In the probe configuration, populations of the ground g and excited e states are described by the following set of equations:

$$\begin{aligned} \dot{e} &= \Gamma_{LE}(1-e-g) - (\Gamma_{RE}+W)e, \\ \dot{g} &= (\Gamma_{LG}+\Gamma_{RG})(1-e-g) + We. \end{aligned} \tag{3.2}$$

An initial condition of an empty dot ($g = e = 0$) leads to the following approximate solutions (see Appendix .1.1 for the derivation)

$$\begin{aligned} e(t) &\approx \frac{\Gamma_{LE}}{\Gamma_T}\left(1-e^{-\Gamma_T t}\right)e^{-Dt}, \\ g(t) &\approx \frac{\Gamma_{TG}}{\Gamma_T}\left(1-e^{-\Gamma_T t}\right) + \frac{\Gamma_{TE}}{\Gamma_T}\left(1-e^{-Dt}\right). \end{aligned} \tag{3.3}$$

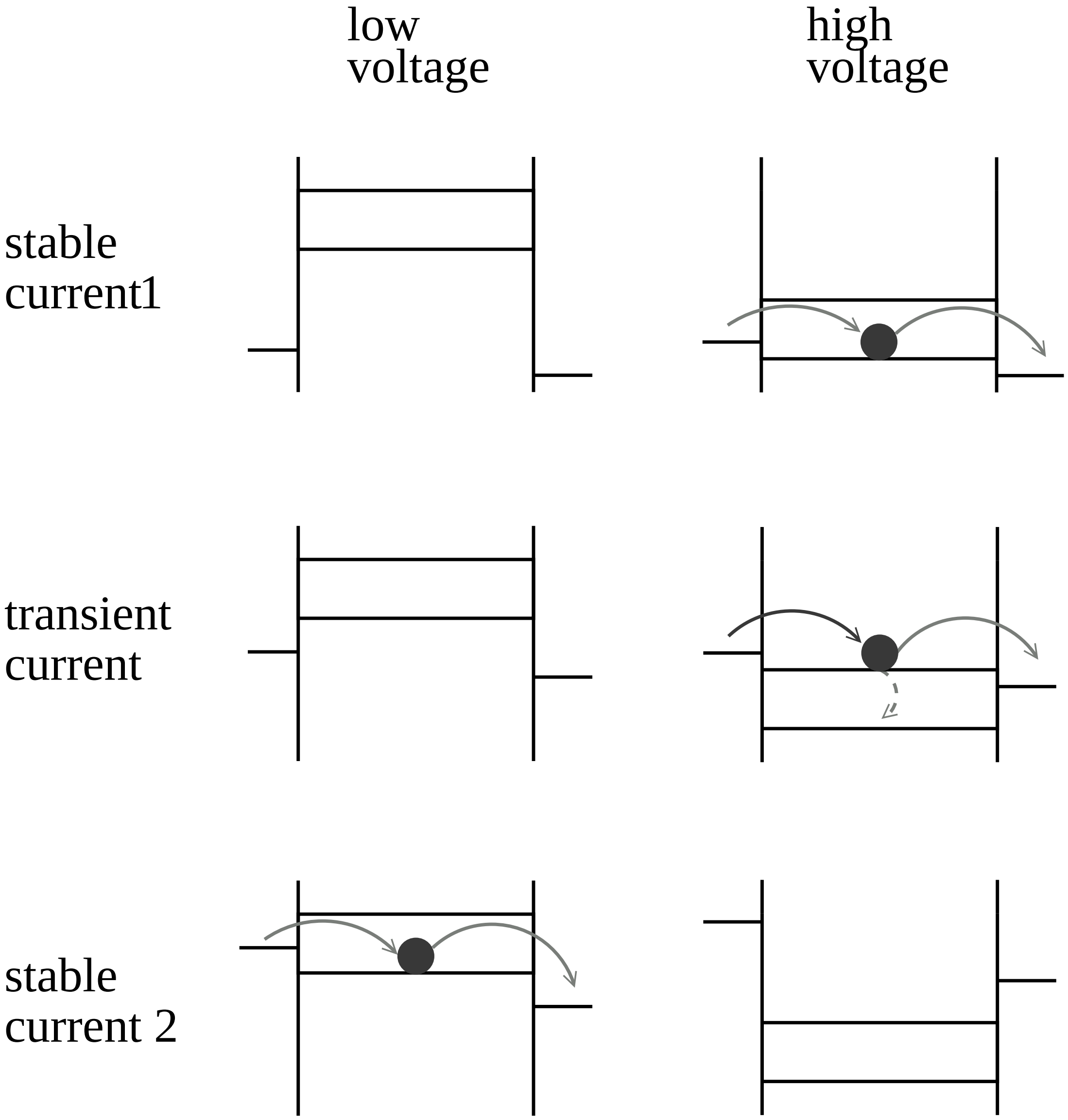

Figure 3.5: Two stable and one transient current configuration for a dot with two voltage steps applied. In the stable current 1 and transient current configuration the current flows during the high voltage pulse, while in stable current 2 configuration during the low voltage pulse.

Here tunneling rates with index T are total tunneling rates for the corresponding state, $\Gamma_{TG} = \Gamma_{LG}+\Gamma_{RG}$, $\Gamma_{TE} = \Gamma_{LE}+\Gamma_{RE}$, $\Gamma_T = \Gamma_{TG}+\Gamma_{TE}$, and D is an effective relaxation rate

$$D = W + \frac{\Gamma_{TG}}{\Gamma_T}\Gamma_{RE}. \tag{3.4}$$

The approximate solutions are written in a form allowing straightforward physical interpretation. Considering an empty dot at time zero, there is an initial filling of the dot due to electron tunneling from the leads. This is a fast process and leaves the states of the dot occupied according to the "filling efficiency" – the average excited state population equals Γ_{LE}/Γ_T, while the ground state is populated with a probability of Γ_{TG}/Γ_T. After this initial filling, the population of the excited state decays in favor of the ground state on a longer time scale, given by the effective relaxation rate D. This rate reveals two ways how an electron can get from the excited state to the ground state. It can either relax directly, happening with a rate W, or it leaves the dot going to the right lead and another electron tunnels into the ground state. This happens with a probability given by the ground state filling efficiency (this process is called direct injection, since the electron gets from the excited state to the ground state not by the relaxation, but by the injection from the lead). In experiments the spin relaxation rate W is usually much slower than the total tunneling rate $\Gamma_T = \Gamma_{TG} + \Gamma_{TE}$ and also the duration of a particular voltage step is much longer than Γ_T^{-1}. Then the terms decaying with the rate Γ_T (that is the initial filling) are not resolved and only the trade off between the excited and the ground state is observed.

ERO: third step introduced

From Eq. (3.4) it follows that the intrinsic relaxation rate W, one is interested in, can be extracted only if it is not much smaller than the direct injection rate. This is why there was an intermediate step introduced in Ref. [69]. It is denoted as "fill&wait" in Fig. 3.6, and is such that both ground and excited states are below the chemical potential of the right lead. The dot, if empty, is filled by an electron from one of the leads. In an analogous way to the probe configuration, the equations for the time evolution of the population during the fill&wait step are

$$\begin{aligned} \dot{e} &= (\Gamma_{LE} + \Gamma_{RE})(1 - e - g) - We, \\ \dot{g} &= (\Gamma_{LG} + \Gamma_{RG})(1 - e - g) + We. \end{aligned} \tag{3.5}$$

The solution, again for the initial condition of an empty dot (see Appendix .1.2), is

$$\begin{aligned} e(t) &\approx \frac{\Gamma_{TE}}{\Gamma_T}\left(1 - e^{-\Gamma_T t}\right) e^{-Wt}, \\ g(t) &\approx \frac{\Gamma_{TG}}{\Gamma_T}\left(1 - e^{-\Gamma_T t}\right) + \frac{\Gamma_{TE}}{\Gamma_T}\left(1 - e^{-Wt}\right). \end{aligned} \tag{3.6}$$

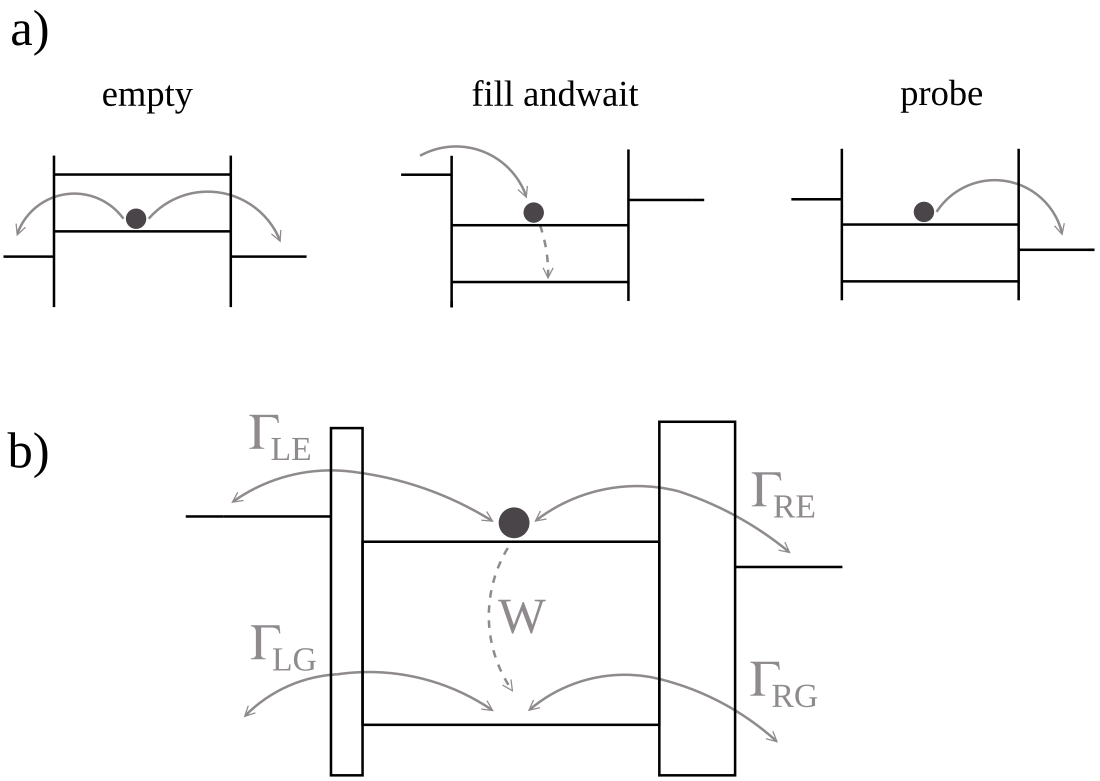

Figure 3.6: a, Relative positions of the energy levels and chemical potentials of the leads for the three steps in energy resolved readout. b, Tunneling rates between the leads and the dot. The first index denotes the lead (left or right), while the second denotes the state of the dot (ground or exited). The relaxation rate from the excited to the ground state is denoted as W. The right barrier is much thicker than the left one.

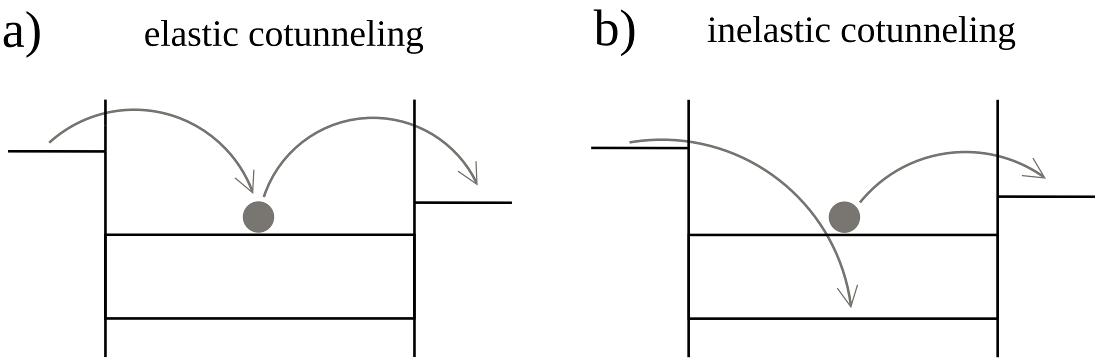

Figure 3.7: Elastic and inelastic cotunneling as a second order tunneling process. a, In the elastic cotunneling the electron initially in the dot tunnels out while another electron tunnels simultaneously into the same state. In inelastic cotunneling the incoming electron enters into a different state of the dot.

The behavior of the system is very similar to the probe configuration – there is an initial fill up on the timescale given by Γ_T^{-1}, followed by the exchange of the excited and ground state populations. However, now the electron, once captured in the dot, cannot escape. Therefore the relaxation rate is not renormalized and the effective (that is measured) relaxation rate equals the intrinsic relaxation rate W. The excited population is measured during the probe step – only if the electron is in the excited state, it tunnels out to the right reservoir, contributing to the current. If it has relaxed to the ground state, it can tunnel out only during the empty phase. If the ratio of the total left and right tunnel rates is the same in the empty and fill&wait steps, on average the electrons tunnel back to the same lead from which the it had entered the dot during the fill&wait step – these back and forth tunnelings result in no net contribution to the measured current.

To complete the picture, the effective relaxation in early experiments using ERO was dominated by cotunneling. This is a quantum mechanical process, thus not included in our classical description in Eq. (3.2), illustrated in Fig. 3.7. Here an electron being in the ground state can tunnel out while another electron from a lead tunnels in *simultaneously*, to the same (elastic cotunneling) or possibly into a different state of the dot (inelastic cotunneling). This process is of the second order in the tunneling rates. For our purposes here the case of interest is when the initial electron is in the excited state, while the replacing electron tunnels into the ground state, contributing to the relaxation. The elastic cotunneling is not capable to relax the electron, but the phase of the incoming electron can be different compared to the phase of the electron initially in the dot. Therefore, elastic cotunneling contributes only to the decoherence.

ERO: experimental results

The method of the transient current was proposed and demonstrated at by Fujisawa et al at NTT Corporation in Japan.[71] In that experiment a lateral quantum dot contained ~ 50 electrons and the only successful relaxation time measured was 3 ns, attributed to an orbital relaxation process. In other cases the effective relaxation was either too slow to give a clear decay or too fast to give a measurable current. The group has pursued this method further – in Ref. [70] they got an upper limit for a spin relaxation time of 2μs and a result of 2 ns for the orbital relaxation time in a lateral dot. The experiment was done also with a single electron vertical dot, however, all the extracted relaxation times were dominated by the direct injection, again giving only an upper limit for the spin relaxation of 1 μs. After introducing the fill&wait step in Ref. [69] it was possible to get rid of the direct injection contribution. The experiment was done with a single and two electrons in a vertical dot in magnetic field of 0-7 T applied perpendicularly. A singlet-triplet relaxation rate of 100 μs was obtained, however it was suspected that it was dominated by the cotunneling. The group finally succeeded in obtaining the singlet-triplet spin relaxation time of 200 μs in Ref. [140], where they measured the spin relaxation at different tunneling rates. Since the cotunneling scales as the tunneling rate squared, it was possible to exclude the cotunneling contribution. This experiment was done in a lateral single dot with ~ 8 electrons in a perpendicular magnetic field up to 3 T. In this experiment, they also observed a narrow dip in the spin relaxation time, being possibly due to an anti-crossing enhancement of the relaxation rate. This is to our knowledge the only experimental observation of such a steep dip in the relaxation rate up to now.

QPC – break through in ERO

Even a measurement of the spin relaxation of few electron states using the transient current method was successful in vertical quantum dots, it turned out to be impossible to realize in lateral quantum dots. A crucial problem is that the tunneling rates into/out of the lateral dot get too small if the dot is forced to be occupied by a small number of electrons. In such a case the cotunneling contribution to the relaxation rate is negligible, but the current through the dot is too small to be measured. This problem was solved by using a quantum point contact (QPC) as a detector of the charge of the dot instead of measuring the current through the dot. The resolution of the QPC detector is quite below a unit charge ($\sim$0.1 e) and thus the single electron tunneling into/out of the dot can be resolved. The QPC was used as a counter for each single electron tunneling event.

Namely, each time the electron tunnels into (out of) the dot, the QPC current is suppressed (enhanced) by a certain amount. In Fig. 3.8 a typical time trace of

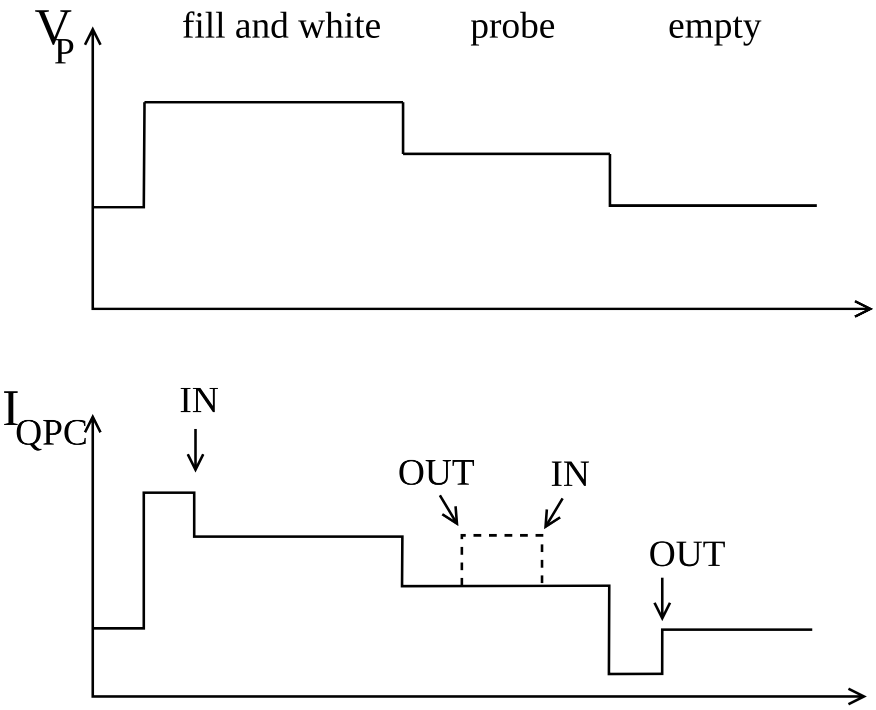

Figure 3.8: Time dependence of the QPC signal during the three step ERO sequence. See text for the explanation.

a QPC current during the three steps of ERO is sketched. An electron enters the dot, which is being initially empty, during the fill&wait step, what is observed as a decrease of the QPC current. If in the excited state, the electron tunnels to the right lead during the probe step and another one tunnels into the ground state, what is observed as a temporary enhancement of the QPC current. If the electron had relaxed during fill&wait step, or entered the dot into the ground state, no enhancement is observed during the probe step. Finally, the dot is emptied during the empty step, observed as an increase of the QPC current and the cycle is restarted. The current through the dot can be obtained by counting the tunneling electrons. In addition, tunneling rates can be deduced by averaging the corresponding time for a particular tunneling to occur. The time resolution of the QPC current signal is ~10 μs, therefore all relevant events to be resolved must happen on a longer time.

ERO+QPC: experimental results

The first experiment measuring the spin relaxation rate using ERO and QPC was done in Delft.[82] The average number of electrons tunneling through the dot in the probe step (lasting for time t_p) is

$$\langle n_E \rangle = \int_0^{t_p} \Gamma_{RE} e(t)\, \mathrm{d}t \approx \Gamma_{RE} \frac{\Gamma_{TE}}{\Gamma_T} \left(1 - e^{-Dt}\right)/D. \tag{3.7}$$

The effective tunneling rate D, Eq. (3.4), was found by fitting the exponential decay, Eq. (3.7). It has been found that the effective rate was dominated by the direct injection and the three step pulse was applied to extract the intrinsic relaxation rate. A simple exponential decay is supposed to be observed, if the current is normalized in the following way

$$\frac{\langle n_E(t_p) \rangle}{\langle n_E(0) \rangle} = e^{-Wt}. \tag{3.8}$$

No decay was detected up to the measurement precision, giving an upper limit for the spin relaxation of 50 μs. In this experiment a parallel magnetic field of 6-14 T was applied to energetically resolve the spin excited state from the ground state. Only in the next experiment[51] the Delft group succeeded in measuring the spin relaxation of a single electron in a single lateral quantum dot (the first successful measurement of this kind). The dot was connected to one reservoir only and the three step voltage pulse was applied. The spin relaxation times of 850 μs, 550 μs, and 120 μs in magnetic fields 8, 10, and 14 T, respectively, were obtained.

A drawback of the ERO method is that for the readout the energy difference has to be large enough to overcome the blurring of the levels due to a finite temperature and shifts of the levels due to background charge fluctuations. Since the Zeeman energy is small, a high magnetic field is required for ERO. In the first experiments of the Delft group the minimal magnetic field was ∼6 T. Very recently[6] the minimal magnetic field for ERO was pushed down to 1.7 T. The improvement was achieved by periodic monitoring and appropriately correcting the shifts of the positions of the energy levels due to the background charge fluctuations. This experiment so far covers the largest range of the magnetic fields and is in a very good agreement with a theoretical prediction for the spin relaxation due to the spin-orbit interactions and acoustic phonons.

Transient current in small magnetic field: TRRO

A different spin to charge conversion scheme was proposed for a measurement of the spin relaxation time in small magnetic fields.[54] The readout of the electron state in the probe step is possible if the tunneling rates for the spin up and down states are different. In the energy readout the tunneling rate out of the ground state during the probe step was strictly zero, since it was under the chemical potential of the right dot. Now both states are above, as depicted in Fig. 3.9, but the rates are different. For two electron states, the difference in the rates

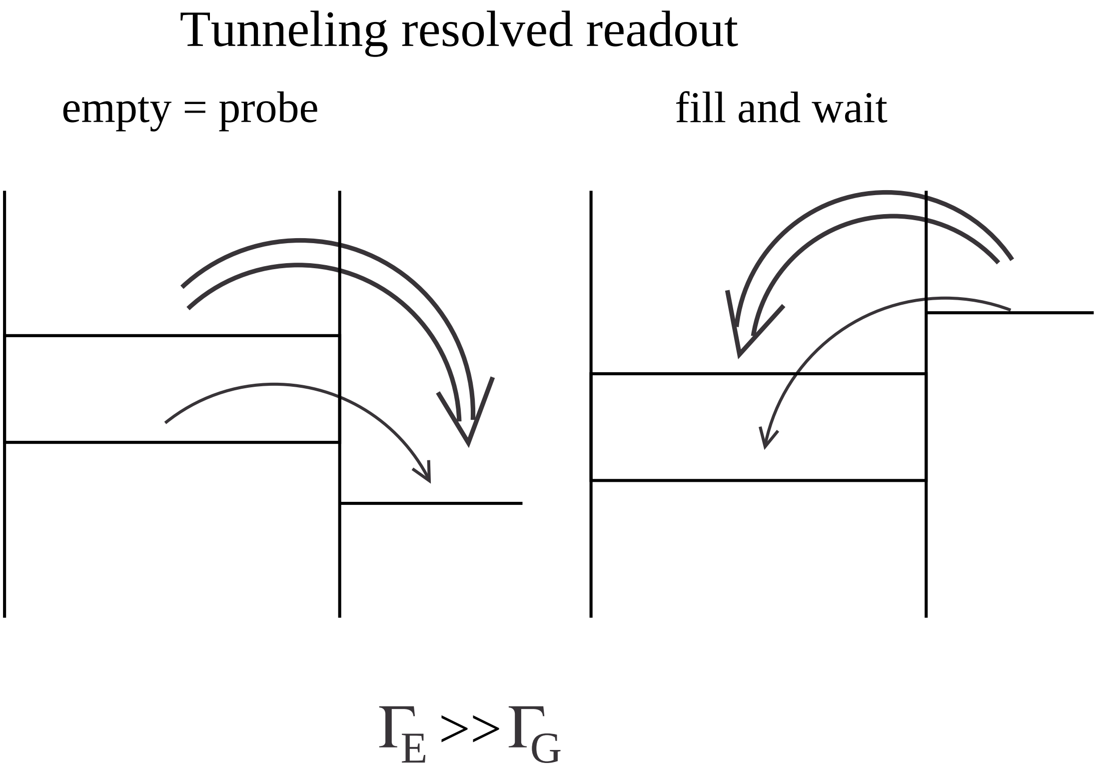

Figure 3.9: Two steps in tunneling resolved readout scheme. The tunneling rates are different for the ground and excited states even if both states are under/above the chemical potential of a lead. In such a case the empty and probe steps can be merged.

originates in the fact that the triplet state is spatially more extended (being antisymmetric) than singlet, leading to a larger overlap with the states in the lead. Thus this method is not straightforwardly applicable to a single electron quantum dot.

In Ref. [81] the Delft group realized the tunneling rate resolved readout (TRRO) for the first time. A two electron occupied lateral single dot in a parallel magnetic field of 0-6 T was used. At zero magnetic field a singlet–triplet relaxation time of 2.58 ms was measured. The method was demonstrated to be feasible even when the energy difference of the excited and ground states was bellow the experimental resolution (that is, it can be considered to be zero), giving a relaxation time of 310 μs. The measured relaxation rate was obtained by fitting the exponential decay of the excited state population as a function of the duration of the fill&wait step.

$$e(t) = \frac{3\Gamma_T}{3\Gamma_T + \Gamma_S} e^{-Wt}[1 - \alpha(t) - \beta(t)] + \alpha(t). \tag{3.9}$$

Here Γ_S and Γ_T are the tunneling rates to the singlet and triplet state and the

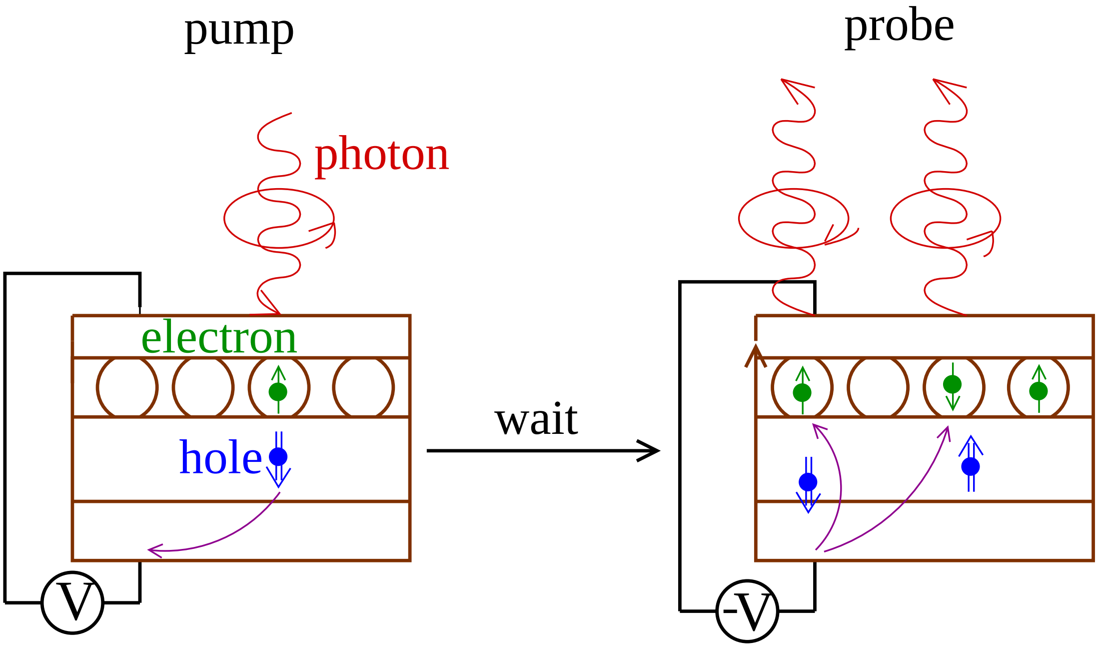

Figure 3.10: Optical pump and probe method. The spin is first pumped optically by a polarized light into an ensemble of self-assembled quantum dots. After a waiting time the remaining spin polarization is probed by measuring the polarization of the emitted light produced by the recombination.

prefactor reflects the filling efficiency – the triplet state is triple degenerate. The probabilities α and β reflect the possibility of a wrong measurement answer: α is a probability that a tunneling was observed even when the electron was in the ground state and β is the probability that the tunneling was not observed even when the electron was in the excited state. They originate in the fact that "unwanted" tunneling rates (such as out of the ground state during the probe step) are not exactly zero. The probabilities are computed in the Appendix .2 and were neglected in the previous computations, where they originated in thermal fluctuations or cotunnelings. In Ref. [81] the visibility (being the probability of the correct answer, equal to $1-\alpha-\beta$) of 80% was achieved, while in Ref. [51], 65% was estimated.

Optical detection of the spin relaxation

A completely different method should be mentioned here for the sake of chronology and as an example of optical methods used in spin relaxation measurements. In Ref. [107] the spin relaxation rate in an ensemble of self assembled quantum dots was measured by optical pump and probe method. The idea is depicted in Fig. 3.10. During the initialization (pump) the spin is optically pumped by a linearly polarized light which creates electron-hole pairs. The voltage is applied such that the holes are expelled from the area of confined electrons such that the recombination process is inhibited. After a waiting time the voltage is reversed, the holes are brought to the area of confined electrons and the recombination takes place. The emitted photon polarization, which depends on the spin orientation of the recombined electron, is detected. The exponential decay of the preferred polarization (being the polarization of the pump pulse) is observed. The longest spin relaxation time obtained was 20 ms at the temperature of 1 K. However, more importantly, the power law dependence of the spin relaxation rate on the perpendicular magnetic field (4-12 T) was observed with the exponent (five) in line with the theoretical prediction for the relaxation dominated by spin-orbit interaction. A typical excitation energy of a dot was 30 meV and approximately 10^4 dots were involved in the experiment.

Singlet–triplet double dot system

Perhaps a most remarkable system for studying coherent spin dynamics (and the relaxation as a subset) was introduced in Ref. [127]. A double dot occupied by two electrons with controllable asymmetry ϵ (detuning of the energy levels of the left and right single dots when considering them to be isolated) is used. The lowest part of the spectrum as a function of the asymmetry is in Fig. 3.11a. If the asymmetry is large, one of the dots is preferably occupied (the one lower in energy) and the ground state is a single dot singlet $S^{(0,2)}$. Since both electrons occupy one dot, the exchange energy is high and the single dot triplet states are far above the ground state and can be neglected. On the other hand, if the detuning is small the preferable occupation is one electron per dot. In this case the exchange energy is small and the ground state is four times degenerate, embracing one singlet $S^{(1,1)}$ and three triplet states $T_0^{(1,1)}$, $T_+^{(1,1)}$, and $T_-^{(1,1)}$. If the magnetic field is applied, the triplet states are split and a two level system, consisting of the singlet $S^{(1,1)}$ and triplet $T_0^{(1,1)}$, can be operated (initialized and probed) by projecting into/from the single dot singlet $S^{(0,2)}$ by adiabatically changing the detuning.

In the first experiment,[127] a charge on the dots was measured by QPC detector, while applying a three step pulse cycle depicted in Fig. 3.11b. If the order of the cycle sequence is A–B–C, the dot is emptied in point A (that is a single electron occupies the double dot). Then, in point B (small detuning), the second electron enters the dot. There is no relevant discrimination between the double dot singlet and triplet states (either by energy or the tunnel rates), so each of the four states is populated with the same probability. In the last part of the cycle the system is brought in point C (large detuning), where the electron being originally in the left dot should tunnel into the right dot to get the system into a ground state. This is possible only if the state in point B was the singlet, due to the spin conservation. For other states in B the transition is blocked for a certain time depending on the initial state, as shown in Fig. 3.11c. The double

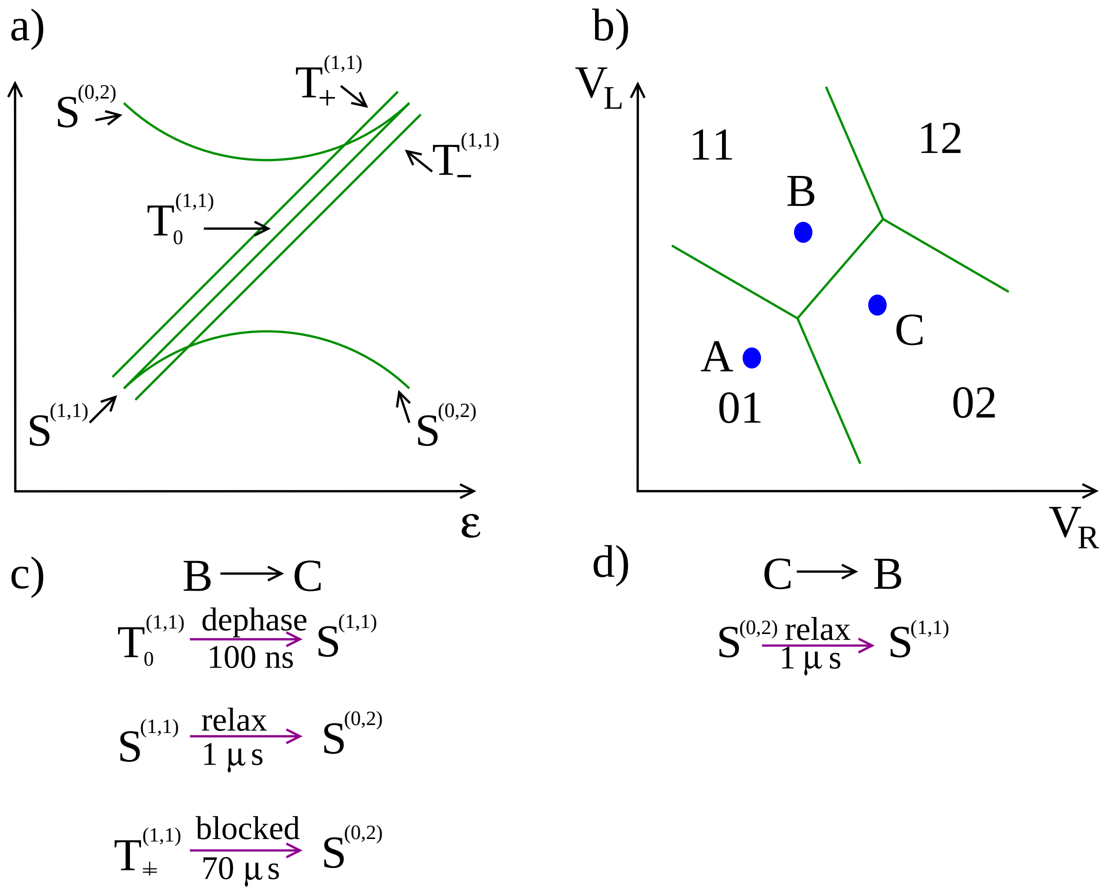

Figure 3.11: Two electron double dot system. Singlet (triplet) states are denoted by $S(T)$. The two upper indexes denote the occupation of the left and right dots. The lower index denotes a projection of the total spin along the magnetic field direction. a, Energy of the states as a function of the bias ϵ. b, Occupation of the two dots as a function of the voltages applied to the left (V_L) and right (V_R) dot. c, Possible processes to go from the double to single dot configuration and d, back.

dot triplet $T_0^{(1,1)}$ dephases into the double dot singlet on a timescale of $T_2 \sim 100$ ns (estimated from other experiments), following an orbital relaxation from the double dot to the single dot singlet, what happens on a scale of 1 μs (estimated from current measurements). For other double dot triplet states the transition is blocked until a spin flip transition occurs. By prolonging the duration of the pulse, the occupation of the left dot due to blocked transitions decays exponentially. By fitting this decay a singlet to triplet relaxation time of 70 μs was obtained. Note that no blocking is observed when the cycle is reversed, being A–C–B, since in C always a single dot singlet is loaded which is free to decay in B into a double dot singlet, see Fig. 3.11d.

While in the previously discussed experiment a magnetic field around 1 T was applied, in the next experiment[92] the same method was used at smaller magnetic fields (0-150 mT). The measured spin relaxation was in the range of 10 ms to 1 μs, while a clear suppression with increasing magnetic field was observed. Such a suppression indicates that the relaxation is caused by fluctuations of the magnetic field of nuclei spins, which are suppressed in an external magnetic field. From the measured relaxation times, an effective internal magnetic field due to nuclei magnetic moments was deduced to be $\sim$ 5 mT, which agrees with the theoretical prediction and supports the assumption about the nuclei spins being the dominant source of the relaxation.[117]

Measuring the decoherence in a quantum dot

We finish this chapter by describing two experiments probing the electron decoherence time. This is done most easily by optical pump and probe methods, similar to the previously discussed experiment of Ref. [107] on page 68. However, such experiments are done on ensembles of dots, so can give only the dephasing time T_2^*.[168]

Orbital decoherence

Experiment measuring the orbital decoherence in a double dot was presented in Ref. [83]. A double lateral quantum dot with $\sim$ 25 electrons connected to leads was used in a two step cycle. A magnetic field of 0.5 T was applied and the tunneling rates were such that the interdot tunneling was much smaller than the coupling of an individual dot to the corresponding lead, as is depicted in Fig. 3.12. The first step, when the dots are biased (that is, the detuning is finite), served as a measurement of the previously achieved state of the dot and a consequent initialization. The dot is kept in this step for a time long enough for an electron to tunnel out of the right dot, contributing to the current and another electron to tunnel into the left dot. The time is, however, short for the interdot tunneling, therefore if the electron was initially in the left dot it stays there. In the oscillation step the dots are unbiased and the eigenstates of the

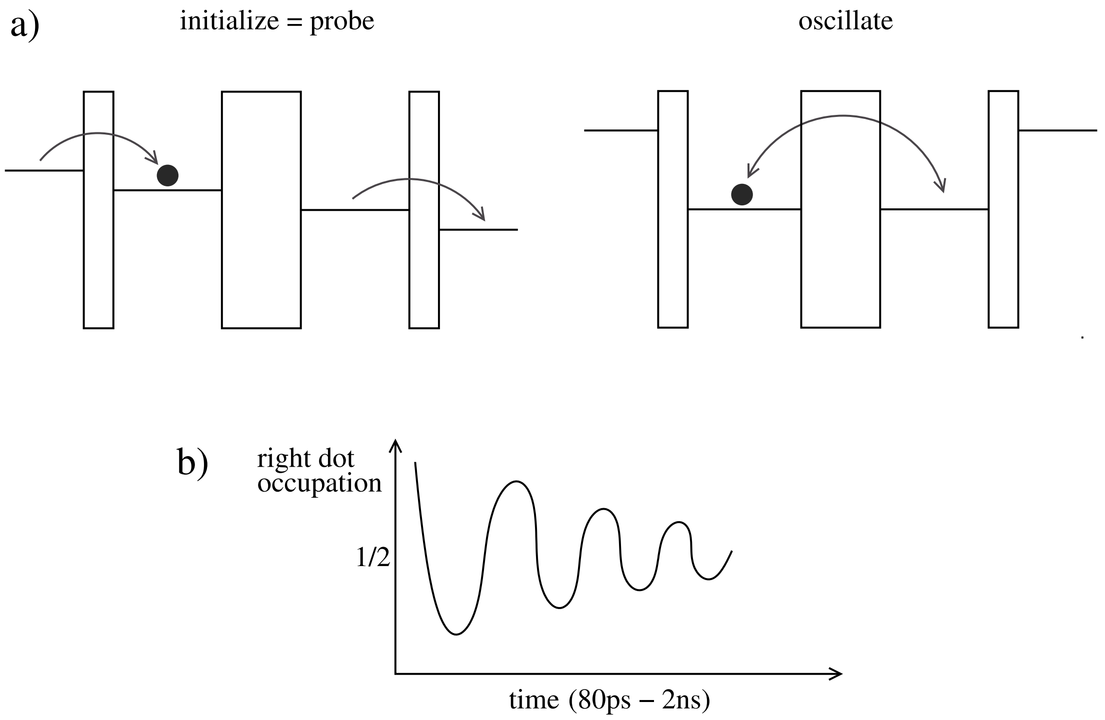

Figure 3.12: a, Two step pulse applied to a two level system of a double lateral quantum dot. b, The observed damped coherent oscillations.

system are delocalized states. The electron initially being in the left dot is then a superposition of delocalized eigenstates and will coherently precess between being in the left and right dot with frequency given by the energy difference of the two lowest delocalized states. The decay of these coherent oscillations is caused by the orbital decoherence and the decoherence time of 1 ns was obtained.

An impressive suitability of the singlet-triplet system in the double dot, Fig. 3.11, was manifested by measuring the spin decoherence time in Ref. [128]. As before, the state initialization/measurement was done by injecting from/projecting to the single dot singlet state at a large detuning, while the decoherence time was obtained from the system evolution at zero detuning, where the double dot singlet and triplet states are degenerate. This is analogous to the two steps used to measure the orbital decoherence described in the previous paragraph. The singlet and triplet states are coupled by magnetic field of the nuclei, which fluctuates over times larger than the relaxation/decoherence of the electron states. In first step the state is initialized to be the double dot singlet. After a waiting time the singlet occupation is measured. The dephasing causes the exponential decay of the probability to find the singlet from 1 at $t = 0$ to 0.5 at $t = \infty$. A dephasing time of 10 ns was extracted. To get a measurable signal, the probability has to be averaged over many cycles, on a total time scale larger than a typical time for fluctuations of the nuclear field. Thus the measured time is the spin dephas-

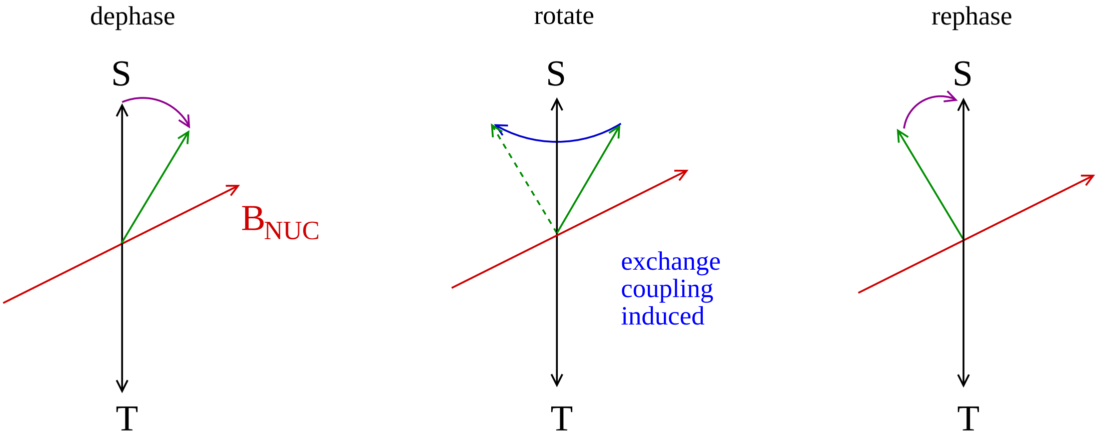

Figure 3.13: Rephasing a state in a spin echo experiment. See text for the explanation.

ing time T_2^*. The group succeeded in getting the decoherence time T_2, too, by applying a spin echo pulse. The idea of the spin echo is in Fig. 3.13. A Bloch sphere can represent the two level system, where the double dot singlet and triplet states are the north and south pole. The nuclear field coupling the two states is represented by a vector in the equatorial plane. The initial state being the north pole precesses around the nuclear field vector. The dephasing coming from multiple measurements comes around because the vector of the nuclear field changes its direction and size from one cycle to another. A spin echo means applying a coupling between the singlet and triplet states at the time τ such that the actual state rotates around the globe axis by 180°. After turning off the coupling, the state continues to precess around the vector of the nuclear field. However, due to the intermediate 180° rotation, at the time 2τ the state will come back to the initial position at the north pole. In this way the influence of a constant nuclear field on the state can be excluded in each cycle. A decoherence time of ~ 1 μs was obtained, being two order of magnitude larger than the dephasing time.

3.3 Phonon induced spin relaxation due to the admixture mechanism

In the rest of this chapter, we present a systematic and comprehensive investigation of phonon-induced orbital and spin relaxation in lateral single and double quantum dots, defined in a GaAs heterostructure. We consider the most relevant electron-phonon couplings – the deformation potential and piezoelectric acoustic phonons. We numerically calculate the relaxation rates in the presence of in-plane and perpendicular magnetic fields. We report on new anisotropy effects of spin relaxation in double dots. The anisotropy arises due to anisotropic spin hot

method	year	system	relax. time
STM	1989	single spin	spin detection
fluorescence	1997	single spin	spin detection
in N-V defects	2002		T_1 ∼ms-s
	2004		T_2 ∼1 μs
magnetic resonant	2004	single spin	spin detection
force microscopy			T_1=760 ms
energy resolved	2001	lateral SD, 50 e	T_1^{orbital}=3 ns
readout (ERO)	2002	lateral SD, 50 e	$T_1 > 2$ μs
	2002	vertical SD, 2 e	$T_1^{\mathrm{S-T}} \geq 100$ μs
	2005	lateral SD, 8 e	$T_1^{\mathrm{S-T}}$=200 μs
ERO+QPC	2003	lateral SD, 1 e	T_1 >50 μs
(B≥ 8 T)	2004	lateral SD, 1 e	$T_1 = 0.85$ ms
(B≥ 1.7 T)	2006	lateral SD, 1 e	$T_1 = 150$ ms
tunneling resolved	2005	lateral SD, 2 e	$T_1^{\mathrm{S-T}}$=2.5 ms
readout (TRRO)			
optical pump&probe	2004	10^4 dots	T_1=20 ms
		self assembled	
singlet-triplet	2005	lateral DD, 2 e	$T_1^{\mathrm{S-T}}$=μs-10 ms
SD-DD system			
	2005		$T_2^{\mathrm{S-T}} = 1$ μs

Table 3.1: Measuring the relaxation time of the spin of a single confined electron – a road map. STM=scanning tunneling microscope, N-V defect=nitrogen vacancy defect, ERO=energy resolved readout, TRRO=tunneling rate resolved readout, QPC=quantum point contact, SD=single dot, DD=double dot, S-T=singlet-triplet, T_1= relaxation time, T_2=decoherence time.

spots, the parameter (magnetic field and interdot coupling) regions in which a spectral crossing between a spin up and a spin down state is lifted (producing an anti-crossing) by spin-orbit coupling [60, 61]. At these points the spin and orbital relaxation rates are equal. In single quantum dots spin hot spots were found in Ref. [21], while in vertical few-electron quantum dots in Ref. [12]. In lateral double dots spin hot spots appear at useful magnetic fields (1 T) and interdot couplings (0.1 meV), due to the crossing of the lowest orbital antisymmetric (with respect to the quantum dot axis) state and the Zeeman split symmetric state of the opposite spin. This occurs when the tunneling energy equals the Zeeman energy. Manipulation of interdot coupling in the presence of a magnetic field thus in general results in a short spin lifetime. Fortunately, we have found that the spin hot spots are absent for certain arrangements of the double dots' axis and the orientation of the in-plane magnetic field. In particular, if the dots are oriented along a diagonal [on a (001) heterostructure plane], and the magnetic field is perpendicular, the spin hot spots are absent (due to symmetry reasons) for any values of spin-orbit parameters. We propose such a geometry, which corresponds to what we call "easy passage", for quantum information processing.

In addition to discussing the easy passages, we focus on providing a unified description, both analytical and numerical, of orbital and spin relaxation rates. We give analytical formulas describing the trends, with respect to magnetic fields and confinement energies of the dots, of the rates. We present the numerically calculated orbital relaxation rates and demonstrate that they are due to the deformation potential phonons at low magnetic fields and due to piezoelectric phonons at high fields (at zero magnetic field, the orbital relaxation in a biased double dot was studied in Ref. [145], using a two-level model).

As for the spin relaxation, we demonstrate here the different origin of spin hot spots in single and double quantum dots. While in single dots spin hot spots appear due to the Bychkov-Rashba term,[21] in double dots both the Bychkov-Rashba and Dresselhaus terms contribute. The reasons is the different symmetry of the underlying states in single and double dots. Furthermore, we classify here the conditions for the absence (or narrowing) of spin hot spots in double dots defined in quantum wells grown in different crystallographic directions, in which the Dresselhaus spin-orbit interaction takes on different functional forms. We also explore the orbital effects of a perpendicular magnetic field component – the main effect is the absence of easy passages; only a narrow "weak passages" appear instead with inhibited but finite spin hot spots. Finally, we show that easy passages are also absent in general asymmetric double dots, implying stringent symmetry requirements on coupled dots for spin information processing.

In the next sections, we first derive useful expressions for orbital and spin relaxation rates. Then we describe the orbital and spin relaxation in single dots for the case of in-plane and perpendicular magnetic fields, followed by a similar description for double dots. Finally we give conclusions.

3.4 Model

3.4.1 Electron parameters

We study a single electron double dot, as described in Chapter 2, while using slightly different values for the spin-orbit couplings. To agree with experimental data, we choose for $\tilde{\alpha}_{BR}$ a value of 3.3 meVÅ, which is in line of experimental observations[119, 100] and corresponds to the carrier density of 5×10^{11} cm^{-2} in Ref. [93]. For the coupling of the linear Dresselhaus terms we choose $\gamma_c\langle P_z^2\rangle/\hbar^2 = 4.5$ meVÅ, corresponding to the 11 nm thick ground state of the triangular confining potential.[34] These values correspond to length units of $l_{BR} = 1.8$ μm, and $l_D = 1.3$ μm.

For a confinement length of 32 nm (used in a recent experiment [51]) and a perpendicular magnetic field of 1 T, one gets the following typical magnitudes for the strengths of the contributions to the Hamiltonian (2.2): 1.1 meV for the confinement energy E_0, 13 μeV for the Zeeman splitting, and 14, 10, and 0.8 μeV for the linear Dresselhaus, Bychkov-Rashba, and the cubic Dresselhaus terms, respectively. The spin-orbit interactions are small perturbations, with strengths comparable to the Zeeman splitting. This leads to the many orders of magnitude difference between the orbital and spin relaxation rates.

We numerically obtain eigenstates of the full electron Hamiltonian, Eq. (2.2), and compute the orbital and spin relaxation rates using Fermi's Golden Rule. We also present analytical calculations for various limiting cases, where we use the effective spin-orbit Hamiltonian derived in Sec. 2.6.1 and perturbative expressions for the lowest eigenfunctions from Sec. 2.6.2.

3.4.2 Phonon-induced orbital and spin relaxation rates

By orbital relaxation we mean the transition from the first excited orbital state to all lower lying states. By spin relaxation we mean the transition from the upper Zeeman split orbital ground state to all lower lying states (except at high magnetic fields, there is only one lower Zeeman split orbital ground state). The spin of a state Γ [eigenstate of H_0, Eq. (2.2)] is quantized in the direction of the magnetic field. However, due to the spin orbit interactions, the perturbed states $\overline{\Gamma}$ [eigenstates of H', Eq. (2.44)] have no common spin quantization axes. We call a state to be spin up (down) if the mean value of the spin in the direction of the magnetic field is positive (negative). Since the spin-orbit interactions are a small perturbation, these mean values are close to $\pm\hbar/2$, except at anti-crossings.

Given the initial and final states for the transition we compute the rates by Fermi's Golden rule, where the perturbation is the electron-phonon interaction. The relevant terms for our GaAs system comprise deformation (df) and piezoelectric acoustic (pz) phonons, described by Hamiltonian terms [114]

$$H^{\mathrm{df}} = \sigma_e \sum_{\mathbf{K}} \sqrt{\frac{\hbar K}{2\rho V c_l}} (b_{\mathbf{K},l} + b^{\dagger}_{-\mathbf{K},l}) e^{\mathrm{i}\mathbf{K}.\mathbf{R}}, \tag{3.10}$$

$$H^{\mathrm{pz}} = -\mathrm{i}eh_{14} \sum_{\mathbf{K},\lambda} \sqrt{\frac{\hbar}{2\rho V c_\lambda}} M_\lambda (b_{\mathbf{K},\lambda} + b^{\dagger}_{-\mathbf{K},\lambda}) e^{\mathrm{i}\mathbf{K}.\mathbf{R}}. \tag{3.11}$$

Here the three dimensional phonon wave vector is denoted by $\mathbf{K} = (k_x, k_y, k_z) = (\mathbf{k}, k_z)$, and $\lambda = l, t1$, or $t2$ is the phonon polarization (one longitudinal and two transversal); ρ is the material density (5.3×10^3kg m^{-3}, for GaAs), V is the volume of the crystal, c_λ is the sound velocity, ($c_l = 5.3 \times 10^3$ m/s, $c_t = 2.5 \times 10^3$ m/s), $b^{\dagger}_{\mathbf{K},\lambda}, b_{\mathbf{K},\lambda}$ are the creation and annihilation phonon operators, σ_e is the deformation potential (7.0 eV), and eh_{14} is the piezoelectric constant (1.4×10^9 eV/m). Finally, the geometrical factors M_λ are equal to $2(k_x k_y e^\lambda_z + k_z k_x e^\lambda_y + k_y k_z e^\lambda_x)/K^2$, where $\mathbf{e}^\lambda$ are unit polarization vectors,

$$\begin{aligned} \mathbf{e}^l &= (k_x, k_y, k_z)/K, \\ \mathbf{e}^{t1} &= (-k_y, k_x, 0)/k, \\ \mathbf{e}^{t2} &= (k_x k_z, k_y k_z, -k^2)/K. \end{aligned} \tag{3.12}$$

Consider first the deformation potential, Eq. 3.10, in which only longitudinal ($\lambda = l$) phonons take part. Using Fermi's Golden rule, a relaxation (orbital or spin) rate can be written as

$$\Gamma^{\mathrm{df}} = [n(E)+1]\gamma_{\mathrm{df}} E^2 \int \mathrm{d}^2\mathbf{k} |F(\mathbf{k})|^2 |f(k^l_z)|^2 / k^l_z \tag{3.13}$$

$$= [n(E)+1]\gamma_{\mathrm{df}} E^2 l_B^{-1} \chi_{\mathrm{df}}(\mathcal{E}_l). \tag{3.14}$$

Here E is the energy difference between the initial and final states, $n(E) = [\exp(E/k_B T) - 1]^{-1}$ is the occupation number of the phonon state with energy E at temperature T (further we use zero temperature), $\gamma_{\mathrm{df}} = \sigma_e^2/8\pi^2\rho c_l^4 \hbar^3$ is the strength of the deformation electron-phonon interaction [8.3×10^{10} s^{-1} nm /(meV)^2], $F(\mathbf{k}) = \int \mathrm{d}^2\mathbf{r}\, \overline{\Gamma}^{\dagger}_i e^{i\mathbf{k}.\mathbf{r}} \overline{\Gamma}_f$ is the xy-overlap, and $f(k_z) = \int \mathrm{d}z\, \phi_0(z)^{\dagger} e^{ik_z z} \phi_0(z)$ is the z-overlap, contribution of which can be neglected, $f(k_z) \approx 1$, if the energy difference E is much smaller than the excitation energy in the z confinement potential. The z component of the wave vector is given by $k^\lambda_z = \sqrt{\mathcal{E}^2_\lambda / l_B^2 - k^2}$, where the dimensionless parameter $\mathcal{E}_\lambda = E l_B / \hbar c_\lambda$ is the ratio of the effective length l_B and the wavelength of the emitted phonon. Finally, $\chi_{\mathrm{df}}(\mathcal{E}_l)$ is an integral of the xy-overlap $F(\mathbf{k})$. Since a typical linear dimension of a wavefunction is the effective length l_B, we express it as

$$\chi_{\mathrm{df}}(\mathcal{E}_l) = \int_{k_z \geq 0} \mathrm{d}^2(\mathbf{k} l_B) \frac{|F(\mathbf{k})|^2}{\sqrt{\mathcal{E}_l^2 - k^2 l_B^2}}. \tag{3.15}$$

	$\mathcal{E}_\lambda \gg 1$	$\mathcal{E}_\lambda \ll 1$
$\Gamma^{\rm df}$	$A^2\gamma_{\rm df}l_B^{-1}E^2\mathcal{E}_l^{-1}$	$A^2\gamma_{\rm df}l_B^{-1}E^2\mathcal{E}_l^{3}$
$\Gamma_l^{\rm pz}$	$A^2\gamma_{\rm pz}l_B^{-1}\mathcal{E}_l^{-5}$	$A^2\gamma_{\rm pz}l_B^{-1}\mathcal{E}_l^{3}$
$\Gamma_t^{\rm pz}$	$A^2\gamma_{\rm pz}(c_l/c_t)^2l_B^{-1}\mathcal{E}_t^{-3}$	$A^2\gamma_{\rm pz}(c_l/c_t)^2l_B^{-1}\mathcal{E}_t^{3}$
relative	$\Gamma^{\rm df} \gg \Gamma_t^{\rm pz} \gg \Gamma_l^{\rm pz}$	$\Gamma_t^{\rm pz} \approx (c_l/c_t)^5\Gamma_l^{\rm pz} \gg \Gamma^{\rm df}$

Table 3.2: The relaxation rates and the relative strength of the contributions due to deformation ($\lambda = l$), piezoelectric longitudinal ($\lambda = l$), and piezoelectric transversal ($\lambda = t$) phonons. The two limiting cases are defined by the ratio, $\mathcal{E}_\lambda$, of the wavelength of the emitted phonon of polarization λ, and the effective length l_B. The initial and final states are encoded into the coefficient A, which needs to be evaluated for specific cases.

We compute the relaxation rate $\Gamma^{\rm df}$ numerically using formula (3.13). However, we can gain physical insight in two important limits. First, if the wavelength of relevant phonons is smaller than the size of the dots, $\mathcal{E}_l \gg 1$, the square root can be taken out from the integral and $\chi_{df} \sim 1/\mathcal{E}_l$. Physically, this means that the energy to be absorbed by the phonon is large and almost whole is in the z component of the phonon wave vector (phonon is emitted almost perpendicularly to the xy-plane). Second, in the opposite limit of $\mathcal{E}_l \ll 1$, the integration is only in the vicinity of point $\mathbf{k} = 0$. Because of the orthogonality of the eigenfunctions the overlap integral vanishes, $F(\mathbf{k} \to \mathbf{0}) \to 0$, and the lowest order gives $|F|^2 \sim (kl_B)^2$. This leads to the dependence of $\chi_{\rm df}(\mathcal{E}_l) \sim \mathcal{E}_l^3$.

Analogous expression holds for the piezoelectric interaction which contains contributions from longitudinal and transverse phonons. The relaxation rate can be written as

$$\Gamma^{\rm pz} = [n(E) + 1]\gamma_{\rm pz}l_B^{-1}\chi_{pz}(\mathcal{E}), \tag{3.16}$$

with $\gamma_{\rm pz} = (eh_{14})^2/8\pi^2\rho c_l^2\hbar = 4 \times 10^{10}$ s^{-1} nm (note the different unit from $\gamma_{\rm df}$) and $\chi_{\rm pz}(\mathcal{E}) = \sum_\lambda (c_l^2/c_\lambda^2) \int {\rm d}^2(\mathbf{k}l_B)|M_\lambda|^2|F(\mathbf{k})|^2/k_z^\lambda l_B$. The geometrical factors, M_λ, have no influence on the limiting expressions for $\chi_{\rm pz}$ in the limit $\mathcal{E} \ll 1$, where $\chi_{\rm pz}(\mathcal{E}) \sim \mathcal{E}^3$. If $\mathcal{E} \gg 1$, the fact that M_λ contains factors $(k_x/K)^2$ and k_x/K leads to limits $\mathcal{E}^{-5}$ and $\mathcal{E}^{-3}$ for the longitudinal and transverse phonons, respectively. Table 3.2 summarizes the limiting expressions.

As we discussed in Sec. 3.1.1, in addition to the deformation and piezoelectric phonons, there are additional electron-phonon spin dependent interactions which can lead to spin relaxation. The direct spin-phonon coupling (spin-orbit modulated electron-phonon interaction[97, 98]) is believed to give a negligible contribution. In very small (say, 10-20 nm, which is not our case) quantum dots spin relaxation due to the ripple mechanism[164] can be as important as the spin-orbit mechanism and should be considered. Finally, at low magnetic fields the relaxation is believed to be dominated by the hyperfine interaction between the electron and nuclei of the host material.[59, 58]

3.5 Single dots

In the single dot case we identify the unperturbed lower and upper Zeeman split orbital ground, and excited orbital states as $\Psi_{0,0,\uparrow}$, $\Psi_{0,0,\downarrow}$, and $\Psi_{0,-1,\uparrow}$, respectively (we call them ground, spin, and orbital state). Here, consistent with Chapter 2, we use letter Ψ for the eigenfunctions of the single dot. The negative value of the g factor energetically favors spin up rather that spin down states. Having opposite spin, the perturbed ground and spin states will have a nonzero overlap due to those perturbations in the effective Hamiltonian (2.45) which do not commute with the Zeeman term. Therefore the xy-overlap $F(\mathbf{k})$ will be proportional to the strengths of the corresponding perturbations. In the case of the spin relaxation, the coefficient A in Tab. 3.2 will be approximately equal to these strengths divided by a typical energy difference between the corresponding coupled states, as can be seen from Eqs. (2.54)-(2.57). On the other hand, since the excited orbital and ground states have the same spin, the coefficient A for the orbital relaxation is of order 1.

This consideration leads to the following approximations which we use when estimating the rate analytically. For orbital relaxation

$$H_1 \approx 0. \tag{3.17}$$

For spin relaxation, in analytical calculations we neglect the cubic Dresselhaus term. If the magnetic field is in-plane, the term in Eq. (2.46) does not couple the ground or the spin state, which have zero orbital momenta, with any other state. If the magnetic field is perpendicular, the term in Eq. (2.46) commutes with the Zeeman term, again giving no contribution to the spin relaxation. For the spin relaxation we therefore approximate

$$H_1 \approx H_Z^{(2)}. \tag{3.18}$$

3.5.1 In-plane magnetic field

Figure 3.14 compares our calculation of the spin relaxation in an in-plane magnetic field with two experiments.[51, 6] It can be seen that the experiments can be fitted very well over large range of magnetic fields with a reasonable set of spin-orbit parameters. This is a strong indication that acoustic phonons together with the admixture mechanism due to spin-orbit is the dominant source of the spin relaxation.

To understand numerical results, we provide approximate analytical formulas. Using Eqs. (2.54), (2.55), (3.16), and (3.18) we get for the dominant contribution to the spin relaxation due to piezoelectric transversal phonons in the low magnetic field limit

$$\Gamma_t^{\mathrm{pz}} \approx \frac{256\pi\gamma_{\mathrm{pz}} c_l^2 m^2}{105\hbar^7 c_t^5} l_0^8 |\mu B_{\|}|^5 \mathcal{L}_{\mathrm{SO}}^{-2}, \tag{3.19}$$

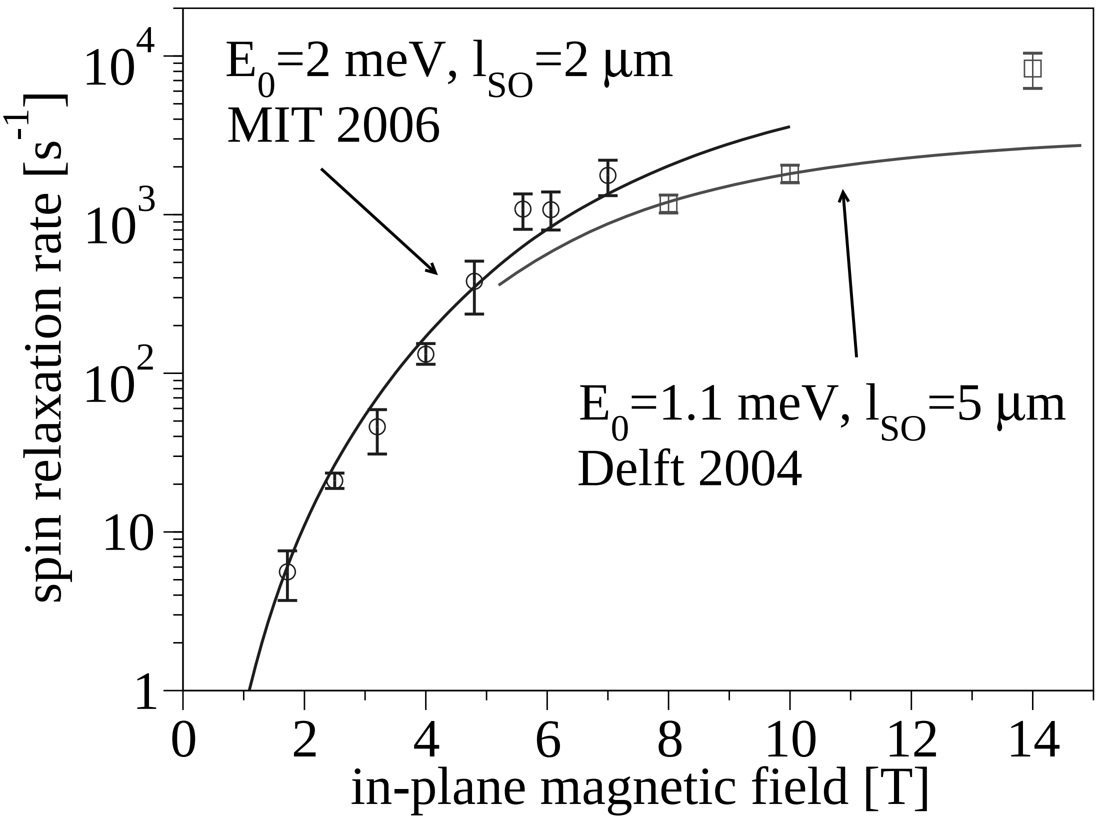

Figure 3.14: Spin relaxation rate in single electron single dot as a function of in-plane magnetic field in two experiments. Points with error bars are experimental values, solid lines are our fits. The only fitting parameter is the strength of the spin-orbit coupling, different in the two experiments.

where

$$\mathcal{L}_{\mathrm{SO}}^{-2} = \frac{l_D^2 + l_{BR}^2 - 2\sin(2\gamma) l_D l_{BR}}{l_D^2 l_{BR}^2} \tag{3.20}$$

describes the effective (anisotropic) spin-orbit length. The angular dependence of the spin relaxation rate, expressing the C_{2v} symmetry of the heterostructure, allows to find the ratio of the Dresselhaus and Bychkov-Rashba couplings:

$$\min\{l_D/l_{BR}, l_{BR}/l_D\} = 2/(\sqrt{r_a}+1) - 1, \tag{3.21}$$

where r_a is the ratio of the rates at $\gamma = 45°$ and $\gamma = 135°$. A possible measured angular dependence with the minimum at $\gamma = 45°$ would be another convincing indication that the admixture due to spin-orbit is the mechanism of the relaxation. A more general angular dependence, allowing for out-of-plane magnetic fields, was derived in Ref. [75].

The reason for the angular dependence of Γ_t^{pz} follows from Eq. (3.18), which for an in-plane field is

$$H_1 = -\mu B_{\|} \sigma_z [x(\frac{\cos\gamma}{l_{BR}} - \frac{\sin\gamma}{l_D}) + y(\frac{\sin\gamma}{l_{BR}} - \frac{\cos\gamma}{l_D})]. \tag{3.22}$$

Due to the selection rules for the Fock-Darwin states, x and y do not mix in coupling of the states. The coefficient A^2 is then proportional to the sum of the squared couplings from Eq. (3.22), at x and y. Taking E_0 as a typical energy difference E of the coupled states and using l_B for a natural length unit, we get $A^2 \approx |\mu B_{\|} l_B / E_0|^2 \mathcal{L}_{\mathrm{SO}}^{-2}$. Noting that $l_B = l_0$ for in-plane field and using the low energy limit for Γ_t^{pz} from Tab. 3.2, one recovers Eq. (3.19) up to a numerical factor.

3.5.2 Perpendicular magnetic field

Orbital relaxation rates

In the case of a perpendicular magnetic field, the numerically calculated orbital and spin relaxation rates in a single dot are shown in Fig. 3.15. The orbital relaxation rate is of the order of 10^9 s^{-1}. The spin-orbit contributions to the rate (not shown in the figure) are of the order of 10^6 s^{-1} for the linear spin orbit terms and 10^5 s^{-1} for the cubic Dresselhaus term, validating the approximation Eq. (3.17). The energy difference of the orbital and the ground state is $E = \hbar^2/ml_B^2 - (\hbar e/2m)B_\perp$. At *low* magnetic fields the *high* $\mathcal{E}$ limit applies and the deformation potential dominates the orbital relaxation rate. The results are listed in Tab. 3.3. The values at zero magnetic field, up to a numerical factor, follow from Tab. 3.2, if one uses $A = 1$ and the low magnetic field limits, where $E \approx \hbar^2/ml_0^2$, and $l_B \approx l_0$. The dependence of the rates on the energy difference of the states, shown in Tab. 3.2, is enough to understand the different dependence of

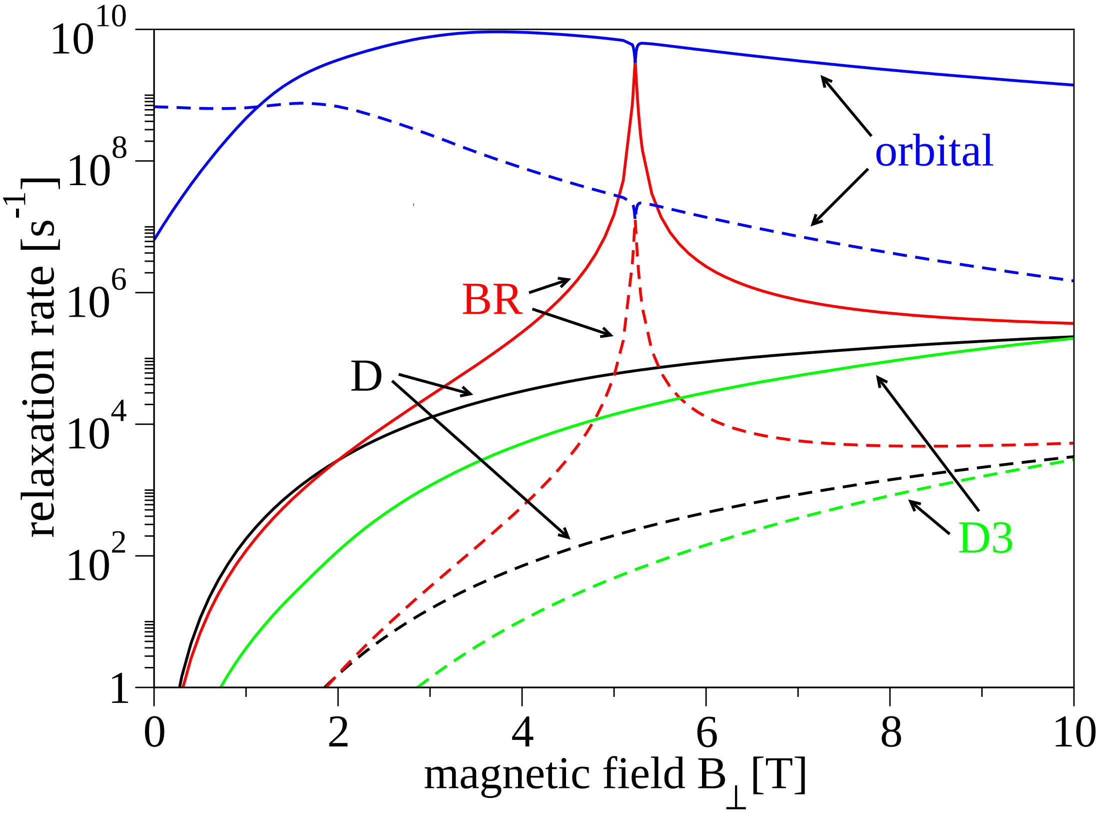

Figure 3.15: Orbital and spin (labels D, BR, and $D3$ denote which spin-orbit interaction is present) relaxation rates in a single quantum dot, for the piezoelectric (solid) and deformation potential (dashed) phonons. The confining length is 32 nm. Anti-crossing of the unperturbed spin and orbital state occurs at $B_{\perp} = 5.2$ T.

low mag. field	orbital	Γ^{df}	$(\pi\gamma_{\mathrm{df}}\hbar^3 c_l/m)l_0^{-4}(1-B_\perp e l_0^2/2\hbar)$	$\lesssim 0.6$ T
		Γ_l^{pz}	$(459\pi\gamma_{\mathrm{pz}}c_l^5 m^5/4\hbar^5)l_0^4(1+5B_\perp e l_0^2/2\hbar)$	$\lesssim 0.5$ T
		Γ_t^{pz}	$(61\pi\gamma_{\mathrm{pz}}c_l^2 c_t m^3/4\hbar^3)l_0^2(1+3B_\perp e l_0^2/2\hbar)$	$\lesssim 0.8$ T
	spin	Γ^{df}	$(128\pi\gamma_{\mathrm{df}}m^2/3\hbar^7 c_l^3)l_0^8\lvert\mu B_\perp\rvert^7 l_D^{-2}$	$\lesssim 4$ T
		Γ_l^{pz}	$(128\pi\gamma_{\mathrm{pz}}m^2/35\hbar^7 c_l^3)l_0^8\lvert\mu B_\perp\rvert^5 l_D^{-2}$	$\lesssim 4$ T
		Γ_t^{pz}	$\Gamma_l^{\mathrm{pz}} \times 4c_l^5/3c_t^5$	$\lesssim 4$ T
high mag. field	orbital	Γ^{df}	$(2\pi\gamma_{\mathrm{df}}\hbar^{13}/3e^6 m^5 c_l^3)l_0^{-20}B_\perp^{-6}$	$\gtrsim 4$ T
		Γ_l^{pz}	$(8\pi\gamma_{\mathrm{pz}}\hbar^7/35e^4 m^3 c_l^3)l_0^{-12}B_\perp^{-4}$	$\gtrsim 4$ T
		Γ_t^{pz}	$\Gamma_l^{\mathrm{pz}} \times 4c_l^5/3c_t^5$	$\gtrsim 6$ T
	spin	Γ^{df}	$(32\pi\gamma_{\mathrm{df}}\lvert\mu\rvert^5/3\hbar e^2 c_l^3)B_\perp^3 l_D^{-2}$	$\gtrsim 8$ T
		Γ_l^{pz}	$(32\pi\gamma_{\mathrm{pz}}\lvert\mu\rvert^3/35\hbar e^2 c_l^3)B_\perp l_D^{-2}$	$\gtrsim 7$ T
		Γ_t^{pz}	$\Gamma_l^{\mathrm{pz}} \times 4c_l^5/3c_t^5$	$\gtrsim 7$ T

Table 3.3: Approximate orbital and spin (due to Dresselhaus coupling) relaxation rates in a single quantum dot at low and high perpendicular magnetic fields in the lowest order of the non-degenerate perturbation theory. In the last column we state the maximal or minimal magnetic field by requiring that at $l_0 = 32$ nm the presented approximation does not differ from the numerical value by more than a factor of 2.

the deformation and piezoelectric contributions to the orbital relaxation rate at low magnetic fields shown in Figs. 3.15 and 3.16. The deformation contribution drops with increasing both the magnetic field and confinement lengths, while the piezoelectric contribution increases with increase of these two parameters.

For fields lower that 1 T the dominant deformation contribution manifest itself on Fig. 3.16. At magnetic fields higher than 1 T the piezoelectric contribution dominates. Up to about 4 T we are still in the regime $\mathcal{E} \gg 1$ and the rate grows with increasing magnetic field and increasing confinement length. Since the energy difference E drops with increasing magnetic field, for magnetic fields $\gtrsim 6$ T we get into the limit $\mathcal{E} \ll 1$. The corresponding orbital relaxation rates in 3.3 then follows from Tab. 3.2 using $A = 1$ and high magnetic field limits, where $E \approx \hbar^3/emBl_0^4$ and $l_B^2 \approx 2\hbar/eB$. This leads to a much stronger drop of the deformation contribution to the rate with the increase of both magnetic field and the confinement length, than is the drop of the piezoelectric contribution.

Finally, we explain the influence of the anti-crossing on the orbital relaxation rate, seen in Fig. 3.15. The anti-crossing contributes by an overall factor of $|\alpha|^2$ [α is defined in Eq. (2.59)], which multiplies the orbital relaxation rates listed in Tab. 3.3. Away from anti-crossing $\alpha \approx 1$, while directly at the anti-crossing the rate is reduced by a factor of 2, $\alpha = 1/\sqrt{2}$. The anti-crossing region for the orbital relaxation is rather narrow (~ 0.1 T) and manifests itself as a narrow line of the suppression of the rate in Fig. 3.16.

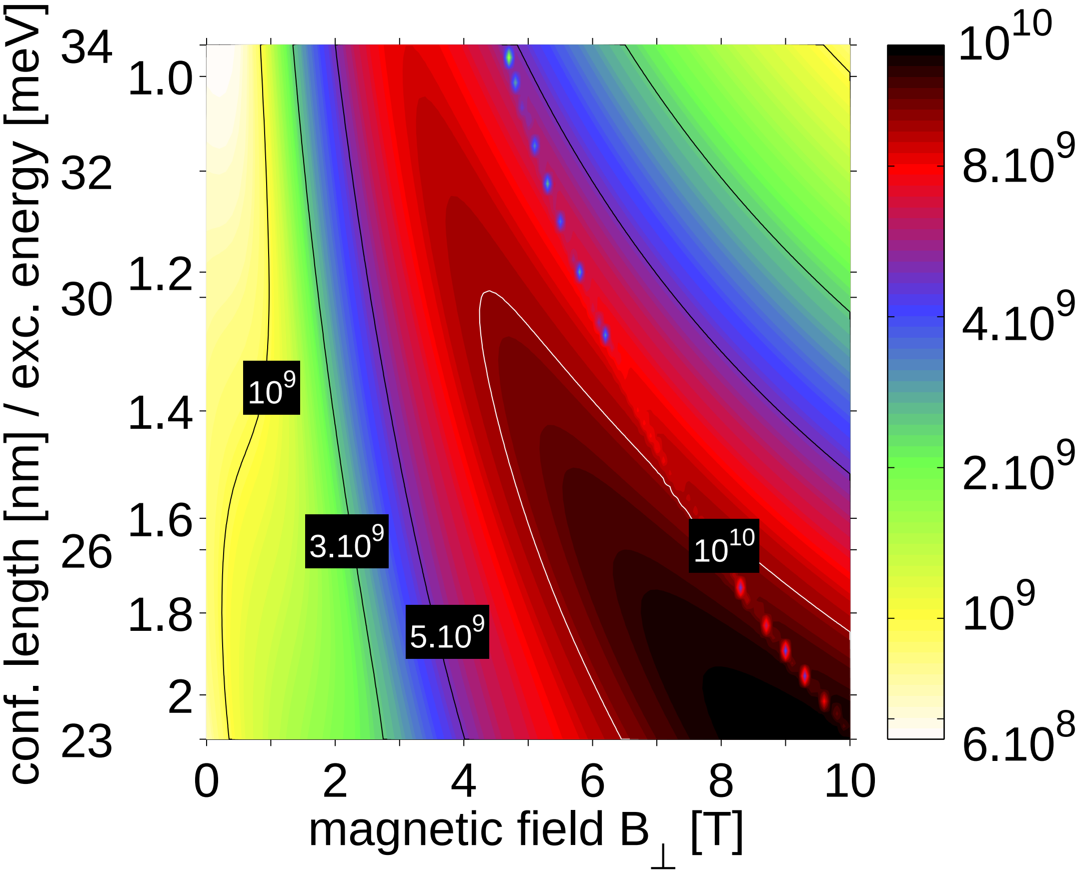

Figure 3.16: Orbital relaxation rate (the sum of the deformation and piezoelectric contribution) in a single quantum dot as a function of magnetic field and the confinement length l_0 / the confinement (excitation) energy E_0. The rate is given on the logarithmic scale in the units of s^{-1}. The solid lines represent equal relaxation rates (equirelaxation lines) with values shown by the labels. The granular structure in the figure is an artifact of the limited data resolution.

Spin relaxation rates

For spin relaxation the relevant energy difference is the Zeeman splitting, $E \approx 2|\mu B|$. Therefore the low energy limit, $\mathcal{E} \ll 1$, applies up to rather high magnetic fields ($\sim$10 T). Piezoelectric transversal phonons dominate the rate. The linear spin-orbit terms dominate over the cubic Dresselhaus term, although the difference becomes smaller for higher magnetic fields. We use an example of the linear Dresselhaus term for analytical expressions. Using Eq. (3.18) and the limits of low and high magnetic fields we present the analytical spin relaxation rates in Tab. 3.3 (these results were also derived in Refs. [21] and [98]). These formulas approximately follow from Tab. 3.2 using $A = |\mu B_\perp| l_B / l_D \delta E$ and $E = |\mu B_\perp|$, while noting that $\delta E = E_0$ for low and $\delta E = |\mu B_\perp|$ for high magnetic fields. The trends described by the Dresselhaus contribution can be seen in Fig. 3.15. The spin relaxation rate grows much steeper with increasing magnetic field at low $B_\perp$ (fifth power) than at high $B_\perp$ (first power). Interestingly, at high magnetic fields the rate does not depend on the confining length.

Away from the anti-crossing analogous formulas, up to a numerical factor, as those listed in Tab. 3.3, hold for the contribution to the spin relaxation due to the Bychkov-Rashba term after the substitution $l_D \to l_{BR}$. In this case the contribution to the overlap between the spin and ground states due to the term β in Eq. (2.55) is comparable to others. However, comparing the analytical formulas from Tab. 3.3 with the numerical calculation in Fig. 3.17, we find discrepancy, except at low magnetic fields. This is because, as can be seen also in Fig. 3.15, the rate is actually dominated by a spin hot spot (anti-crossing). The anti-crossing occurs for single dots only when the Bychkov-Rashba term is present, since the Dresselhaus terms do not couple the unperturbed orbital states.[21] In this case we can neglect all terms but that one containing β in Eq. (2.55) and for the spin relaxation rate due to the anti-crossing one gets $\Gamma(\mathrm{spin},\mathrm{acr}) = |\beta|^2 \Gamma(\mathrm{orbital})$. Thus, the anti-crossing effectively mixes what we usually call spin and orbital rates. The spin relaxation rate has a sharp peak at the anti-crossing. With increasing the "distance" from the anti-crossing the rate drops, mirroring the drop of the coefficient $|\beta|^2$. Only far enough from the anti-crossing the term β is not dominant in Eq. (2.55) and the rate is described by expressions analogous to those from Tab. 3.3. In Fig. 3.15 the Bychkov-Rashba contribution to the spin relaxation rate is dominated by the β term unless the magnetic field is smaller than 2 T. Similarly in Fig. 3.16, for fields higher than 2 T the total spin relaxation rate is dominated by the anti-crossing contribution due to Bychkov-Rashba term. Consequently, the influence of the anti-crossing is substantial in a much larger region (several Tesla) than in the case of the orbital relaxation.

In Ref. [21] spin relaxation rates due to the deformation potential were computed in the lowest order of the perturbation theory and an analogous figure to our Fig. 3.15 was presented. Our results for both orbital and spin relaxation rates are in a quantitative agreement.

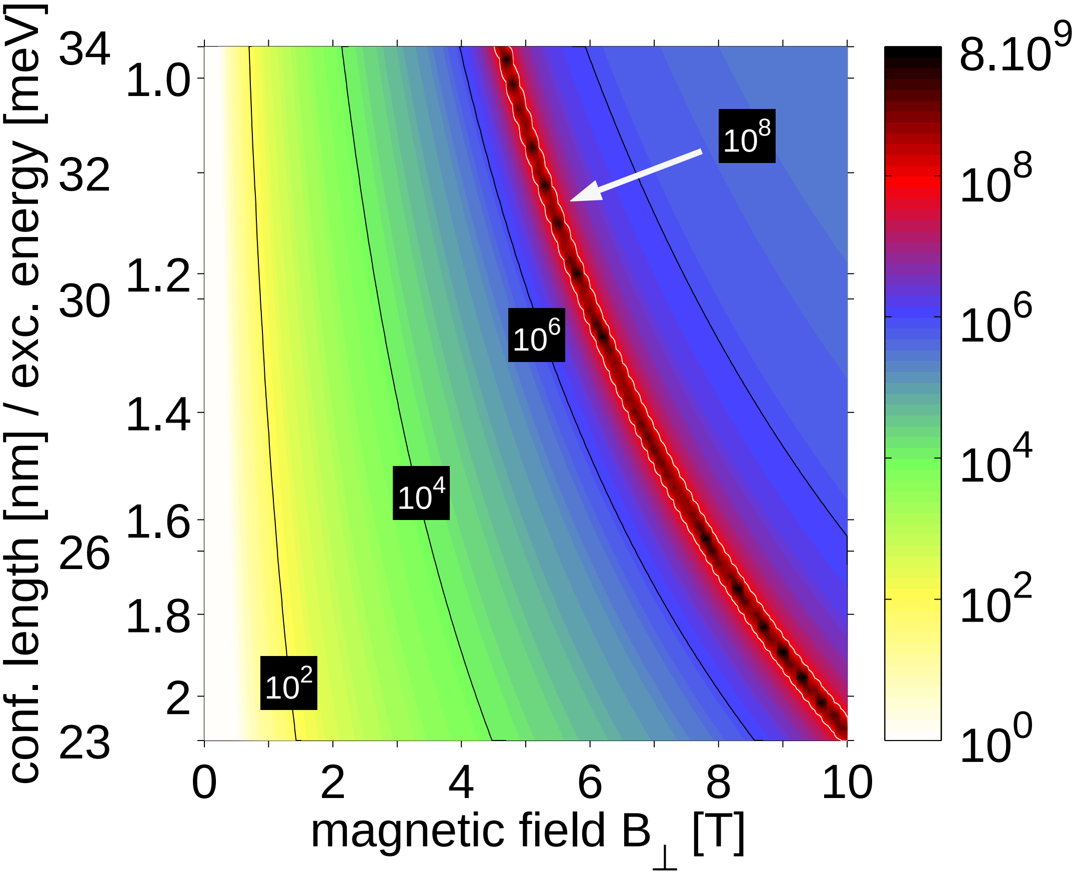

Figure 3.17: Spin relaxation rate in a single quantum dot as a function of magnetic field and the confinement length l_0 / the confinement energy E_0. The rate is given on the logarithmic scale in the units of s^{-1}. The solid lines represent equirelaxation lines.

3.6 Double dots

In our double dot potential the ground (excited orbital) state can be approximated as a symmetric (antisymmetric) combination of two Fock-Darwin functions, $\Psi_{0,0,\uparrow}$, placed at the two potential minima, as was explain in Sec. 2.5.1. What we call here ground, spin and orbital state is denoted in Sec. 2.5.3 as $\Gamma_S^\uparrow$, $\Gamma_S^\downarrow$, and $\Gamma_A^\uparrow$, respectively. Similarly to the single dot case, the most important parameter for the orbital relaxation is the energy difference between the initial and final states, being twice the tunneling energy, obtained by subtracting the two values in Eq. (2.34)

$$2T^{(0)} = \frac{\hbar^2}{ml_B^2} \frac{2d(1-\theta^2)\{1 + d\sqrt{\pi}\mathrm{Erfc}(d) - e^{-d^2}\}}{\sqrt{\pi}\{e^{d^2(1+\theta^2)} - e^{-d^2(1+\theta^2)}\}}, \tag{3.23}$$

where $\theta = B_\perp e l_B^2/2\hbar$. The approximation of Eq. (3.18) for the spin relaxation is correct also here, since Eq. (2.46) does not couple any two of the ground, spin, and orbital states due to a definite symmetry of the L_z operator. There is a coupling through higher excited states with appropriate symmetry, but, as we learn from numerics, this is negligible. Apart from the energy difference, given by the Zeeman energy, for the spin relaxation the anti-crossing plays a dominant role.

3.6.1 In-plane magnetic field

The spin relaxation rate as a function of in-plane magnetic field and the interdot distance is plotted in Fig. 3.18. The rates for small interdot distances are similar to the single dot case, where the rate grows with increasing magnetic field; for low magnetic fields more steeply than for large. The order of magnitude of the rate is given by Eq. (3.19), being about 10^2 s^{-1} at 1 T and 10^5 s^{-1} at 10 T. At large interdot distances the rate is strongly influenced by the presence of a anti-crossing (spin hot spot), which occurs when the Zeeman and twice the tunneling energies are equal. If the tunneling energy is changed from zero to a value of order of the single dot excitation energy, regardless of the magnetic field strength, one always passes through a spin hot spot region, where the spin relaxation is very fast. Fortunately there exist specific orientations of the double dot system and the magnetic field, where this anti-crossing does not occur. We call such a configuration "easy passage."

To understand the angular dependence of the relaxation rate and find conditions for an easy passage it is enough to write the effective Hamiltonian for the spin relaxation, Eq. (3.18), after the rotation into coordinates in which the new x axis lies along the dot's axis **d**, see Sec. 2.6.1. Since there are no orbital effects in in-plane magnetic fields, in these new coordinates the unperturbed solutions of the Hamiltonian H_0 have a definite symmetry under inversions along $\hat{x}$ – the

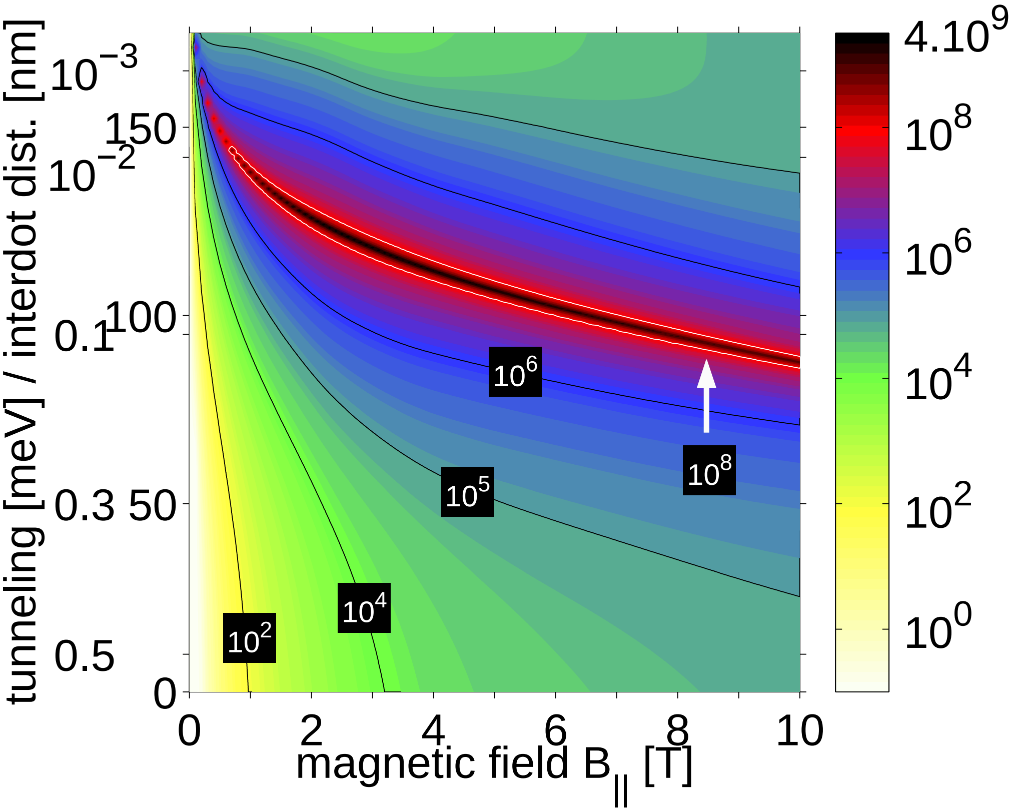

Figure 3.18: Spin relaxation rate in a double quantum dot as a function of in-plane magnetic field for $\gamma = 0°$ and the interdot distance d / tunneling energy $T^{(0)}$, for a confinement length 32 nm. The relaxation rate is given on the logarithmic scale in the units of s^{-1}. The double dot is oriented along [100] ($\delta = 0°$).

ground and spin states are symmetric, while the orbital state is antisymmetric. The transformed H_1 of Eq. (3.18), is

$$\begin{aligned} H_1 = &- \mu B_{\|}\sigma_z\{x[l_{BR}^{-1}\cos(\gamma-\delta) - l_D^{-1}\sin(\gamma+\delta)] \\ &+ y[l_{BR}^{-1}\sin(\gamma-\delta) - l_D^{-1}\cos(\gamma+\delta)]\}. \end{aligned} \tag{3.24}$$

In the single dot case the coefficient A^2 in Tab. 3.2 is proportional to the sum of the squared couplings in Eq. (3.24) at x and y. However, in the double dot case, x and y can couple states differently. For large interdot distances the most important influence on the spin relaxation comes from the anti-crossing of the spin and orbital states, which are coupled by terms with the x-like symmetry. Thus, the anti-crossing will not occur if

$$l_{BR}^{-1}\cos(\gamma-\delta) - l_D^{-1}\sin(\gamma+\delta) = 0. \tag{3.25}$$

The angles γ and δ that satisfy the above equation define an easy passage. Figure 3.19 presents the spin relaxation rate as a function of the tunneling energy and orientation of the in-plane magnetic field for double quantum dot oriented along [100] and [110] directions. For a double dot oriented along [100] direction ($\delta = 0$) the easy passage occurs for an in-plane magnetic field oriented along angle γ given by $\tan\gamma = l_D/l_{BR}$. Similarly to the single dot case, the measured angular dependence recovers the ratio of the spin-orbit couplings, now also revealing which one is larger. As can be seen from Eq. (3.25), both linear Bychkov-Rashba and Dresselhaus (also cubic) spin-orbit terms contribute to the anti-crossing; in single dots it is only the Bychkov-Rashba coupling which gives relevant spin hot spots. The position of the easy passage is then given by an interplay of all the spin-orbit terms. If the double dot is oriented along [110] ($\delta = \pi/4$), the condition for the easy passage is $\gamma = 135°$, being independent on the spin-orbit couplings and thus suitable to use in quantum information processing.

3.6.2 Perpendicular magnetic field

Orbital relaxation rate

There are two different regimes for the orbital relaxation, depending on the energy difference of the ground and orbital states, $E = 2T^{\uparrow}$, which is more sensitive to the interdot distance than to the confinement length. If $dl_0 \ll l_B$, then $E \approx \hbar^2/ml_B^2$, decreasing with increasing the magnetic field or the interdot distance. The limit of high $\mathcal{E}$ applies and the rates are comparable to the single dot case. On the other hand, if $dl_0 \gg l_B$ the energy, and thus also the rates, drop exponentially with increasing the magnetic field or the interdot distance. Due to the complex interplay of the magnetic field and interdot distance, no power law dependence of the rates on magnetic field can be identified. However, approximations in Tab. 3.2 give analytical formulas with a fair agreement with numerics, if the energy difference is approximated by Eq. (3.23), $E \approx 2T^{(0)}$.

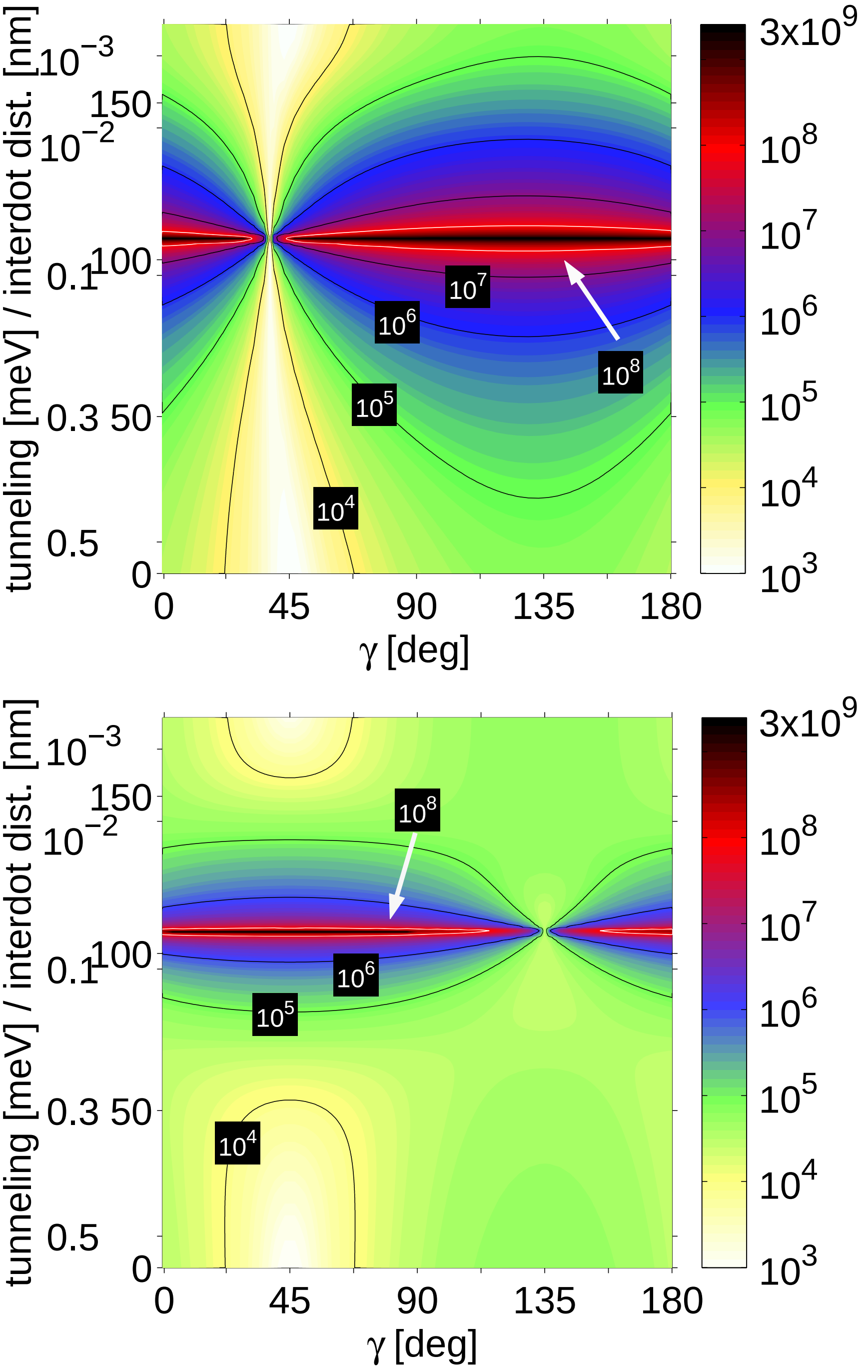

Figure 3.19: Calculated spin relaxation rate, in s^{-1}, of a double quantum dot as a function of γ and tunneling energy, for $B_{||} = 5$ T. Spin hot spots strongly influence spin relaxation at tunneling energies from 0.001 to 0.1 meV. a, The dots are oriented along [100] ($\delta = 0°$). The weakest relaxation is for $\gamma \approx 35°$. b, The dots are oriented along [110] ($\delta = 45°$), with the easy passage at $\gamma = 135°$.

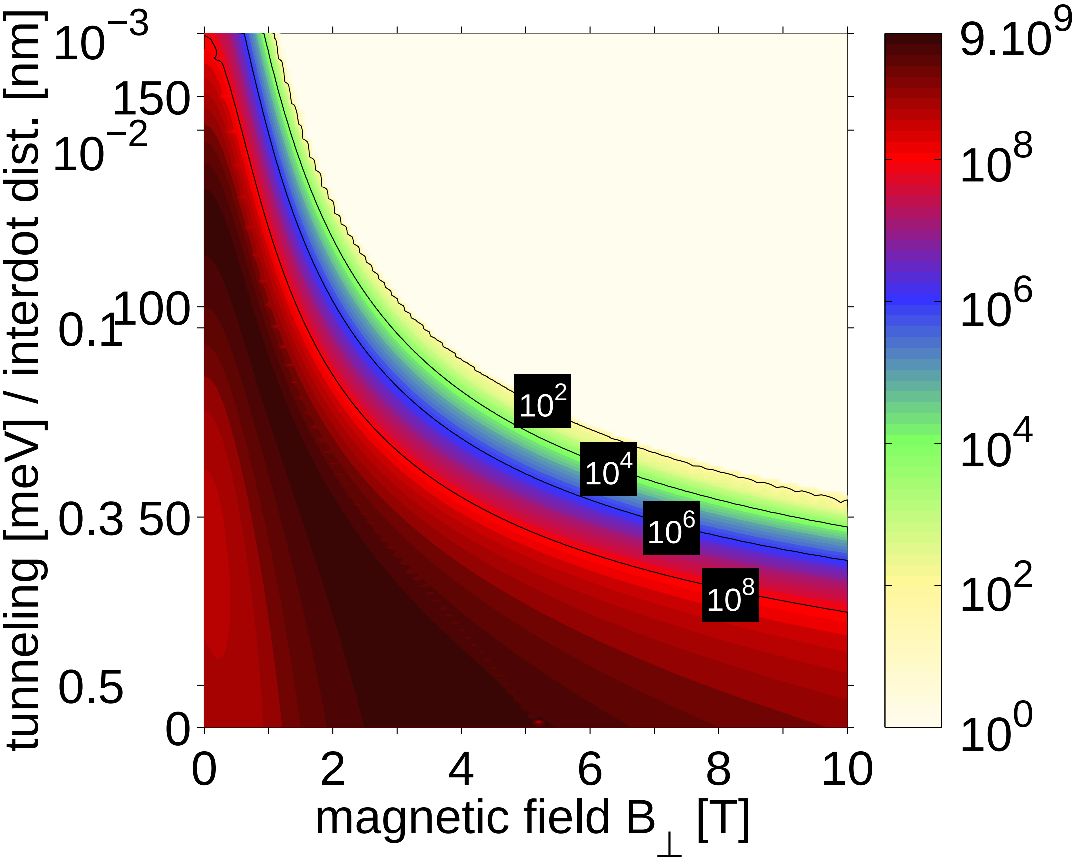

Figure 3.20: Orbital relaxation rate in a double quantum dot as a function of in-plane magnetic field for $\gamma = 0°$ and the interdot distance d / tunneling energy $T^{(0)}$, for a confinement length 32 nm. The relaxation rate is given on the logarithmic scale in the units of s^{-1}. The double dot is oriented along [100] ($\delta = 0°$).

The dependence of the orbital relaxation rate on the magnetic field and the interdot distance is shown in Fig. 3.20. The lower left corner is the regime of the high $\mathcal{E}$ limit. The rate here is similar to the single dot case. The opposite corner is the regime of an exponentially small energy difference and the rate is practically zero. The transition between these two regimes comes for a smaller interdot distance if the magnetic field is higher, since the transition occurs when $d \sim l_B$. Again, as in the single dot case, the anti-crossing does not have a large influence on the orbital rate – in the figure it can hardly be seen. For interdot distances much larger than l_B the dots are effectively isolated.

Spin relaxation rate

Spin relaxation in double dots reveals a surprising complexity as compared to the single dot case. The complexity is due to the strong anisotropy of spin hot spots. While anisotropy appears already in single dots, caused by the interference of the Bychkov-Rashba and Dresselhaus couplings, additional anisotropy appears in spin hot spots. This anisotropy does not require the presence of both couplings. Instead, it is caused by the selection rules for spin-orbit virtual transitions in the double-dot spectrum. Next we discuss the individual contributions of the Bychkov-Rashba and Dresselhaus terms in the spin relaxation rate and, specifically, in the spin hot spot anisotropy.

The contribution to the spin relaxation rate from the Bychkov-Rashba (Dresselhaus) term is shown in the upper (lower) part of Fig. 3.21. For low magnetic fields the rate grows with increasing magnetic field, as we expect from Tab. 3.2. However, similarly to the in-plane magnetic field case, the spin hot spots (ridges in Fig. 3.21) dominate the rate for most of the parameters' range. The interdot distance strongly influences the spin relaxation rate by determining the position of anti-crossings. In high magnetic fields, the spin state can anti-cross higher orbital states depending on the symmetry of these states. However, the influence of these anti-crossings on the rate is limited to a narrow region of magnetic fields, since the dots are effectively isolated at high fields and the crossing states do not comply with the selection rules for spin-orbit couplings of single dot states.

It is interesting to compare the contribution to the spin relaxation by the Bychkov-Rashba and the Dresselhaus terms. Let us first look at the single dot regime, which in Fig. 3.21 is visible at $d = 0$. The spin hot spot appears only for the Bychkov-Rashba term, in line with our earlier observation in Fig. 3.15. The Dresselhaus term becomes effective only in the coupled-dot system in which the symmetry of the lowest orbital states allows the coupling at the level crossings. The coupling is again absent at two isolated dots ($d \to \infty$). Another nice feature seen in Fig. 3.21 is the transformation of the single-dot spin hot spot at about 5 T to a double-dot spin hot spot at lower fields, while the single-dot spin hot spot that starts at about 9 T shifts towards 5 T in the double dot and remains there at all couplings.

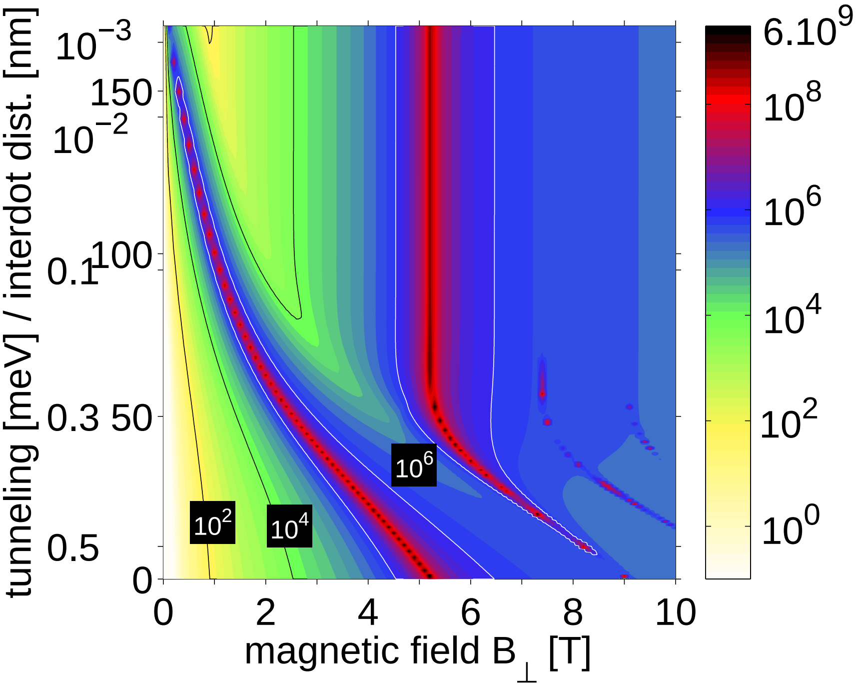

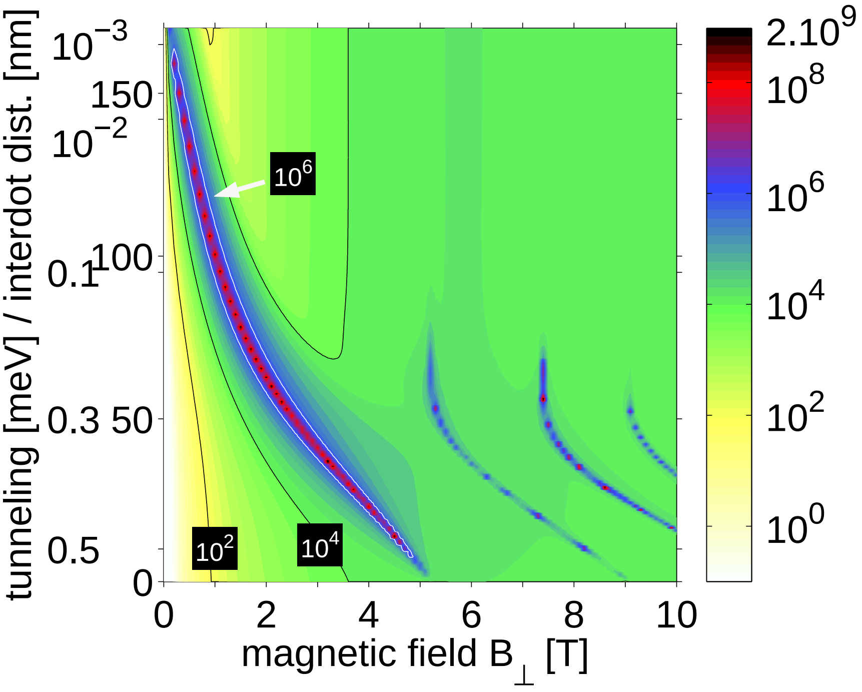

Figure 3.21: Spin relaxation rate as a function of perpendicular magnetic field for $\gamma = 0°$ and the interdot distance d / tunneling energy $T^{(0)}$ (at zero magnetic field only), for a confinement length 32 nm. The relaxation rate is given in logarithmic scale in the units of s^{-1}. The double dot is oriented along [100] ($\delta = 0°$). The upper figure shows results when only the Bychkov-Rashba term is present in the Hamiltonian. In the lower figure, only the Dresselhaus terms are present.

Similarly to the in-plane field case, we can understand the anisotropy of the spin relaxation in perpendicular magnetic field by studying the transformed effective Hamiltonian:

$$\begin{aligned} H_1 =&\mu B_\perp \{x[\sigma_x(l_{BR}^{-1} - l_D^{-1}\sin 2\delta) - \sigma_y l_D^{-1}\cos 2\delta] \\ &+ y[\sigma_y(l_{BR}^{-1} + l_D^{-1}\sin 2\delta) - \sigma_x l_D^{-1}\cos 2\delta]\}. \end{aligned} \tag{3.26}$$

Due to the presence of the orbital effects of the perpendicular magnetic field, the unperturbed states have no specific symmetry under inversions along $\hat{x}$. As a result, only in the limit of low magnetic fields ($l_B \approx l_0$), for us below 1 T, the term in Eq. (3.26) containing x dominates over the term containing y; in higher fields both terms contribute. In this limit the condition for a suppression of the anti-crossing is $l_D = l_{BR}$ and $\delta = 45°$. This we call a "weak passage", since the anti-crossing, while suppressed, is still present. If the condition for a weak passage is not fulfilled, the spin relaxation rate, as a function of δ, still has a minimum at $\delta = 45°$ and a maximum at $\delta = 135°$. However, the ratio between the two extremal values is in general of order 1.

3.6.3 Other growth directions

Thus far we have considered lateral quantum dots defined in a (001) plane of a GaAs heterostructure. A different growth direction leads to a different form of the Dresselhaus spin-orbit interactions[168] (the form of the Bychkov-Rashba term remains unchanged) and to different conditions for the easy passage. Our results are summarized in Tab. 3.4. For [111] growth direction the linear Dresselhaus term has the same form as the Bychkov-Rashba one. Our results easily translate for this case by placing formally $l_D \to \infty$. There will be no spin relaxation anisotropy in single dots, while in double dots spin hot spots vanish for $\cos(\gamma - \delta) = 0$ at in-plane fields. For a general magnetic field a weak passage occurs only at specific spin-orbit parameters, given by $2\sqrt{3}l_{BR} + l_D = 0$ (the couplings can be negative).

A less trivial situation occurs for the [110] grown quantum well. The linear Dresselhaus term has the form

$$H_D = -\frac{\hbar}{4ml_D}\sigma_z P_x \tag{3.27}$$

Unlike the Bychkov-Rashba term, which has eigenspins always in the plane, the [110] Dresselhaus term has eigenspins oriented out of the plane.

For this growth direction, the calculated spin relaxation rate for the double dot system oriented along $\delta = \pi/2$ in an in-plane magnetic field of $B_{||} = 1$ T is shown in Fig. 3.22. The spin hot spots exist for all orientations of the field except at multiples of π. This is confirmed by analytical considerations summarized in Tab. 3.4. The easy passage exists if the dot is oriented along the (rotated) $\hat{x}$, while

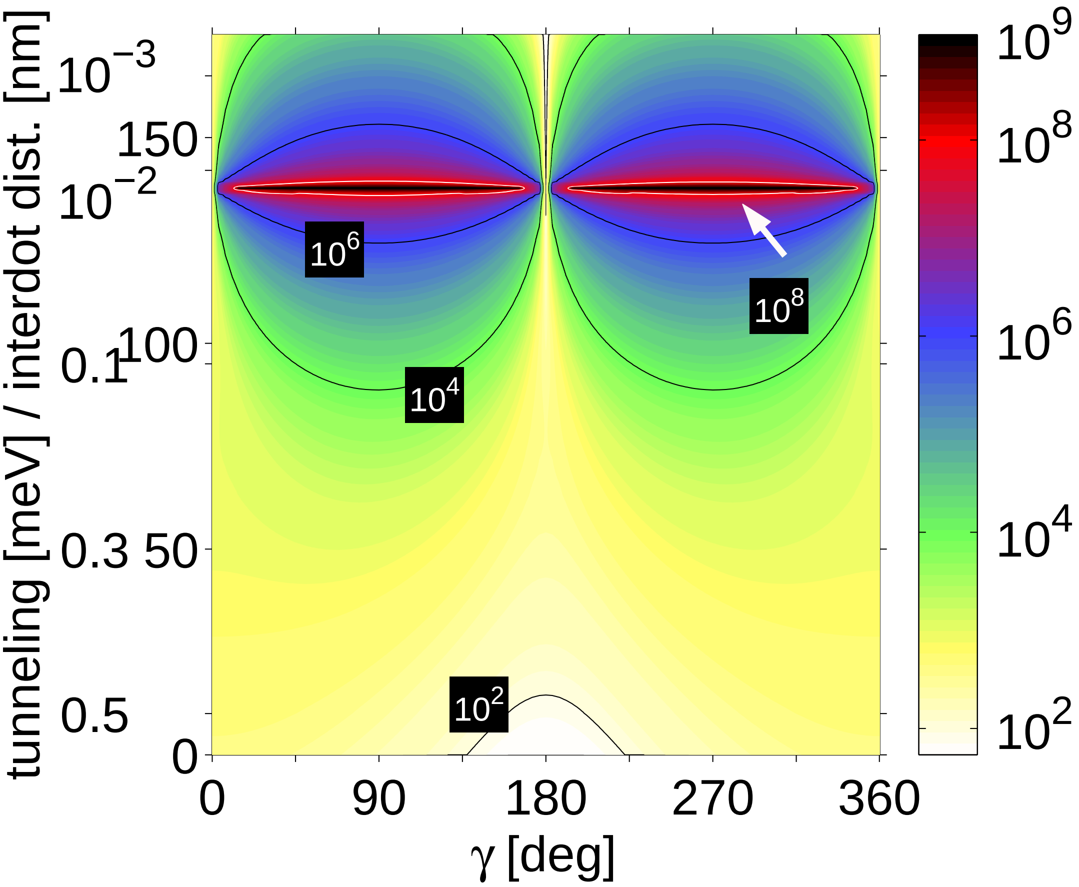

Figure 3.22: Spin relaxation rate as a function of γ and the tunneling energy for $B_{||} = 1$ T, for [110] growth direction. The dot orientation is given by $\delta = \pi/2$. The relaxation rate is given in logarithmic scale in the units of s^{-1}.

growth dir.	in-plane	general
[001]	$l_{BR}\cos(\gamma+\delta) =$ $= l_D\sin(\gamma-\delta)$	$l_D = l_{BR}$, $\delta = \pi/4$
[111]	$\cos(\gamma-\delta) = 0$	$2\sqrt{3}l_{BR} + l_D = 0$
[110]	$\gamma = 0$, $\delta = \pi/2$	$l_{BR}\cos\delta = \pm 2 l_D \cot\xi$, $\sin(\delta-\gamma) = \pm 1$
$[\cos\alpha\ \sin\alpha\ 0]$	$\delta = \pi/2$, $l_D\tan\gamma = -l_{BR}\cos 2\alpha$	$l_D = -l_{BR}\cos 2\alpha$, $\delta = \pi/4$, $\xi = 0$

Table 3.4: Easy passage conditions for several growth directions in an in-plane magnetic field and weak passage conditions for a magnetic field with a nonzero perpendicular component. The z axis points in the growth direction. In addition to γ and δ, defined in Fig. 2.3, angle ξ is the angle between the magnetic field and the z axis.

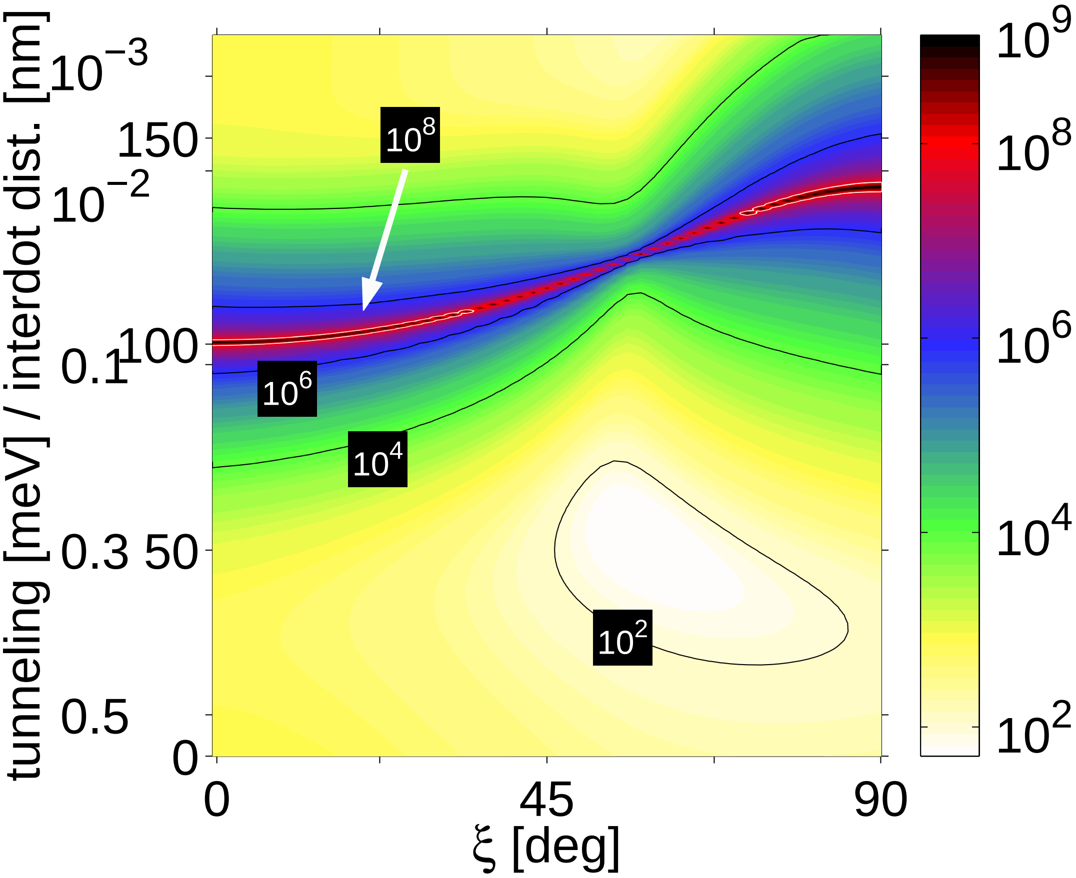

Figure 3.23: Spin relaxation rate as a function of ξ and tunneling energy for $B = 1$ T, for [110] growth direction. The dot orientation is given by $\delta = \pi/2$. The relaxation rate is given in logarithmic scale in the units of s^{-1}.

the in-plane magnetic field is along $\hat{y}$. Also, the [110] Hamiltonian is not invariant under the in-plane inversion of the coordinates which is why the period in γ for the relaxation rate is twice as in the case of the [001] growth direction. However, the part of the Hamiltonian important for anti-crossing is invariant with respect to inversion along $\hat{y}$. Therefore, the results in Fig. 3.19 for $\gamma > \pi$ are equal to those at $2\pi - \gamma$ to a very good approximation.

In order to demonstrate the difference between easy and weak passages, we plot in Fig. 3.23 the calculated spin relaxation rate in double dots defined in a (110) plane. The dots are oriented along $\hat{y}$. From Tab. 3.4 one gets the conditions for the weak passage to be $\gamma = 0$, and, for our spin-orbit couplings, $\xi = 56^\circ$, where ξ is the angle between the magnetic field and $\hat{z}$. This arrangement corresponds to the “neck” in Fig. 3.23. However, contrary to an easy passage, here the width of the anti-crossing region is finite and gets larger with increasing magnetic field (not shown). Since all weak passages we found depend on spin-orbit couplings, they (better, the corresponding geometries) are much less useful for robust inhibiting of spin relaxation than easy passages.

In the above analysis we have not considered the cubic Dresselhaus term, H_{D3}, in deriving the conditions for easy passages. Being cubic, even after rotating the double dot ($\delta \neq 0$), it always has qualitatively the same symmetry properties with respect to inversions about $\hat{x}$ and $\hat{y}$ – it is a sum of two terms, one with symmetry of x and one y. Therefore the presence of H_{D3} does not destroy the easy passage. It can only slightly change the conditions for the easy passage to occur. For our parameters this change, checked numerically, is only on the order of 1° for the of angles in Tab. 3.4, so the linear terms should provide a realistic guidance to experimental demonstrations of the predicted anisotropy.

3.7 Conclusions

In this chapter, we have calculated phonon-induced orbital and spin relaxation rates of single electron states in single and double quantum dots. The rates were calculated as a function of in-plane and perpendicular magnetic fields, as well as a function of the field and (in the case of double dots) dots’ orientation. Realistic, GaAs defined, electron-phonon piezoelectric and deformation potential Hamiltonians were considered. Similarly, relevant spin-orbit interactions, namely the Bychkov-Rashba and linear and cubic Dresselhaus couplings, were used to calculate the spin relaxation rate. We have supported our numerical findings by analytical models based on perturbation theory, deriving effective Hamiltonians which display, in the lowest order, all the important effects seen in numerics. We have proposed using a classifying dimensionless parameter $\mathcal{E}$ which allows to obtain relevant trends and order-of-magnitude estimates in important limiting cases.

In the case of single dots, we have carefully analyzed the theoretically predicted anisotropy of the spin relaxation rate in an in-plane magnetic field. The anisotropy comes from the interplay of the linear Bychkov-Rashba and Dresselhaus terms (if only one of the terms dominates, the anisotropy is absent). Experimental verification of the anisotropy would give a strong evidence of the spin-orbit mechanism of spin relaxation. Furthermore, such a measurement would enable to estimate the ratio of the two relevant spin-orbit terms.

For single dots in a perpendicular magnetic field, which causes cyclotron effects as well as the Zeeman splitting, we have numerically investigated the orbital relaxation rate. In addition, we have provided a simple analytical scheme to estimate the rates in the important limits of low and high magnetic fields, and found the corresponding rate as a function of the confining length. The orbital relaxation rate is found to be of the order of 10^9 s^{-1}, with a relatively small dependence on the magnetic field. At anti-crossings the orbital relaxation rate is reduced by a factor of two. At low magnetic fields the rate is dominated by the deformation potential electron-phonon interaction, while at high fields it is dominated by piezoelectric phonons.

On the other hand, the spin relaxation in single dots is always dominated by piezoelectric transversal phonons. The contribution of deformation potential phonons is more than a decade smaller. The rate is of the order of 10^5 s^{-1} over a large region of parameters (magnetic field and excitation energy). However, the rate is strongly enhanced in the region of anti-crossing/spin hot spot, where it becomes comparable to the orbital relaxation rate. We have also provided analytical estimates of the rate (away from the spin hot spots) for various phonon contributions, at the limits of low and high magnetic fields.

The physics is more complex in coupled dots. We have numerically studied spin relaxation in double dots in in-plane magnetic fields, in which the rate is strongly anisotropic in the direction of both the magnetic field and the dots' axis. Similarly to the single dot case, the piezoelectric phonons dominate spin relaxation here. We have demonstrated that a spin-hot spot exists at useful magnetic fields (say, 1 T) and interdot couplings (0.1-0.01 meV). In fact, a spin hot spot is a typical phenomenon in symmetric double dots since it appears when the tunneling energy becomes comparable to the Zeeman splitting. Fortunately, the spin hot spots are strongly anisotropic, due to the symmetry of the lowest orbital electronic states, and they vanish at certain orientations of the field and the dots' axis. We have systematically investigated these "easy passages" using an analytical model. We have found the criteria for the absence of spin hot spots for different growth directions of the underlying quantum well. These criteria should be seriously considered in fabricating double dot systems for spin-based quantum information processing which requires low spin relaxation.

For double dots in a perpendicular magnetic field, the orbital relaxation rate is most influenced by the energy difference of the corresponding coupled states. The energy has a range over eight orders of magnitude due to cyclotron effects on the interdot coupling. As in the single dot case, both deformation potential and

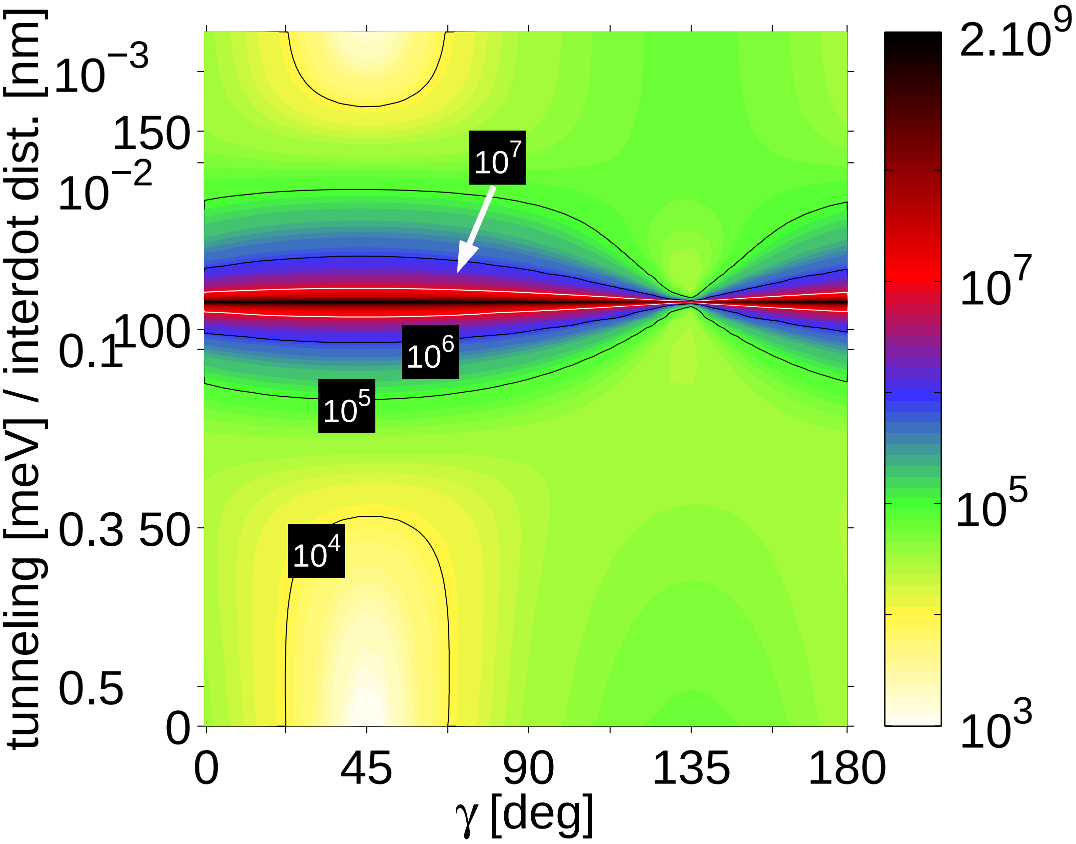

Figure 3.24: Spin relaxation rate in a double dot as a function of the orientation of the in-plane magnetic field and tunneling energy for $B = 5$ T, for [001] growth direction. The dot orientation is given by $\delta = \pi/4$. A small asymmetric term is added into the confinement potential (an electric field of 10^3 V/m in y direction is applied in on one of the dots). By this, the easy passage is turned into a weak passage – compare with Fig. 3.19.

piezoelectric phonons can dominate the orbital relaxation. The spin relaxation in double dots in a perpendicular field has similar qualitative features as in the single dot case, with an additional anisotropy given by the orientation of the double dot with respect to the crystallographic axes. However, unlike in in-plane fields, only weak easy passages (in which spin hot spots form a neck on the parameter map, rather than disappear altogether) exist in a perpendicular magnetic field. We have also observed a nice shift of spin hot spots to the lower field neighbors as the tunneling between the dots decreases. While the perpendicular fields provide a nice opportunity to study fundamental physics of double dot systems, they are less useful in quantum information processing due to the omnipresence of spin hot spots and weak passages.

Our final note concerns the symmetry of the double dot. Do our conclusions hold if the symmetry is broken? The answer is yes, if the double-dot system still possesses either x- or y-like symmetry. Suppose, for example, that a weak electric field is applied along $\hat{x}$ or $\hat{y}$, or one of the dots is somewhat smaller than the other. The spin hot spot anisotropy still leads to easy passages in spin relaxation in in-plane magnetic fields. On the other hand, if the symmetry breaking is xy-like (an electric field pointing along a diagonal, for example), the easy passage is destroyed since the selection rules for the lowest orbital states will allow coupling of the states by the term containing y in H_1 of Eq. 3.24 (recall that it was the vanishing of the term containing x that lead to the appearance of easy passages). This situation is demonstrated in Fig. 3.24. A double dot system in an in-plane field of 5 T is oriented along [110] (the growth direction is [001]). If the double dot is symmetric, an easy passage exists for $\gamma = 135°$, see Fig. 3.22. However, if one of the dots is subject to a y-like electric field, so that the overall symmetry of the perturbation is xy-like, the easy passage turns to a weak passage – at all directions of the in-plane magnetic field there exists an interdot coupling in which the spin relaxation rate is greatly enhanced. This is another important message for spin-based quantum information processing in quantum dots.

Chapter 4

Adding resonant field

Starting with an electron in a quantum dot with dissipation, as analyzed in Chapters 2 and 3, we now add oscillating electric and magnetic fields. Such fields induce Rabi oscillations between electron eigenstates. We first overview shortly the tasks that can be accomplished using oscillating fields in quantum dots and next we present our results about the role of the spin-orbit interactions in the resonant field induced Rabi oscillations.

4.1 Oscillating field in a quantum dot

Resonantly induced Rabi oscillations due to oscillating fields are a most often used method for controlled qubit manipulations. The advantage of this method is a high energy selectivity – only the states whose energy difference matches exactly the frequency of the field are influenced. By changing the amplitude of the resonant field one can control the speed of the operation.

The need for controlled manipulations comes from quantum information processing, where qubit gates are basic building blocks of a quantum processor. A qubit gate is a unitary operation that brings an initial state into a final state according to a specific rule (an example is the NOT operation which makes spin up into spin down and vice versa). The required unitary operation is achieved by a proper interaction which acts on the system for a suitable time. For example, the previously mentioned NOT operation can be accomplished by turning on a magnetic field in a perpendicular direction to the spin quantization axis for such a time that the spin precesses by angle π.

Manipulation of a quantum dot charge qubit by a resonant electric field was demonstrated in Ref. [126]. Nuclear magnetic resonance is an example of a spin resonance technique with a wide range of practical applications. In a quantum dot the possibility of a selective manipulation of spin qubits by resonant magnetic field was demonstrated using the idea of g-factor modulation.[94] Experimentally, however, an oscillating electric field is much more convenient to handle compared to the magnetic field. Therefore, it was proposed to exploit the spin-orbit interaction, which allows to manipulate the spin by the electric field. It was shown that in quantum well the electric field is comparably efficient as the magnetic field for experimentally used fields' strengths.[134] In GaAs quantum dot, an oscillating in-plane electric field of $10^2 - 10^3$ V/m is as effective as an oscillating magnetic field of 1 mT for realistic spin-orbit parameters, in a static magnetic field of 1 T.[74]

Recently, the influence of dissipation,[8] double dot symmetry,[152] intense fields,[91] detuning from the resonance,[35] quantum character of the oscillating field,[80] and other factors on the Rabi oscillations in quantum dots were studied. Impetus has come from remarkable experimental progress – Rabi oscillations were observed in a double electron double dot[128] and an on-chip coherent manipulation of single electron spin was demonstrated in Ref. [105]. It is worth to mention that Rabi oscillations are a crucial method for manipulation of trapped ions, together with optical shelving.[121] The latter is a resonance induced population inversion due to different relaxation rates and has been shown to work also in quantum dots.[143]

Similarly as starting and stopping the rotation of the qubit by turning on and off the oscillating field, the current through the dot can be also controlled. Namely, if electron states in two dots or in the dot and in the leads are misaligned, the oscillating field can provide the energy needed to overcome the barrier due to misalignment, which without the field blocks the current.[19, 148, 144] The induced current is known as photon assisted tunneling.[20, 17] Recently, the same concept, where the two states between which the current is blocked without the resonant field have different spins lead to proposals for spin pump (the resonant field induces a spin-polarized current even if no voltage is applied),[139] spin battery (given spin species are flipped into the opposite in both leads),[46, 44] spin filter (only one of the spin species can go through the dot from one reservoir into the second).[138] It was also shown how from the resonant width of the pumped current the spin decoherence time can be obtained.[56, 55]

4.2 Spin-orbit influence on induced Rabi oscillations

We continue studying the role of spin-orbit interactions in orbital and spin qubits realized by single electron double quantum dot. We use the results of Chapter 2 to get the electron wavefunctions and energies, while phonon-induced relaxation rates are computed according to Chapter 3. In this chapter we add an oscillating resonant electric and magnetic fields. We aim at quantifying the influence of the spin-orbit interactions on the spin (the resonant states are the ground state and its Zeeman split twin) and the orbital (resonance between the ground state and the lowest orbital excited state) electron resonance.

The main result of this chapter is the identification of effective dipolar electric and magnetic couplings between resonant states. The dependence of these couplings on the orientation of the dots, with respect to the crystallographic axes, as well as on the orientation of the static magnetic field allows to control the resonance strength induced by electric and magnetic fields individually. For example, a specific contribution to the spin resonance from the oscillating electric field can be turned off by proper orientation of the static magnetic field.

In the rest of the chapter we first describe the electron in the dissipative phonon environment under oscillating electric and magnetic fields using reduced density matrix. Then we list analytical results for a two level approximation, showing how the decoherence and relaxation rates can be obtained from measurable quantities (the excited population, the Rabi frequency, and the absorption). We also show how these can be obtained from a steady current measurement. Finally, with the effective spin-orbit Hamiltonian we evaluate the matrix elements of oscillating magnetic and electric fields for the case of spin and orbital resonance.

4.3 Model

We consider a single electron in a double quantum, as described in Chapter 2. Here we use a confinement length 32 nm and values of spin-orbit couplings from Chapter 3. In this chapter, we consider only an in-plane static magnetic field. We now describe the influence of the phonon environment as well as of the oscillating electric and magnetic fields.

The phonon environment leads to the relaxation and decoherence expressed, in the Markov approximation, by the time derivative of the diagonal and off-diagonal elements of the reduced density matrix of the electron, ρ:[15]

$$\begin{aligned}\partial_t|_{\rm ph}\,\rho_{ii} &= -\sum_k 2\Gamma_{ik}\rho_{ii} + \sum_k 2\Gamma_{ki}\rho_{kk},\\ \partial_t|_{\rm ph}\,\rho_{ij} &= -\sum_k (\Gamma_{ik}+\Gamma_{jk})\rho_{ij} \equiv -\gamma_{ij}\rho_{ij}.\end{aligned} \tag{4.1}$$

Here $2\Gamma_{ij}$ is the relaxation rate from the electron state i to j due to the piezoelectric and deformation potential interactions of the electron with acoustic phonons. There is no additional phonon channel for the decoherence γ_{ij} apart from the relaxation, since the phonon density of states vanishes for zero phonon energy, $\Gamma_{ii}=0$. We do not consider non-phonon mechanisms of dephasing, which are important at low magnetic fields, $B_{||} \lesssim 1$ T. To allow for a finite temperature one can suppose a detailed balance: $\Gamma_{ji} = \tau\Gamma_{ij}$, where $\tau = \exp(-\hbar\omega_{ji}/k_BT)$. In the calculations below, we consider temperature much lower than the orbital excitation energy. For example, the experiment Ref. [105] was done at temperature 100 mK, corresponding to ~ 0.01 meV, while a typical excitation energy of the used quantum dot was about 1 meV. In this limit the transitions into higher orbital levels have negligible rates. The decoherence rate for both spin and orbital resonance is then given by the relaxation between the resonant states only,

$$\gamma_{ba} = \Gamma_{ba} + \Gamma_{ab} = \Gamma_{ba}(1+\tau), \tag{4.2}$$

where a and b are indexes of the resonant states. Equation (4.2) is valid at low temperatures, independent on other parameters, due to the fact that the relaxation rates including spin flip are much smaller than the transition rates between the spin alike states.

In addition to phonons, the electron is subject to oscillating electric and magnetic fields, which contribute through the following Hamiltonian:

$$H^{\rm of} = 2[e\mathbf{E}^{\rm of}.\mathbf{r} + (g/2)\mu_B \mathbf{B}^{\rm of}.\boldsymbol{\sigma}]\cos\omega t \equiv 2\hbar\Omega\cos\omega t. \tag{4.3}$$

Only the in-plane components of the oscillating electric field are relevant. The oscillating magnetic field is perpendicular to the plane, $\mathbf{B}^{\rm of} \propto \hat{z}$, simulating the conditions in the experiment.[105] In the numerical calculations we set $E = 1000$ V/m as a realistic guess for the experimental setup[104] and $B_{||} = 1$ mT, a typical value from the experiment.[105] We suppose the frequency ω be close to the energy difference of a given pair of states – resonant states – denoted by indexes a and b, such that $\omega \approx \omega_{ba} \equiv (E_b - E_a)/\hbar > 0$. In the rotating wave approximation,[15] that we adopt, the oscillating field influences only the two resonant states by opening an additional transition channel:

$$\begin{aligned} \partial_t|_{\rm of}\,\rho_{aa} &= 2(\rho_{bb}-\rho_{aa})J, \\ \partial_t|_{\rm of}\,\rho_{bb} &= 2(\rho_{aa}-\rho_{bb})J. \end{aligned} \tag{4.4}$$

The Rabi frequency J is determined by the oscillating field matrix element Ω_{ba} and the decoherence rate between the resonant states, γ_{ba}. Away from resonance, $\omega = \omega_{ba}$, the Rabi frequency decays with the Lorentzian shape,

$$J = |\Omega_{ba}|^2 \frac{\gamma_{ba}}{(\omega_{ba}-\omega)^2 + \gamma_{ba}^2}. \tag{4.5}$$

Finally, even though it is not currently measurable in a single electron system, we include in our list of interesting resonance parameters the absorption,

$$W = \frac{\rm d}{{\rm d}t}|_{\rm of} \sum_i E_i \overline{\rho}_{ii}, \tag{4.6}$$

defined as the energy gain of the electron due to the oscillating field.

4.4 Resonance in a two level model

In order to obtain useful resonant characteristics we calculate the steady state density matrix $\overline{\rho}$. Our numerical strategy to obtain $\overline{\rho}$ is as follows: We diagonalize the coupled dots electron Hamiltonian, Eq. (2.2), and compute the relaxation rates using Fermi's Golden rule. We choose a pair of resonant states, {a, b}, and after evaluating Ω_{ba} we find the Rabi frequency according to Eq. (4.5). Finally, we find the steady state density matrix by solving the set of linear equations defined by $\partial_t|_{\mathrm{ph}}\overline{\rho} + \partial_t|_{\mathrm{of}}\overline{\rho} = 0$. A different method, with the oscillating field treated exactly, was used for single dot qubit in intense oscillating fields,[91] three orders of magnitude larger than the fields considered here.

Apart from the case of optical shelving,[121] whereby the electron is trapped in a dark state, it is enough to consider the basis for the density matrix to consist of only the two resonant states. The physics is then characterized by the number $J_0^r = \Gamma_{ba}^{-1} J|_{\omega=\omega_{ba}}$ which is the Rabi frequency at the resonance, measured in units of the relaxation rate between the resonant states.

Two limits can be identified, according to J_0^r. (i) If the Rabi frequency dominates the relaxation, $J_0^r \gg 1$, the probability to find the electron in the ground or exited state is almost the same. In this regime the coherent oscillation of the electron is occasionally interrupted by a relaxation. (ii) If $J_0^r \ll 1$, immediately after the electron is excited by the oscillating field it relaxes back to the ground state. The probability to find the electron in the excited state then differs from the thermal equilibrium value in proportion to J_0^r. The absorption is proportional to the electron transition rate from the excited state to the ground state times the energy dissipated at this transition. The transition rate equals the relaxation rate for strong enough oscillating field, $J_0^r \gg 1$, while it is limited to the Rabi frequency for weak fields, $J_0^r \ll 1$. The frequency full widths at half maximum (FWHM) also differ for the two limits – see Tab. 4.1 for analytical results.

Figure 4.1 presents our numerical results for the Rabi frequency, excited population width, and decoherence as functions of the tunneling energy for the spin and orbital resonance. Both resonances are in the regime of $J_0^r \gg 1$, where the decoherence is revealed by the FWHM of the Rabi frequency, see Tab. 4.1, while the relaxation rate can be obtained if both the Rabi frequency at resonance and FWHM of the excited population are known, too. Due to Eq. (4.2), the relaxation rate is indiscernible from the decoherence in the figure and J_0^r can be directly determined. For the spin resonance J_0^r varies between 10^5 and 10^{11} – the limit expressions in Tab. 4.1 are then exact with this precision. The upward dips in FWHM and the decoherence rate are due to the anti-crossing of the spin and orbital states. It is interesting that the Rabi frequency is not influenced by the anti-crossing. This is because both the square of the matrix element and the decoherence (equal to the relaxation) in Eq. (4.5) depend on the anti-crossing in the same way and the contributions cancel.

Comparing to the spin resonance, the orbital resonance is much less sensitive

a	steady state	at resonance	FWHM ($\delta\omega_{1/2}^2$)
$\overline{\rho}_{bb}$	$\frac{J+\tau\Gamma_{ba}}{2J+\Gamma_{ba}(1+\tau)}$	$\frac{J_0^r+\tau}{2J_0^r+1+\tau}$	$\frac{8J_0^r(1+J_0^r)+4\tau(1+\tau+3J_0^r)}{J_0^r-\tau(1+\tau+3J_0^r)}\gamma_{ba}^2$
J	$\frac{\lvert\Omega_{ba}\rvert^2\gamma_{ba}}{(\omega_{ba}-\omega)^2+\gamma_{ba}^2}$	$\lvert\Omega_{ba}\rvert^2/\gamma_{ba}$	$4\gamma_{ba}^2$
W	$E_{ba}J\frac{2(1-\tau)}{1+\tau+2J/\Gamma_{ba}}$	$E_{ba}J\frac{2(1-\tau)}{1+\tau+2J_0^r}$	$\frac{4(1+\tau+2J_0^r)}{1+\tau}\gamma_{ba}^2$

b	limit	at resonance	FWHM ($\delta\omega_{1/2}^2$)
$\overline{\rho}_{bb}$	$J_0^r \gg 1$	$1/2-(1-\tau)/2J_0^r$	$8J_0^r\gamma_{ba}^2/(1-3\tau)$
$\overline{\rho}_{bb}$	$J_0^r \ll 1$	$\frac{\tau}{1+\tau}+J_0^r(1-\tau)/(1+\tau)^2$	$4\gamma_{ba}^2$
W	$J_0^r \gg 1$	$E_{ba}\Gamma_{ba}(1-\tau)$	$8\lvert\Omega_{ba}\rvert^2\gamma_{ba}\Gamma_{ba}^{-1}/(1+\tau)$
W	$J_0^r \ll 1$	$2E_{ba}J^r(1-\tau)/(1+\tau)$	$4\gamma_{ba}^2$

Table 4.1: (a) Steady state, value at resonance, and frequency full width at half maximum (FWHM) $\delta\omega_{1/2}$ squared for the excited state population $\overline{\rho}_{bb}$, the Rabi frequency J, and absorption W. Note that the FWHM of the excited population is defined only if the temperature is low enough such that $J_0^r \geq \tau(1+\tau)/(1-3\tau)$. (b) The value at the resonance, and frequency full width at half maximum of the excited population and absorption in the two limits.

to the anti-crossing, since only in a very narrow region at the anti-crossing the relaxation rate acquires a factor one half. One also sees that J_0^r is smaller, meaning it is easier to get into the regime of $J_0^r < 1$ by lowering the amplitude of the oscillating electric field. Reaching this regime, the decoherence can be obtained from the FWHM of the excited population or from the Rabi frequency.

4.4.1 Current through the dot

As described in the previous section, probing the electron qubit by a resonant oscillating field can reveal the relaxation and decoherence times. For that, however, the excited population and Rabi frequency have to be known. We show here how these can be extracted from current measurements. For this purpose we open the system by coupling it to the left and right reservoirs in the regime of transient current, as depicted in Fig. 4.2. Such a configuration was studied in Ref. [56] under more general conditions. We consider a simplified model which allows simple physical interpretation. We suppose no dependence of the coupling rates, Γ_L and Γ_R, on the electron state. Opening the dot adds additional terms to Eqs. (4.1), and (4.4), namely

$$\begin{aligned} \partial_t|_{\mathrm{lead}}\rho_{bb} &= -\Gamma_R\rho_{bb} + \Gamma_L\rho_0, \\ \partial_t|_{\mathrm{lead}}\rho_{aa} &= (\Gamma_R + \Gamma_L)\rho_0. \end{aligned} \tag{4.7}$$

Here we denote the population probability of the empty state as ρ_0. Due to the normalization of the density matrix it holds $\rho_0 = 1 - \rho_{bb} - \rho_{aa}$. We neglect any coherences including the empty dot since these would include electrons in the

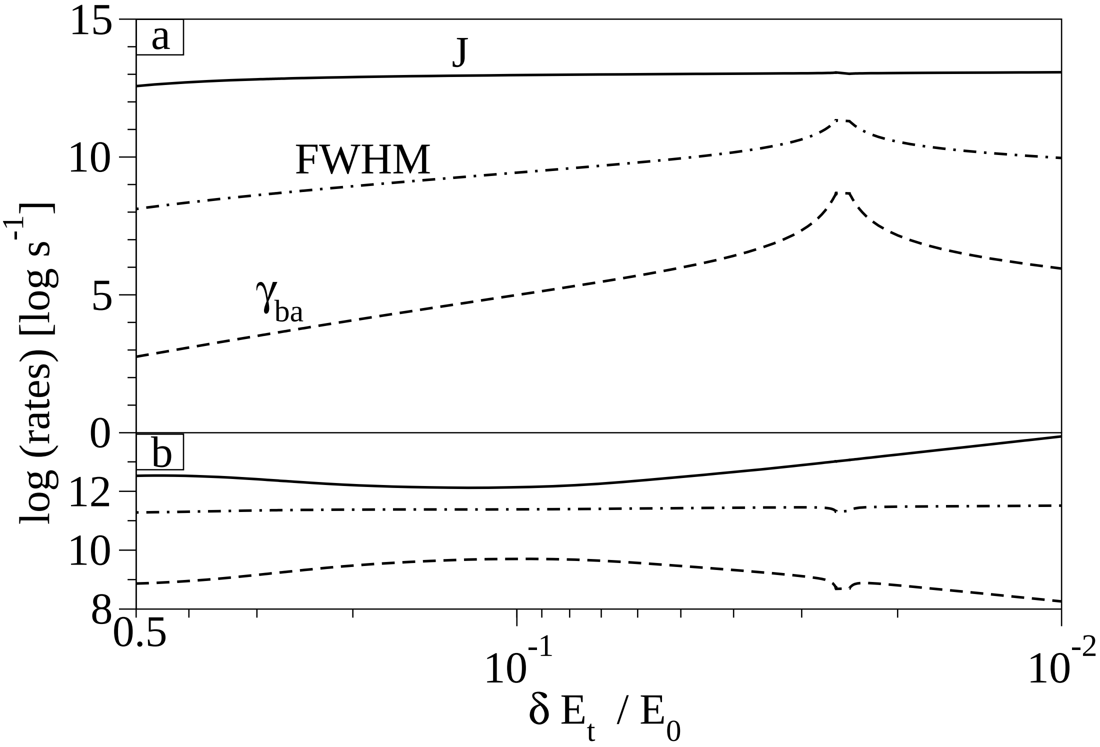

Figure 4.1: Calculated Rabi frequency J at resonance (solid), decoherence γ_{ba} (dashed), and the FWHM of the excited population (dot-dashed) as functions of the ratio of the tunneling energy T and the confinement energy E_0 for (a) spin resonance and (b) orbital resonance. The static in-plane magnetic field is $B_{||} = 1$ T. If the solid line is above (under) the dashed one, it means that $J_0^r > 1$ ($J_0^r < 1$). The dots are oriented along [100], while the static magnetic field lies along [010].

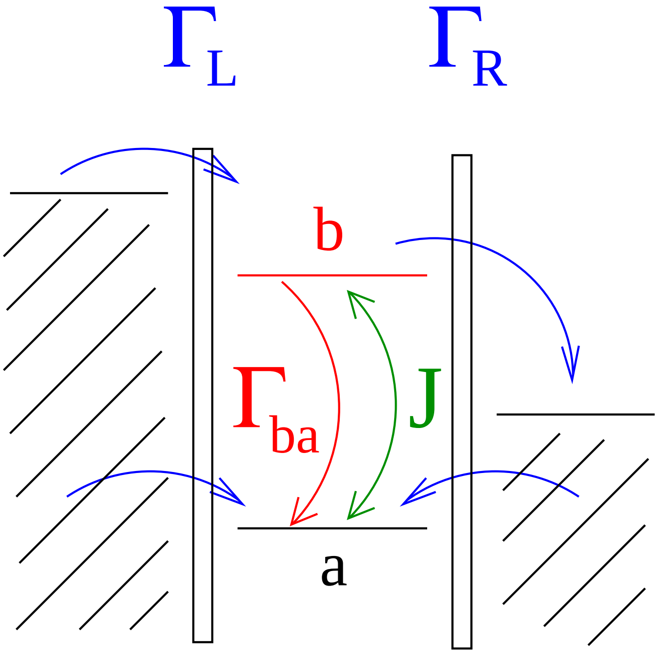

Figure 4.2: A two level model of a quantum dot with dissipation (described by a relaxation rate Γ_{ba}). The applied oscillating field induces the Rabi frequency J. The dot is connected to the left and right leads, each characterized by a single tunneling rate (Γ_L and Γ_R). The electron can enter the ground state of an empty dot from any lead, while the excited state can be filled only from the left lead. Once in the dot, the electron can leave only from the excited state to the right lead.

leads. We solve for the steady state solution in the two level basis and find the current through the dot to be

$$I = \frac{\Gamma_L \Gamma_R (J + \Gamma_{ba}\tau)}{\Gamma_R[\Gamma_R + 3J + \Gamma_{ba}(1+2\tau)] + \Gamma_L\{\Gamma_R + 2[2J + \Gamma_{ba}(1+\tau)]\}}. \tag{4.8}$$

If the couplings to the leads are tuned to be small, $\Gamma_R, \Gamma_L \ll J + \tau\Gamma_{ba}$, the current will be proportional to the occupation of the excited state $\overline{\rho}_{bb}$. If $\Gamma_L \ll \Gamma_R$, the left lead is the current bottleneck and the current is $I = 2e\Gamma_L\overline{\rho}_{bb}$; If $\Gamma_R \ll \Gamma_L$, the current is $I = e\Gamma_R\overline{\rho}_{bb}$. In the opposite regime, when the couplings to the leads are large, $\Gamma_R, \Gamma_L \gg J + \tau\Gamma_{ba}$, the current is proportional to the excitation rate from the ground to the excited state $I = 2(J + \tau\Gamma_{ba})\Gamma_L/(\Gamma_L + \Gamma_R)$, valid for any relative strength of the couplings. By the current measurement in the transient regime it is thus possible to measure the excited state population, or the Rabi frequency, by changing the coupling to the leads. The value of the Rabi frequency in Fig. 4.1 gives an example what are large and small values for the couplings.

4.4.2 Effective spin-orbit Hamiltonian

Once again, the spin-orbit influence on the matrix elements of oscillating fields follows from the effective spin-orbit Hamiltonian Eq. (2.45)

$$H_1 = H_{D3} + H_{\text{lin}}^{(2)} + H_Z^{(2)} + H_{D3}^{(2)}, \tag{4.9}$$

where the individual terms are listed in Eqs. (2.46)-(2.48). As explained in Sec. 2.6.1 and used already in Chapter 3, see Eq. (3.24), we rotate the axes to lay along the main axes of the potential, whereby the effective linear spin-orbit couplings in $H_Z^{(2)}$ obtain the following form

$$h_1^x = l_{BR}^{-1}\cos(\gamma - \delta) - l_D^{-1}\sin(\gamma + \delta), \tag{4.10}$$

$$h_1^y = l_{BR}^{-1}\sin(\gamma - \delta) - l_D^{-1}\cos(\gamma + \delta). \tag{4.11}$$

Since the magnetic field is in-plane, $\hat{\mathbf{h}}_\mathbf{2} = \mathbf{0}$. It is important that the couplings can be selectively turned to zero by orienting the in-plane magnetic field $\mathbf{B}_{||}$ in a direction (γ) dependent on the orientation of the double dot (δ).

The term H_{lin}, Eq. (2.46) is untouched by the rotation. The result of the rotation in Eq. (2.48) is not presented here; we will, however, discuss its relevant parts. For the following discussion the symmetries of the terms of H_1 are important. First, each term has a definite time reversal symmetry: $H_Z^{(2)}$ is antisymmetric, while the other terms are time reversal symmetric. Second, the spatial symmetry of a particular term is defined by a combination of x, y, P_x, and P_y it contains.

We will now quantify individual contributions of oscillating fields to the matrix element Ω_{ba}. We will show where these contributions originate and how they can be used to control the electron spin and orbital resonance.

4.5 Matrix elements for the spin resonance

Consider exact states $\overline{\Gamma}_{1\uparrow}^{00}$ and $\overline{\Gamma}_{1\downarrow}^{00}$, and a general Hermitian operator O. Let us write the matrix element in the following form:

$$\langle\overline{\Gamma}_{1\uparrow}^{00}|O|\overline{\Gamma}_{1\downarrow}^{00}\rangle = \langle\Gamma_{1\uparrow}^{00}|O|\Gamma_{1\downarrow}^{00}\rangle + \delta O, \tag{4.12}$$

where δO is due to spin-orbit corrections. If the first term is nonzero, that is the unperturbed states are coupled by O, δO can be usually neglected. If the first term vanishes, and we are away from the anti-crossing, $\beta \ll 1$, the time inversion symmetry gives an important information about the matrix element δO. Indeed, if O has a definite time reversal symmetry, $T(O) = 1(-1)$ when being symmetric (antisymmetric), the matrix element in the lowest order in H_1 is[158, 98]

$$\begin{aligned}\delta O =& \sum_{i,j,\sigma} \langle\Gamma_{1\uparrow}^{00} O \Gamma_{i\sigma}^{j}\rangle\langle\Gamma_{i\sigma}^{j} H_1 \Gamma_{1\downarrow}^{00}\rangle \times \\ &\times \left(\frac{1}{E_{1\downarrow}^{00} - E_{i\sigma}^{j}} - \frac{T(H_1)T(O)}{E_{1\uparrow}^{00} - E_{i,-\sigma}^{j}} \right),\end{aligned} \tag{4.13}$$

where i denotes the symmetry class, j denotes, for brevity, both upper orbital indexes, and σ denotes the spin. In this lowest order, the contributions from terms in H_1 are additive and can be considered separately. Therefore the first order contributions of the terms with the same time reversal symmetry as O will be suppressed by a factor of order of E_Z/E_0, comparing to matrix elements between states with different spatial indexes. Near the anti-crossing the terms containing coefficients α and β dominate other terms in Eqs. (2.55)-(2.56) and the matrix elements are then proportional to these coefficients – the suppression does not take place.

These general results can be applied to the spin resonance due to magnetic and electric fields. The oscillating magnetic field $[\hbar\Omega = \mu B_z^{\rm of}\sigma_z]$ couples the unperturbed states:

$$\Omega_{\rm spin}^{B_z^{\rm of}} = \alpha\mu B_z^{\rm of}, \tag{4.14}$$

so that we can neglect the spin-orbit contribution to the matrix element $\delta\Omega$.

On the other hand, the electric field dipole operator $(\hbar\Omega = e\mathbf{E}^{\rm of}.\mathbf{r})$ does not couple the unperturbed states. As Ω is now time reversal symmetric, the contributions of all terms in H_1 but $H_Z^{(2)}$ are suppressed. For the electric field along the rotated $\hat{x}$ axis, the matrix element at the anti-crossing is

$$\Omega_{\rm spin}^{E_x^{\rm of}} = \beta e E_x^{\rm of}\overline{X}. \tag{4.15}$$

Away from the anti-crossing

$$\Omega_{\rm spin}^{E_x^{\rm of}} = -eE_x^{\rm of} h_1^x E_Z \sum_j |\overline{X}_j|^2 \frac{2E_j^x}{(E_j^x)^2 - 4E_Z^2}, \tag{4.16}$$

	definition	unit	expression	$d \ll 1$	$d \gg 1$
$\overline{X}_1$	$\langle\Gamma_2^{10}\|x\|\Gamma_1^{00}\rangle$	l_0	$\frac{d}{\sqrt{1-e^{-2d^2}}}$	$\frac{1}{\sqrt{2}}$	d
$\overline{X}_2$	$\langle\Gamma_2^{31}\|x\|\Gamma_1^{00}\rangle$	l_0	-	$-\frac{3d^2}{4}$	$\frac{1}{\sqrt{2}}$
$\overline{Y}_1$	$\langle\Gamma_4^{11}\|y\|\Gamma_1^{00}\rangle$	l_0	$\frac{1}{\sqrt{2}}$	$\frac{1}{\sqrt{2}}$	$\frac{1}{\sqrt{2}}$
$\overline{XY}$	$\langle\Gamma_3^{21}\|P_xP_y\|\Gamma_1^{00}\rangle$	$\hbar^2 l_0^{-2}$	$-\frac{d}{\sqrt{2}}\frac{e^{-d^2}}{\sqrt{1-e^{-2d^2}}}$	$-\frac{1}{2}$	$-\frac{d}{\sqrt{2}}e^{-d^2}$
E_1^x	$E_2^{10}-E_1^{00}$	E_0	$2T^{(0)}/E_0$	1	de^{-d^2}
E_2^x	$E_2^{31}-E_1^{00}$	E_0	-	3	1
E_1^y	$E_4^{11}-E_1^{00}$	E_0	1	1	1

Table 4.2: Analytical approximations for the dipole matrix elements and energy differences. For each quantity the definition, unit, expression, and limits for small and large interdot distances are given. In some cases the expression is too lengthy and only the asymptotics are given. The expression for $T^{(0)}$ is given in Eq. 3.23.

where $E_Z = \mu B_{||}$. The spatial symmetry (here x) of the dipole operator selects only eigenfunctions of symmetry x in the sum. Only $H_Z^{(2)}$, Eq. (2.47), contains a term of x symmetry, proportional to h_1^x. In the above sum each state j (with energy $E_1^{00}+E_j^x$) contributes proportionally to its dipole matrix element $\overline{X}_j$. To get the analytical result reasonably close to numerics one needs to include the two lowest eigenfunctions in the sum in Eq.(4.16).

If the electric field is along the rotated $\hat{y}$ axis, the anti-crossing does not influence the overlap, since y dipole operator of the electric field does not couple the ground and anti-crossing state. Then, an analogous expression to Eq. (4.16) holds at (up to a factor α multiplying some terms in the sum) or away from the anti-crossing:

$$\Omega_{\rm spin}^{E_y^{\rm of}} = -eE_y^{\rm of} h_1^y E_Z \sum_j |\overline{Y}_j|^2 \frac{2E_j^y}{(E_j^y)^2 - 4E_Z^2}. \tag{4.17}$$

Here it is enough to include just the lowest eigenfunction of y symmetry in the sum. The dipole elements and energy differences, computed by approximating the unperturbed functions Γ by LCSDO, Eq. (2.21), are summarized in Tab. 4.2.

Fully numerical results for the matrix elements as a function of the magnetic field are shown in Fig. 4.3a. The matrix element of the magnetic field is constant, up to a narrow region of suppression due to α, since it depends only on the strength of the oscillating magnetic field, Eq. (4.14). The matrix elements of the electric field [Eqs. (4.16)-(4.17)] are proportional to the Zeeman energy E_Z – the spin resonance is more sensitive to electrical disturbance as the magnetic field grows, while at zero magnetic field the electric field is ineffective. At the anti-crossing, $\Omega_{\rm spin}^{E_x^{\rm of}}$ is strongly enhanced (by two orders of magnitude) and described by Eq. (4.15), while $\Omega_{\rm spin}^{E_y^{\rm of}}$ develops a small dip similar to $\Omega_{\rm spin}^{B_z^{\rm of}}$.

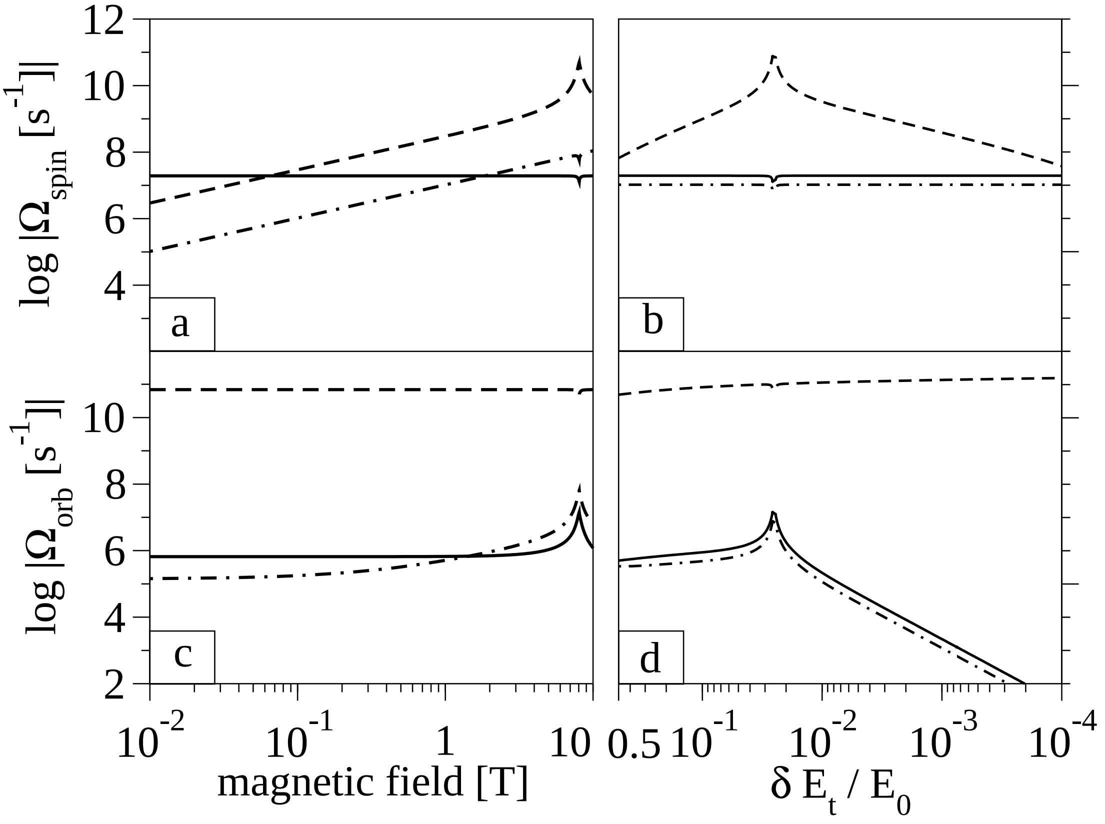

Figure 4.3: Calculated matrix elements between the resonant states due to magnetic and electric oscillating fields. The two upper panels, (a) and (b), show the matrix elements Ω_{spin} for the spin resonance, while the two lower panels show orbital resonance elements Ω_{orb}. On the left, in (a) and (c) the elements are functions of the static magnetic field, with a fixed tunneling energy of 20% of the confinement energy. On the right, in (b) and (d) the elements are functions of the tunneling energy at a fixed magnetic field $B_{||} = 1$ T. The dots are oriented along [100], while the static magnetic field lies along [010].

It can be seen in Fig. 4.3b, where the matrix elements are functions of the tunneling energy, that the spin resonance is much more sensitive to the electric field along the double dots x axis than to a perpendicular field. This difference is strengthened at the anti-crossing. Only in the truly single dot case ($d = 0$ or $d = \infty$), the electric field influence is isotropic. We can also conclude from the single dot values that the matrix elements of a magnetic field of 1 mT and electric field of 10^3 V/m are comparable in magnitude in the static magnetic field of order of Tesla. This means that in the experiment,[105] where no electrically induced signal was observed, the electric field is likely considerably lower than the estimated value of 10^4 V/m.

Similarly to the spin relaxation rates,[123] the matrix elements of the resonant fields are highly anisotropic. The possible control over the resonance is demonstrated in Fig. 4.4a, where the matrix elements Ω are shown as a function of the orientation of the static magnetic field. The magnetic field matrix element is independent on γ, as follows from Eq. (4.14). The electric field matrix element is anisotropic, with the dependence given by the effective spin-orbit couplings h_1^x and h_1^y. By proper orienting the static magnetic field it is thus possible to turn off the contribution due to the electric field along a certain direction. In particular, the electric field along $\hat{x}$ is not effective ($h_1^x = 0$) at $\gamma = \arctan(l_D/l_{BR}) \approx 38^\circ$. The contribution due to the electric field along $\hat{y}$ vanishes at $\gamma = \arctan(l_{BR}/l_D) \approx 58^\circ$, since here $h_1^y = 0$. These conditions were obtained from Eqs. (4.10) and (4.11) by putting $\delta = 0$ (the dots oriented along [100]). Different orientation of the dots changes the conditions for the effective spin-orbit couplings to be zero. For example, in Fig. 4.4b, the dots are oriented along [110], that is $\delta = 45^\circ$ and the effective couplings h_1^x and h_1^y are zero at $\gamma = 45^\circ$ and 135°, respectively, independent on the spin-orbit parameters. If the electric field points along a general direction, it is still possible to turn off the contribution to the overlap by properly orienting the magnetic field. However, in a general case the desired position of the magnetic field is defined not only by the effective couplings h_1^x and h_1^y, but by all terms in Eqs. (4.16)-(4.17).

As shown in Chapter 3, in the easy passage configuration, defined by $h_1^x = 0$, the spin relaxation time does not suffer a drastic suppression due to the anti-crossing. In addition to that, the spin resonance is insensitive to otherwise most effective electric field component – along $\hat{x}$. Such electric fields are inevitably present if the spin qubit is manipulated by an on-chip generated magnetic field.[105] On the other hand, on-chip manipulations seem inevitable in a scalable system, where it must be possible to address the qubits selectively. The easy passage configuration thus protects the spin against the electric field and provides a stable Rabi frequency over a wide range of parameters values.

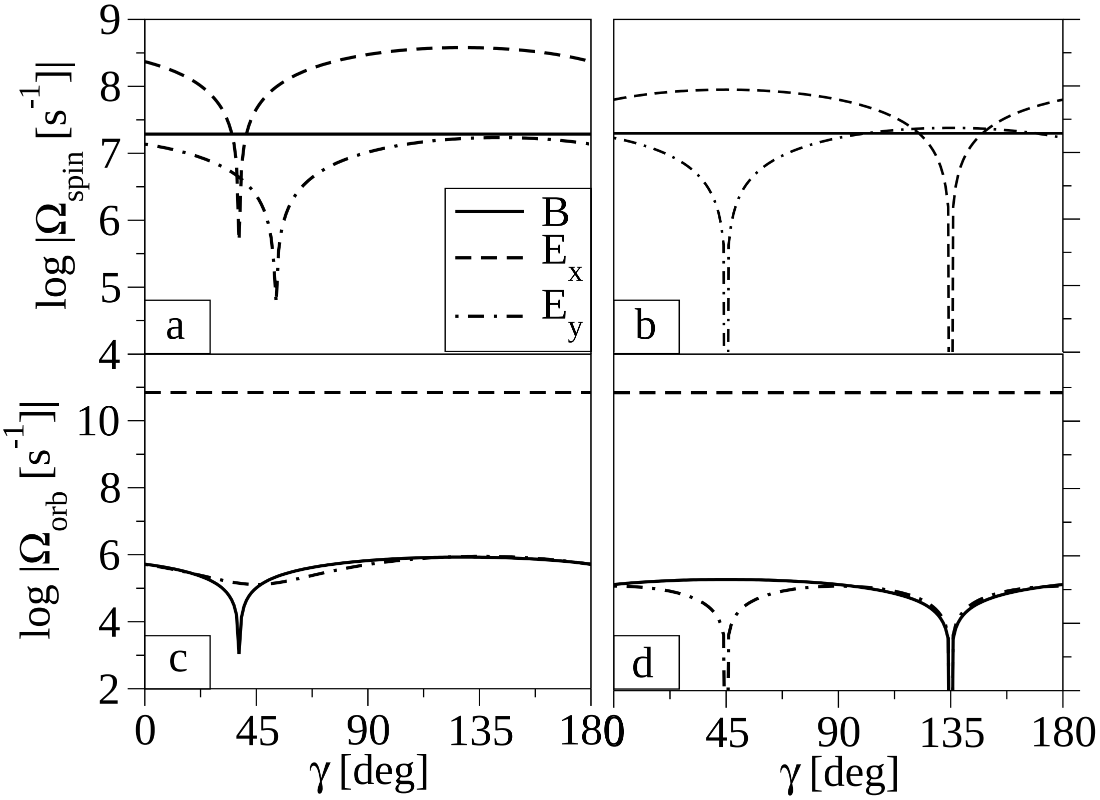

Figure 4.4: Calculated matrix elements for the spin [upper two panels (a) and (b)] and the orbital [lower two panels (c) and (d)] resonance due to oscillating magnetic and electric fields as functions of γ, the orientation of the static magnetic field, $B_{||} = 1$ T. The tunneling energy is 20% of the confinement energy. On the left, in (a) and (c) the dots are oriented along [100], that is $\delta = 0$. On the right, in (b) and (d) the dots are oriented along [110], $\delta = 45°$.

4.6 Matrix elements for the orbital resonance

In the orbital resonance the resonant states are $\overline{\Gamma}^{00}_{1\uparrow}$ and $\overline{\Gamma}^{00}_{2\uparrow}$. A similar suppression as in Eq. (4.13) holds for the overlap between states with different spatial indexes, if the operator O acts only in the spin subspace. This suppression again favors the contribution from $H_Z^{(2)}$ comparing to the rest of H_1. If the anti-crossing dominates, the overlap due to $B_z^{\rm of}$ is $\Omega_{\rm orb}^{B_z^{\rm of}} = -\beta\mu B_z^{\rm of}$, while away from the anti-crossing

$$\Omega_{\rm orb}^{B_z^{\rm of}} = \mu B_z^{\rm of} h_1^x \overline{X}_1 \frac{(E_1^x)^2}{(E_1^x)^2 - 4E_Z^2}. \tag{4.18}$$

Contrary to the case of electrically induced spin resonance, the oscillating magnetic field can induce transitions also at zero static magnetic field, as seen in Fig. 4.3c. The electric field along $\hat{x}$ is most efficient for the orbital resonance, $\Omega_{\rm orb}^{E_x^{\rm of}} = eE_x^{\rm of}\overline{X}_1$, since it couples unperturbed states directly.

For the chosen parameters, the magnetic field is approximately as effective as the electric field along $\hat{y}$, since the linear spin-orbit terms do not contribute to the electric field matrix element in the first order. Here, for a non-zero overlap between $\overline{\Gamma}^{00}_{1\uparrow}$ and $\overline{\Gamma}^{00}_{2\uparrow}$, a spin diagonal operator with spatial symmetry xy is needed. The only such in H_1 is the term originating in the first term of $H_{D3}^{(2)}$, Eq. (2.48). After the rotation of the coordinate system this term is $-(2\gamma_c/\hbar^2 l_{BR})\cos(2\delta)P_xP_y$, leading to the overlap

$$\Omega_{\rm orb}^{E_y^{\rm of}} = -2eE_y^{\rm of}\overline{Y}_1 \frac{\gamma_c}{\hbar^2 l_{BR}} \cos 2\delta \overline{XY} \frac{2E_1^x}{(E_1^y)^2 - (E_1^x)^2}. \tag{4.19}$$

In small magnetic fields ($\lesssim$ 1 T) this contribution dominates the overlap comparing to contributions from other parts in H_1, such as $H_Z^{(2)}$, contributing in the second order. Note that there is no term with appropriate symmetry (spin diagonal, spatially xy) in H_1 coming from a mixture of H_D and H_{D3}, making $\Omega_{\rm orb}^{E_y^{\rm of}}$ a specific effect due to the mixed cubic Dresselhaus and Bychkov-Rashba interactions.

The dependence of the matrix elements Ω on the static magnetic field orientation γ is shown in Fig. 4.4c and d. The magnetic field matrix element is proportional to h_1^x, see Eq. (4.18). The direct coupling through the electric field along $\hat{x}$ is also independent on γ. The matrix element of the electric field along $\hat{y}$, as given in Eq. (4.19), is independent on γ and can not be put to zero by changing the magnetic field orientation – as seen in Fig. 4.4c. However, there is some dependence to be seen and the dependence is striking for a different dots' orientation. The reason is that Eq. (4.19) is the dominant contribution to the matrix element only up to a certain value of the static magnetic field – in higher fields the second order contribution from H_1 will dominate. Since there is already a visible dependence in Fig. 4.4c, we can estimate the crossover magnetic field to be 1 Tesla, for our parameters. In Fig. 4.4d, the contribution of Eq. (4.19) is zero exactly, since $\delta = 45°$. Therefore the second order contribution to the matrix element coming from $H_Z^{(2)}$ is seen. The possible dependence of the matrix element on γ can decide whether the matrix element is induced by linear spin-orbit terms (depends on γ), or the mixed cubic-linear terms (does not depend on γ). This could be used as a detection for the presence of the cubic Dresselhaus term. Unless the electric field is positioned exactly along $\hat{y}$, no oscillating magnetic field influence or anisotropy can be observed due to high effectiveness of the electric field along $\hat{x}$.

4.7 Conclusions

We have studied electrically and magnetically induced spin and orbital resonance of a single electron confined in single and coupled lateral quantum dots. We have shown how the decoherence and relaxation rates can be computed from the excited population and Rabi frequency (these two in turn can be obtained from a steady state current measurement by changing the coupling to leads). We have also shown that the *spin* resonance in an *electric* oscillating field, induced by the spin-orbit interactions,[134, 74] can in practical situations exceed the resonance induced by the magnetic field. We have shown that the spin-orbit interactions allow *orbital* resonance in an oscillating *magnetic* field. We have quantified the spin-orbit contributions to the resonance, stemming from the effective spin-orbit Hamiltonian. The time reversal symmetry and spatial symmetry of the potential determine which part of the effective Hamiltonian is relevant. The electron resonance is most sensitive to the electric field along the coupled dots' axis. However, this component of the electric field is not effective in spin resonance in the easy passage configuration, which is achieved by properly orienting the static magnetic field. The easy passage thus provides not only long spin relaxation time, but also stability against electric field disturbances, making it a suitable arrangement for spin qubit realization.

Chapter 5

Conclusions

We have performed numerical and analytical study of single electron states localized in a semiconductor quantum dot created by gate and heterostructure confinement. We included phonons into our consideration, leading to the orbital and spin relaxation. We also allowed for the presence of resonant electric and magnetic fields and studied the effectiveness of these fields in inducing Rabi oscillations. We concentrated on revealing the role of the spin-orbit interactions, trying to provide means of control over electron states. Important part of our investigations was to look at spin anti-crossings which have profound consequences on spin properties of the system.

In the first part we studied the spin-orbit interactions influence on the energy spectrum of single and double dot states both in zero and finite perpendicular magnetic field. Among our main results here is the finding that the tunneling energy in double quantum dots is influenced by spin-orbit interactions much less than expected. Nevertheless, spin-orbit interactions induce small difference in tunneling energies for spin up and down electrons, what we proposed to use in a spin to charge conversion scheme. The small influence of the spin-orbit on the energy follows from the symmetry of the potential and the spin-orbit interactions and we explained it by deriving an effective spin-orbit Hamiltonian. On the other hand, we found that a double dot, compared to a single dot, is much more influenced by spin hot spots. It is because the anti-crossing can occur at any magnetic field, and all spin-orbit terms are effective in inducing the anti-crossing. In single dots the field where the anti-crossing occurs is fixed by the dot dimensions and some of the spin-orbit terms are not effective in inducing the anti-crossing. Concluding from the first part, having small impact, spin-orbit interactions are not effective in controlling the double dot spectrum, but their influence on the wavefunctions is more profound than in single dots.

The second part was dedicated to quantifying the spin and orbital relaxation rates due to acoustic phonons, entering through piezoelectric and deformation potentials. We provided a comprehensive study of the spin and orbital relaxation rates in single and double dots in both in-plane and perpendicular magnetic fields. The most interesting result is the anisotropy of the spin relaxation rate, which reflects the anisotropy of the Dresselhaus spin-orbit interactions. This was already known from the single dot case, however, we found that there is an additional anisotropy in double dots, originating in anti-crossing enhancement of the spin relaxation rate. We found that the anti-crossing actually dominates the spin relaxation, making the spin relaxation time much shorter in the useful parameters' range. Fortunately, from the point of long spin relaxation times, we found that there are particular configurations of the quantum dot and a magnetic field where such enhancement of the spin relaxation rate is not present. We have called such configurations easy passages and specified analytically the parameters values for them for various heterostructure growth directions. Using easy passage we proposed a scheme for resolving the couplings of the linear spin-orbit terms. Even highly desirable, experimental quantification of these couplings has not been achieved in quantum dots yet.

In the third part we studied electrically and magnetically induced Rabi oscillations of single electron charge and spin qubits. We showed how decoherence and relaxation time can be calculated from Rabi oscillations characteristics, which, in turn, can be obtained in a steady current measurement. Most important result is that the anisotropy, and the underlying symmetry, is crucial also here. It is namely possible to control the effectiveness of electric and magnetic fields in inducing Rabi oscillations by changing the orientation of the static magnetic field, meaning going into/out of the easy passage configuration.

The spin-orbit interactions thus proved to provide a possible efficient mean for spin qubit manipulation – our results show how to control the spin relaxation rate and Rabi frequency exploiting easy passages. These findings provide guideline for manufacturing experimental samples with much improved double dot spin qubit characteristics from the point of interest of quantum computation.

Possible extensions of the work

We identify three main areas where further studies, taking into account results presented in this work, are highly desirable.

In Chapter 4 we already touched the possibility that the dot is open and a current is allowed to flow through the dot. The number of electrons in the dot is then not constant and the electron life time in the dot is finite. Eigenenergies become blurred, with a certain width, around their sharp values from the case of a closed dot. The nearby leads provide an additional relaxation and decoherence channel. However, compared to phonons, the theoretical description is much more complicated, since the influence of the leads probably depends strongly on the system details.

Closely connected to couplings to the leads is the possibility of a finite bias applied across the dot, meaning a dot in a nonlinear regime. It is a situation almost always encountered in experiments, in which a current flows through the dot. Considering our results, the degradation of the potential symmetry will critically influence easy passages, which exist due to the potential symmetry. It is important to find out to what degree are easy passages useful in realistic biases.

From the point of view of a possible exploitation of double dots as qubits in quantum information processing, the most important extension of this work is to repeat the analysis for the two electron case. Recent experiments provide data for comparison for both energy spectrum and spin relaxation time. We think that easy passages will occur also in the two electron case, if the confining potential stays symmetric. This problem is currently under our investigation.

Chapter 6

Appendices

.1 Transient current occupation

.1.1 Probe pulse

Here we derive Eq. (3.3) from Eq. (3.2). We introduce the missing charge in the ground state, $x = 1 - g$, which transforms Eq. (3.2) into a homogeneous system:

$$\begin{aligned} \dot{e} &= \Gamma_{LE}(x - e) - (\Gamma_{RE} + W)e, \\ \dot{x} &= -(\Gamma_{LG} + \Gamma_{RG})(x - e) - We. \end{aligned} \tag{1}$$

Introducing total tunneling rates,

$$\begin{aligned} \Gamma_{TG} &= \Gamma_{LG} + \Gamma_{RG}, \\ \Gamma_{TE} &= \Gamma_{LE} + \Gamma_{RE}, \\ \Gamma_{T} &= \Gamma_{TE} + \Gamma_{TG}, \end{aligned} \tag{2}$$

we express e from the second equation,

$$e(\Gamma_{TG} - W) = \dot{x} + \Gamma_{TG}x. \tag{3}$$

Inserting it into the first one, we get a second order homogeneous equation for x:

$$\frac{\ddot{x} + \Gamma_{TG}\dot{x}}{\Gamma_{TG} - W} = \Gamma_{LE}x - \frac{\Gamma_{TE} + W}{\Gamma_{TG} - W}\left(\dot{x} + \Gamma_{TG}x\right), \tag{4}$$

which we rewrite as

$$\ddot{x} + a\dot{x} + b^2 x = 0, \tag{5}$$

where

$$\begin{aligned} a &= \Gamma_T + W, \\ b^2 &= \Gamma_{TG}(\Gamma_{TE} + W) - \Gamma_{LE}(\Gamma_{TG} - W) = \Gamma_{TG}\Gamma_{RE} + W(\Gamma_T - \Gamma_{RE}). \end{aligned} \tag{6}$$

In further we use that W and Γ_{RE} are much smaller than the total (or left) tunneling rate and express all quantities up to the lowest order in small frequencies ($a \gg b$). The solution of the homogeneous equation is

$$x(t) = Ae^{-\omega_1 t} + Be^{-\omega_2 t}, \tag{7}$$

where the frequencies $\omega_{1,2}$ are given by

$$\begin{aligned}
\omega_{1,2} &= \frac{1}{2}\left(a \pm \sqrt{a^2 - 4b^2}\right) = \frac{a}{2}\left(1 \pm \sqrt{1 - 4\frac{b^2}{a^2}}\right) = \frac{a}{2}\left(1 \pm (1 - 2\frac{b^2}{a^2})\right) + o(\frac{b^2}{a^2}).\\
\omega_2 &= \frac{b^2}{a} \approx \frac{\Gamma_{TG}}{\Gamma_T}\Gamma_{RE} + W \equiv D.\\
\omega_1 &= a - \omega_2 \approx \Gamma_T - \frac{\Gamma_{TG}}{\Gamma_T}\Gamma_{RE},
\end{aligned} \tag{8}$$

The initial condition $e = g = 0$ leads to equations for the coefficients of the linear combination Eq. (7)

$$\left.\begin{aligned} A + B &= 1,\\ A\omega_1 + B\omega_2 &= \Gamma_{TG}, \end{aligned}\right\} \Rightarrow \begin{aligned} &B = 1 - A,\\ &A = \tfrac{\Gamma_{TG} - \omega_2}{\omega_1 - \omega_2} \approx \tfrac{\Gamma_{TG}}{\Gamma_T} + \left(\tfrac{\Gamma_{TG}}{\Gamma_T}\right)^2 \tfrac{\Gamma_{RE}}{\Gamma_T} - \tfrac{W}{\Gamma_T}\tfrac{\Gamma_{TE}}{\Gamma_T}. \end{aligned} \tag{9}$$

Using this result in Eq. (7) we get

$$x(t) \approx \frac{\Gamma_{TG}}{\Gamma_T} e^{-\Gamma_T t} + \frac{\Gamma_{TE}}{\Gamma_T} e^{-Dt}, \tag{10}$$

from where the solution for ground state population $g(t)$ given in Eq. (3.3) follows.

From Eq. (3) follows that the excited state will have the same functional form as Eq. (7) with different coefficients given again by the initial condition of an empty dot:

$$\left.\begin{aligned} A' + B' &= 0,\\ A'\omega_1 + B'\omega_2 &= -\Gamma_{LE}, \end{aligned}\right\} \Rightarrow \begin{aligned} &B' = -A',\\ &-A' = \tfrac{\Gamma_{LE}}{\omega_1 - \omega_2} \approx \tfrac{\Gamma_{LE}}{\Gamma_T}\left(1 + \tfrac{W}{\Gamma_T} + 2\tfrac{\Gamma_{TG}}{\Gamma_T}\tfrac{\Gamma_{RE}}{\Gamma_T}\right). \end{aligned} \tag{11}$$

From here we get

$$e(t) \approx \frac{\Gamma_{LE}}{\Gamma_T}(e^{-\Gamma_T t} + e^{-Dt}), \tag{12}$$

which is, within the leading order in Γ_T^{-1}, equivalent to the solution in Eq. (3.3).

.1.2 Fill&wait pulse

Here Eq. (3.5) are derived from Eq. (3.6). Now the equations are best simplified by introducing the total missing charge on the dot $c = 1 - g - e$.

$$\begin{aligned} \dot{e} &= \Gamma_{TE}c - We,\\ \dot{c} &= -\Gamma_T c, \end{aligned} \tag{13}$$

with initial conditions $e(0) = 0$ and $c(0) = 1$. The second equation gives immediately

$$c(t) = e^{-\Gamma_T t}, \tag{14}$$

From the previous case, Appendix .1.1, the functional form of the excited state population is already known. One of the frequencies is that given by Eq. (14), leading to an ansatz

$$e(t) = A\left(e^{-\omega_2 t} - e^{-\Gamma_T t}\right), \tag{15}$$

where the second frequency and the normalization follows from Eq. (13).

$$\begin{aligned} A\left(-\omega_2 e^{-\omega_2 t} + \Gamma_T e^{-\Gamma_T t}\right) &= \Gamma_{TE} e^{-\Gamma_T t} - WA\left(e^{-\omega_2 t} - e^{-\Gamma_T t}\right), \\ e^{-\omega_2 t}\left(-A\omega_2 + WA\right) &= e^{-\Gamma_T t}\left(-A\Gamma_T + \Gamma_{TE} + WA\right), \end{aligned} \tag{16}$$

giving

$$\begin{aligned} \omega_2 &= W, \\ A &= \frac{\Gamma_{TE}}{\Gamma_T - W} \end{aligned} \tag{17}$$

.2 TRRO – probe pulse

Here we derive explicit formulas for probabilities α and β in Eq. (3.9). We suppose the dot is in fill&wait step, as denoted in Fig. 3.9, leading to the following equations for the populations:

$$\begin{aligned} \dot{e} &= -(\Gamma_T + W)e, \\ \dot{g} &= -\Gamma_S g + We. \end{aligned} \tag{18}$$

Comparing with Eq. (13) the solution follows as:

$$\begin{aligned} e(t) &= e(0)e^{-(\Gamma_T + W)t}, \\ g(t) &= Ae^{-(\Gamma_T + W)t} + Be^{-\Gamma_S t}. \end{aligned} \tag{19}$$

Considering an initial condition of an occupied dot, $e(0) + A + B = 1$, one solves for the ground state population

$$\begin{aligned} &- A(\Gamma_T + W)e^{-(\Gamma_T + W)t} - B\Gamma_S e^{-\Gamma_S t} = \\ &\quad = -\Gamma_S A e^{-(\Gamma_T + W)} t - \Gamma_S B e^{-\Gamma_S t} + We(0)e^{-(\Gamma_T + W)t}, \end{aligned} \tag{20}$$

giving

$$e^{-(\Gamma_T + W)t}\big[A(\Gamma_T + W) - \Gamma_S A + We(0)\big] = 0, \tag{21}$$

with solution

$$\begin{aligned} A &= \frac{W}{\Gamma_S - \Gamma_T - W}, \\ B &= 1 - A - e(0). \end{aligned} \tag{22}$$

If, initially, the excited state is populated, $e(0) = 1$, the time dependence of the two states is

$$\begin{aligned} e(t) &= e^{-(\Gamma_T + W)t}, \\ g(t) &= \frac{W}{\Gamma_T - \Gamma_S + W}\left(e^{-\Gamma_S t} - e^{-(\Gamma_T + W)t}\right). \end{aligned} \tag{23}$$

A tunneling has not been observed, with an electron in the excited state initially, with a probability

$$\beta(t) = e(t) + g(t) = \frac{1}{\Gamma_T + W - \Gamma_S}\left(We^{-\Gamma_S t} + (\Gamma_T - \Gamma_S)e^{-(\Gamma_T + W)t}\right), \tag{24}$$

On the other hand, if the ground state is populated in the beginning, $g(0) = 1$,

$$\begin{aligned} e(t) &= 0, \\ g(t) &= e^{-\Gamma_S t}. \end{aligned} \tag{25}$$

A tunneling has been observed, even the electron was in the ground state, with a probability

$$\alpha(t) = 1 - g(t) - e(t) = 1 - e^{-\Gamma_S t}. \tag{26}$$

The visibility, for given tunneling rates, is

$$v(t) = 1 - \alpha(t) - \beta(t), \tag{27}$$

and can be optimized as a function of the duration of the probe step.

Bibliography

[1] V. A. Abalmassov and F. Marquardt. Electron-nuclei spin relaxation through phonon-assisted hyperfine interaction in a quantum dot. *Phys. Rev. B*, 70:75313, 2004.

[2] Elihu Abrahams. Donor electron spin relaxation in silicon. *Phys. Rev.*, 107:491, 1957.

[3] A. M. Alcalde, O. O. Diniz Neto, and G. E. Marques. Spin-flip relaxation due to phonon macroscopic deformation potential in quantum dots. *Microel. J.*, 36:1034, 2005.

[4] A. M. Alcalde, Qu Fanayo, and G. E. Marques. Electron-phonon induced spin relaxation in InAs quantum dots. *Physica E*, 20:228, 2004.

[5] I. L. Aleiner and Vladimir I. Faľko. Spin-orbit coupling effects on quantum transport in lateral semiconductor dots. *Phys. Rev. Lett.*, 87(25):256801, 2001.

[6] S. Amasha, K. MacLean, Iuliana Radu, D. M. Zumbuhl, M. A. Kastner, M. P. Hanson, and A. C. Gossard. Measurements of the spin relaxation rate at low magnetic fields in a quantum dot. *cond-mat/0607110*, 2006.

[7] N. W. Ashcroft and N. D. Mermin. *Solid State Physics.* Saunders Colledge, Philadelphia, 1976.

[8] S. Ashhab, J. R. Johansson, and Franco Nori. Decoherence and Rabi oscillations in a qubit coupled to a quantum two-level system. *cond-mat/0604475*, unpublished.

[9] N. S. Averkiev and L. E. Golub. Giant spin relaxation anisotropy in zinc-blende heterostructures. *Phys. Rev. B*, 60:15582, 1999.

[10] N. S. Averkiev, L. E. Golub, A. S. Gurevich, V. P. Evtikhiev, V. P. Kochereshko, A. V. Platonov, A. S. Shkolnik, and Yu. P. Efimov. Spin-relaxation anisotropy in asymmetrical (001) AlGaAs quantum wells from Hanle-effect measurements: Relative strengths of Rashba and Dresselhaus spin-orbit coupling. *Phys. Rev. B*, 74:33305, 2006.

[11] S. C. Badescu and T. L. Reinecke. Mixing of two-electron spin states in a semiconductor quantum dot. *cond-mat/0610405*, unpublished.

[12] Anjana Bagga, Pekka Pietilainen, and Tapash Chakraborty. Spin hot spots in vertically-coupled few-electron quantum dots. *cond-mat/0601390*, 2006.

[13] G. Bastard. *Wave Mechanics Applied to Semiconductor Heterostructures.* Les Editions de Physique, les Ulis, 1988.

[14] Andrea Bertoni, Massimo Rontani, Guido Goldoni, and Elisa Molinari. Reduced electron relaxation rate in multielectron quantum dots. *Phys. Rev. Lett.*, 95:66806, 2005.

[15] Karl Blum. *Density matrix theory and applications.* Plenum Press, New York, 1996.

[16] Massoud Borhani, Vitaly N. Golovach, and Daniel Loss. Spin decay in a quantum dot coupled to a quantum point contact. *Phys. Rev. B*, 73:155311, 2006.

[17] T. Brandes, R. Aguado, and G. Platero. Charge transport through open driven two-level systems with dissipation. *Phys. Rev. B*, 69:205326, 2004.

[18] M. Braun and U. Rössler. Magneto-optic transitions and non-parabolicity parameters in the conduction band of semiconductors. *J. Phys. C*, 18:3365, 1985.

[19] C. Bruder and H. Schoeller. Charging effects in ultrasmall quantum dots in the presence of time-varing fields. *Phys. Rev. Lett.*, 72:1076, 1994.

[20] Ph. Brune, C. Bruder, and H. Schoeller. Photon-assisted transport through ultrasmall quantum dots: Influence of intradot transitions. *Phys. Rev. B*, 56:4730, 1997.

[21] Denis V. Bulaev and Daniel Loss. Spin relaxation and anticrossing in quantum dots: Rashba versus Dresselhaus spin orbit coupling. *Phys. Rev. B*, 71:205324, 2005.

[22] E. N. Bulgakov and A. F. Sadreev. Spin polarization in quantum dots by radiation field with circular polarization. *JETP Letters*, 73(10):505, 2001.

[23] Yu. A. Bychkov and E. I. Rashba. Oscillatory effects and the magnetic susceptibility of carriers in inversion layers. *J. Phys. C*, 17:6039–6045, 1984.

[24] Carlos Calero, E. M. Chudnovsky, and D. A. Garanin. Field dependence of the electron spin relaxation in quantum dots. *Phys. Rev. Lett.*, 95:166603, 2005.

[25] M. Cardona, N. E. Christensen, and G. Fasol. Relativistic band structure and spin-orbit splitting of zinc-blende-type semiconductors. *Phys. Rev. B*, 38:1806, 1988.

[26] X. Cartoixá, L.-W. Wang, D.Z.-Y. Ting, and Y.-C. Chang. Higher-order contributions to Rashba and Dresselhaus effects. *Phys. Rev. B*, 73:205341, 2006.

[27] A. V. Chaplik and L. I. Magarill. Bound states in a two-dimensional short range potential induced by the spin-orbit interaction. *Phys. Rev. Lett.*, 94:126402, 2006.

[28] Juan I. Climente, Andrea Bertoni, Guido Goldoni, and Elisa Molinari. Phonon-induced electron relaxation in weakly confined single and coupled quantum dots. *Phys. Rev. B*, 74:35313, 2006.

[29] Juan I. Climente, Andrea Bertoni, Guido Goldoni, Massimo Rontani, and Elisa Molinari. Triplet-singlet spin relaxation in quantum dots with spin-orbit coupling. *cond-mat/0610509*, unpublished.

[30] W. A. Coish and Daniel Loss. Singlet-triplet decoherence due to neclear spins in a double quantum dot. *Phys. Rev. B*, 72:125337, 2005.

[31] T. Darnhofer and U. Rössler. Effects of band structure and spin in quantum dots. *Phys. Rev. B*, 47(23):16020, 1993.

[32] C. G. Darwin. *Proc. Cambridge Philos. Soc.*, 27:86, 1931.

[33] E. A. de Andrada e Silva and G. C. La Rocca. Rashba splitting in semiconductor quantum wires. *Phys. Rev. B*, 67:165318, 2003.

[34] Rogerio de Sousa and S. Das Sarma. Gate control of spin dynamics in III-V semiconductor quantum dots. *Phys. Rev B*, 68:155330, 2003.

[35] S. Michaelis de Vasconcellos, S. Stufler, S.-A. Wegner, P. Ester, A. Zrenner, and M. Bichler. Quantum interferences of a single quantum dot in the case of detuning. *Phys. Rev. B*, 74:81304(R), 2006.

[36] S. Debald, T. Brandes, and B. Kramer. Control of dephasing and phonon emission in coupled quantum dots. *Phys. Rev. B*, 66:41301(R), 2002.

[37] Stefan Debald and Clive Emary. Spin-orbit-driven coherent oscillations in a few-electron quantum dot. *Phys. Rev. Lett.*, 94:226803, 2005.

[38] C. Deng and X. Hu. Nuclear spin diffusion in quantum dots: Effects of inhomogeneous hyperfine interaction. *Phys. Rev. B*, 72:165333, 2005.

[39] C. Deng and X. Hu. Analytical solution of electron spin decoherence through hyperfine interaction in a quantum dot. *Phys. Rev. B*, 73:241303(R), 2006.

[40] C. F. Destefani and Sergio E. Ulloa. Anisotropic electron g factor in quantum dots with spin-orbit interaction. *Phys. Rev. B*, 71:161303(R), 2005.

[41] C. F. Destefani and Sergio E. Ulloa. Oscillatory spin relaxation rates in quantum dots. *Phys. Rev. B*, 72:115326, 2005.

[42] C. F. Destefani, Sergio E. Ulloa, and G. E. Marques. Spin-orbit and electronic interactions in narrow-gap quantum dots. *Phys. Rev. B*, 70:205315, 2004.

[43] C. F. Destefani, Sergio E. Ulloa, and G. E. Marques. Spin-orbit coupling and intrinsic spin mixing in quantum dots. *Phys. Rev. B*, 69:125302, 2004.

[44] I. Djuric and C. P. Search. Spin current and shot noise from a quantum dot coupled to a quantized cavity field. *Phys. Rev. B*, 74:115327, 2006.

[45] V. V. Dobrovitski, J. M. Taylor, and M. D. Lukin. Long-lived memory for electronic spin in a quantum dot: Numerical analysis. *Phys. Rev. B*, 73:245318, 2006.

[46] Bing Dong, H. L. Cui, and X. L. Lei. Pumped spin-current and shot-noise spectra of a single quantum dot. *Phys. Rev. Lett.*, 94:66601, 2005.

[47] G. Dresselhaus. Spin orbit coupling effects in zinc blende structures. *Phys. Rev.*, 100:580–586, 1955.

[48] C. Durkan and M. E. Welland. Electronic spin detection in molecules using scanning-tunneling-microscopy-assisted electron-spin resonance. *Appl. Phys. Lett.*, 80:458, 2002.

[49] M.I. Dyakonov and V.Y. Kachorovskii. Spin relaxation of two-dimensional electrons in noncentrosymmetric semiconductors. *Fiz. Tekh. Poluprovodn.(S-Peterburg)*, 20:178–181, 1986.

[50] B. Eble, O. Krebs, A. Lematre, K. Kowalik, A. Kudelski, P. Voisin, B. Urbaszek, X. Marie, and T. Amand. Dynamic nuclear polarization of a single charge-tunable InAs-GaAs quantum dot. *Phys. Rev. B*, 74:81306(R), 2006.

[51] J. M. Elzerman, R. Hanson, L. H. Willem van Beveren, B. Witkamp, L. M. K. Vandersypen, and L. P. Kouwenhoven. Single-shot read-out of an individual electron spin in a quantum dot. *Nature*, 430:431, 2004.

[52] J. M. Elzerman, R. Hanson, L. H. Willems van Beveren, B. Witkamp, L. M. K. Vandersypen, and L. P. Kouwenhoven. Single-shot read-out of an individual electron spin in a quantum dot. *Nature*, 430:431, 2002.

[53] H. Engel and D. Loss. Fermionic bell-state analyzer for spin qubits. *Science*, 309:586, 2005.

[54] Hans-Andreas Engel, Vitaly N. Golovach, Daniel Loss, L. M. K. Vandersypen, J. M. Elzerman, R. Hanson, and L. P. Kouwenhoven. Measurement efficiency and n-shot readout of spin qubits. *Phys. Rev. Lett.*, 93(10):106804, 2004.

[55] Hans-Andreas Engel and Daniel Loss. Single-spin dynamics and decoherence in a quantum dot via charge transport. *Phys. Rev. B*, 65:195321, 2002.

[56] Hans-Angreas Engel and Daniel Loss. Detection of single spin decoherence in a quantum dot via charge currents. *Phys. Rev. Lett.*, 86:4648, 2001.

[57] G. Engels, J. Lange, Th. Schäpers, and H. Lüth. Experimental and theoretical approach to spin splitting in modulation-doped InGaAs/InP quantum wells for B=0. *Phys. Rev. B*, 55:1958(R), 1997.

[58] Sigurdur I. Erlingsson and Yuli V. Nazarov. Hyperfine-mediated transitions between a Zeeman split doublet in GaAs quantum dots: The role of internal field. *Phys. Rev. B*, 66:155327, 2002.

[59] Sigurdur I. Erlingsson, Yuli V. Nazarov, and Vladimir I. Faľko. Nucleus-mediated spin-flip transitions in GaAs quantum dots. *Phys. Rev. B*, 64:195306, 2001.

[60] J. Fabian and S. Das Sarma. Spin relaxation of conduction electrons in polyvalent metals: theory and realistic calculation. *Phys. Rev. Lett.*, 81:5624, 1998.

[61] J. Fabian and S. Das Sarma. Phonon-induced spin relaxation of conduction electrons in aluminum. *Phys. Rev. Lett.*, 83:1211, 1999.

[62] V. I. Faľko, B. L. Altshuler, and O. Tsyplyatyev. Anisotropy of spin splitting and spin relaxation in lateral quantum dots. *Phys. Rev. Lett.*, 95:076603, 2005.

[63] L. Fedichkin and A. Fedorov. Decoherence rate of semiconductor charge qubit coupled to acoustic phonon reservoir. *Phys. Rev. A*, 69:032311, 2004.

[64] A. V. Fedorov, A. V. Baranov, I. D. Rukhlenko, and Y. Masumoto. New many-body mechanism of intraband carrier relaxation in quantum dots embedded in doped heterostructures. *Sol. St. Comm.*, 128:219, 2003.

[65] Marian Florescu, Sergei Dickman, Mariusz Ciorga, Andy Sachrajda, and Pawel Hawrylak. Spin-orbit interaction and spin relaxation in a lateral quantum dot. *Physica E*, 22:414, 2004.

[66] Marian Florescu and Pawel Hawrylak. Spin relaxation in lateral quantum dots: Effects of spin-orbit interaction. *Phys. Rev. B*, 73:045304, 2006.

[67] Vladimir Fock. *Z. Phys.*, 47:446, 1928.

[68] David M. Frenkel. Spin relaxation in GaAs-AlGaAs heterostructures in high magnetic fields. *Phys. Rev. B*, 43:14228, 1991.

[69] Toshimasa Fujisawa, David Guy Austing, Yasuhiro Tokura, Yoshiro Hirayama, and Seigo Tarucha. Allowed and forbidden transitions in artificial hydrogen and helium atoms. *Nature*, 419:278, 2002.

[70] Toshimasa Fujisawa, Yasuhiro Tokura, David G. Austing, Yoshiro Hirayama, and Seigo Tarucha. Spin-dependent energy relaxation inside a quantum dot. *Physica B*, 314:224, 2002.

[71] Toshimasa Fujisawa, Yasuhiro Tokura, and Yoshiro Hirayama. Transient current spectroscopy of a quantum dot in the coulomb blockade regime. *Phys. Rev. B*, 63:081304(R), 2001.

[72] Y. M. Galperin, B. L. Altshuler, J. Bergli, and D. V. Shantsev. Non-gaussian low-frequency noise as a source of qubit decoherence. *Phys. Rev. Lett.*, 96:97009, 2006.

[73] S.D. Ganichev, V. V. Beĺkov, L. E. Golub, E. L. Ivchenko, Petra Schneider, S. Giglberger, J. Eroms, J. De Boeck, G. Borghs, W. Wegscheider, D. Weiss, and W. Prettl. Experimental separation of Rashba and Dresselhaus spin splittings in semiconductor quantum wells. *Phys. Rev. Lett.*, 92(25):256601, 2004.

[74] Vitaly N. Golovach, Massoud Borhani, and Daniel Loss. Electric-dipole-induced spin resonance in quantum dots. *Phys. Rev. B*, 74:165319, 2006.

[75] Vitaly N. Golovach, Alexander Khaetskii, and Daniel Loss. Phonon-induced decay of the electron spin in quantum dots. *Phys. Rev. Let.*, 93(1):16601, 2004.

[76] A. D. Greentree, A. R. Hamilton, L. C. L. Hollenberg, and R. G. Clark. Electrical readout of a spin qubit without double occupancy. *Phys. Rev. B*, 71:113310, 2005.

[77] Anna Grodecka, Lucjan Jacak, Pawel Machnikowski, and Katarzyna Roszak. Phonon impact on the coherent control of quantum states in semiconductor quantum dots. *cond-mat/0404364*, 2004.

[78] A. Gruber, A. Dräbenstedt, C. Tietz, L. Fleury, J. Wrachtrup, and C. von Borczyskowski. Scanning confocal optical microscopy and magnetic resonance on single defect centers. *Science*, 276:2012, 1997.

[79] Dirk Grundler. Large Rashba splitting in InAs quantum wells due to electron wave function penetration into the barrier layers. *Phys. Rev. Lett.*, 84:6074, 2000.

[80] O. Gywat, F. Meier, D. Loss, and D. D. Awschalom. Dynamics of coupled qubits interacting with an off-resonant cavity. *Phys. Rev. B*, 73:125336, 2006.

[81] R. Hanson, L. H. Willems van Beveren, I. T. Vink, J. M. Elzerman, and L. M. K. Vandersypen. Single-shot readout of electron spin states in a quantum dot using spin-dependent tunnel rates. *Phys. Rev. Lett.*, 94:196802, 2005.

[82] R. Hanson, B. Witkamp, L. M. K. Vandersypen, L. H. Willems van Beveren, J. M. Elzerman, and J. P. Kouwenhoven. Zeeman energy and spin relaxation in a one-electron quantum dot. *Phys. Rev. Lett.*, 91(9):196802, 2003.

[83] T. Hayashi, T. Fujisawa, H. D. Cheong, Y. H. Joeong, and Y. Hirayama. Coherent manipulation of electronic states in a double quantum dot. *Phys. Rev. Lett.*, 91(22):226804, 2003.

[84] J. P. Heida, B. J. van Wees, J. J. Kuipers, T. M. Klapwijk, and G. Borghs. Spin-orbit interaction in a two-dimensional electron gas in a InAs/AlSb quantum well with gate-controlled electron density. *Phys. Rev. B*, 57:11911, 1998.

[85] Can-Ming Hu, Junsaku Nitta, Tatsushi Akazaki, Hideaki Takayanagi, Jiro Osaka, P. Pfeffer, and W. Zawadzki. Zero-field spin splitting in an inverted InGaAs/InAlAs heterostructure: Band nonparabolicity influence and the subband dependence. *Phys. Rev. B*, 60:7736, 1999.

[86] Xuedong Hu and S. Das Sarma. Charge-fluctuation-induced dephasing of exchange-coupled spin qubits. *Phys. Rev. Lett.*, 96:100501, 2006.

[87] A. K. Hüttel, J. Weber, A. W. Holleitner, D. Weinmann, K. Eberl, and R. H. Blick. Nuclear spin relaxation probed by a single quantum dot. *Phys. Rev. B*, 69:73302, 2004.

[88] R. Ionicioiu and A. E. Popescu. Single-spin measurement using spin?orbital entanglement. *New J. Physics*, 7:120, 2005.

[89] F. Jelezko, T. Gaebel, I. Popa, A. Gruber, and J. Wrachtrup. Observation of coherent oscillations in a single electron spin. *Phys. Rev. Lett.*, 92:76401, 2004.

[90] F. Jelezko, I. Popa, A. Gruber, C. Tietz, J. Wrachtrup, A. Nizovtsev, and S. Kilin. Single spin states in a defect center resolved by optical spectroscopy. *Appl. Phys. Lett.*, 81:2160, 2002.

[91] J. H. Jiang, M. Q. Weng, and M. W. Wu. Intense terahertz laser fields on a quantum dot with Rashba spin-orbit coupling. *J. Appl. Phys.*, 100:63709, 2006.

[92] A. C. Johnson, J. R. Petta, J. M. Taylor, A. Yacobi, M. D. Lukin, C. M. Marcus, M. P. Hanson, and A. C. Gossard. Triplet-singlet spin relaxation via nuclei in a double quantum dot. *Nature*, 435:925, 2005.

[93] J. Kainz, U. Rössler, and R. Winkler. Anisotropic spin-splitting and spin-relaxation in asymetric zinc blende semiconductor quantum structures. *Phys. Rev. B*, 68:075322, 2003.

[94] Y. Kato, R. C. Myers, D. C. Driscoll, A. C. Gossard, J. Levy, and D. D. Awschalom. Gigahertz electron spin manipulation using voltage-controlled g-tensor modulation. *Science*, 299:1201, 2003.

[95] A. V. Khaetskii, D. Loss, and L. Glazman. Electron spin decoherence in quantum dots due to interaction with nuclei. *Phys. Rev. Lett.*, 88:186802, 2002.

[96] Alexander V. Khaetskii. Spin relaxation in semiconductor mesoscopic systems. *Physica E*, 10:27, 2001.

[97] Alexander V. Khaetskii and Yuli V. Nazarov. Spin relaxation in semiconductor quantum dots. *Phys. Rev. B*, 61(19):12639, 2000.

[98] Alexander V. Khaetskii and Yuli V. Nazarov. Spin-flip transitions between Zeeman sublevels in semiconductor quantum dots. *Phys. Rev. B*, 64:125316, 2001.

[99] D. Klauser, W. A. Coish, and D. Loss. Nuclear spin state narrowing via gate-controlled Rabi oscillations in a double quantum dot. *Phys. Rev. B*, 73:205302, 2006.

[100] W. Knap, C. Skierbiszewski, A. Zduniak, E. Litwin-Staszewska, D. Bertho, F. Kobbi, J. L. Robert, G. E. Pikus, F. G. Pikus, S. V. Iordanskii, V. Mosser, K. Zekentes, and Yu. B. Lyanda-Geller. Weak antilocalization and spin precession in quantum wells. *Phys. Rev. B*, 53:3912, 1996.

[101] P. A. Knipp and T. L. Reinecke. Coupling between electrons and acoustic phonons in semiconductor nanostructures. *Phys. Rev. B*, 52:5923, 1995.

[102] Takaaki Koga, Yoshiaki Sekine, and Junsaku Nitta. Experimental realization of a ballistic spin interferometer based on the Rashba effect using a nanolithographically defined square loop array. *Phys. Rev. B*, 74:41302(R), 2006.

[103] J. Könemann, R. J. Haug, D. K. Maude, V. I Faľko, and B. L. Altshuler. Spin-orbit coupling and anisotropy of spin-splitting in quantum dots. *Phys. Rev. Lett.*, 94:226404, 2005.

[104] F. Koppens. private communication.

[105] F. H. L. Koppens, C. Buizert, K. J. Tielrooij, I. T. Vink, K. C. Nowack, T. Meunier, L. P. Kouwenhoven, and L. M. K. Vandersypen. Driven coherent oscillations of a single electron spin in a quantum dot. *Nature*, 442:766, 2006.

[106] G. F. Koster. *Solid state physics vol. 5.* edited by F. Seitz and D. Turnbull, Academic Press, New York, 1957.

[107] Miro Kroutvar, Yann Ducommun, Dominik Heiss, Max Bichler, Dieter Schuh, Gerhard Absteiter, and Jonathan J. Finley. Optically programmable electron spin memory using semiconductor quantum bits. *Nature*, 432:81, 2004.

[108] W. H. Kuan, C. S. Tang, and W. Xu. Energy levels of a parabolically confined quantum dot in the presence of spin-orbit interaction. *J. Appl. Phys.*, 95:6368, 2004.

[109] C. W. Lai, P. Maletinsky, A. Badolato, and A. Imamoglu. Knight-field-enabled nuclear spin polarization in single quantum dots. *Phys. Rev. Lett.*, 96:167403, 2006.

[110] Xian-Ting Liang. Non-markovian dynamics and phonon decoherence of a double quantum dot charge qubit. *Phys. Rev. B*, 72:245328, 2005.

[111] Y. Y. Liao, Y. N. Chen, D. S. Chuu, and T. Brandes. Spin relaxation in a GaAs quantum dot embedded inside a suspended phonon cavity. *Phys. Rev. B*, 73:85310, 2006.

[112] P. Löwdin. A note on the quantum-mechanical perturbation theory. *J. Chem. Phys.*, 19:1396, 1951.

[113] Y. B. Lyanda-Geller, I. L. Aleiner, and B. L. Altshuler. Coulomb blockade of nuclear spin relaxation in quantum dots. *Phys. Rev. Lett.*, 89:107602, 2002.

[114] G. D. Mahan. *Many-particle Physics*. Kluwer, New York, 2000.

[115] Y. Manassen, R. J. Hamers, J. E. Demuth, and A. J. Castelano, Jr. Direct observation of the precession of individual paramagnetic spins on oxidized silicon surfaces. *Phys. Rev. Lett.*, 62:2531, 1989.

[116] Florian Marquardt and Veniamin A. Abalmassov. Spin relaxation in a quantum dot due to Nyquist noise. *Phys. Rev. B*, 71:165325, 2005.

[117] I. A. Merkulov, Al. L. Efros, and M. Rosen. Electron spin relaxation by nuclei in semiconductor quantum dots. *Phys. Rev. B*, 65:205309, 2002.

[118] T. Meunier, I. T. Vink, L. H. Willems van Beveren, K-J. Tielrooij, R. Hanson, F. H. L. Koppens, H. P. Tranitz, W. Wegscheider, L. P. Kouwenhoven, and L. M. K. Vandersypen. Experimental signature of phonon-mediated spin relaxation. *cond-mat/0609726*, unpublished.

[119] J.B. Miller, D.M. Zumbühl, C.M. Marcus, Y.B. Lyanda-Geller, D. Goldhaber-Gordon, K. Campman, and A.C. Gossard. Gate-controlled spin-orbit quantum interference effects in lateral transport. *Phys. Rev. Lett.*, 90(7):76807, 2003.

[120] G. M. Minkov, A. V. Germanenko, O. E. Rut, A. A. Sherstobitov, L. E. Golub, B. N. Zvonkov, and M. Willander. Weak antilocalization in quantum wells in tilted magnetic fields. *Phys. Rev. B*, 70:155323, 2004.

[121] Warren Nagourney, Jon Sandberg, and Hans Dehmelt. Shelved optical electron amplifier: Observation of a quantum jumps. *Phys. Rev. Lett.*, 56(26):2797, 1986.

[122] J. Nitta, T. Akazaki, H. Takayanagi, and T. Enoki. Gate control of spin-orbit interaction in an inverted InGaAs/InAlAs heterostructure. *Phys. Rev. Lett.*, 78:1335, 1997.

[123] O. Olendski and T. V. Shahbazyan. Anisotropic spin relaxation in quantum dots. *cond-mat/0611065*, unpublished.

[124] K. Ono and S. Tarucha. Nuclear-spin-induced oscillatory current in spin-blockaded quantum dots. *Phys. Rev. Lett.*, 92:256803, 2004.

[125] Masaru Onoda and Naoto Nagaosa. Dynamics of localized spins coupled to the conduction electrons with charge and spin currents. *Phys. Rev. Lett.*, 96:66603, 2006.

[126] T. H. Oosterkamp, T. Fujisawa, W. G. van der Wiel, K. Ishibashi, R. V. Hijman, S. Tarucha, and L. P. Kouwenhoven. Microwave spectroscopy of a quantum-dot molecule. *Nature*, 395:873, 1998.

[127] J. R. Petta, A. C. Johnson, A. Jacoby, C. M. Marcus, M. P. Hanson, and A. C. Gossard. Pulsed-gate measurement of the singlet-triplet relaxation time in a two-electron double quantum dot. *cond-mat/0412048*, unpublished.

[128] J. R. Petta, A. C. Johnson, J. M. Taylor, E. A. Laird, A. Yacoby, M. D. Lukin, C. M. Marcus, M. P. Hanson, and A. C. Gossard. Coherent manipulation of coupled electron spins in semiconductor quatum dots. *Science*, 309:2180, 2005.

[129] P. Pfeffer and W. Zawadzki. Spin splitting of conduction subbands in III-V heterostructures due to inversion asymmetry. *Phys. Rev. B*, 59(8):R5312, 1999.

[130] P. Pfeffer and W. Zawadzki. Theory of spin splitting in GaAlAs parabolic quantum wells controlled by electric field. *Phys. Rev. B*, 72:35325, 2005.

[131] Craig E. Pryor and Michael E. Flatté. Landé g factors and orbital momentum quenching in semiconductor quantum dots. *Phys. Rev. Lett.*, 96:26804, 2006.

[132] S. Rahman, J. Gorman, C. H. W. Barnes, D. A. Williams, and H. P. Langtangen. Finite-element analysis of a silicon-based double quantum dot structure. *Phys, Rev. B*, 73:233307, 2006.

[133] E. I. Rashba. Properties of semiconductors with an extremum loop. 1. cyclotron and combinational resonance in a magnetic field perpendicular to the plane of the loop. *Fiz. Tverd. Tela (Leningrad)*, 2:1224, 1960.

[134] E. I. Rashba and Al. L. Efros. Orbital mechanisms of electron-spin manipulation by an electric field. *Phys. Rev. Lett.*, 91:126405, 2003.

[135] P. Recher, E. V. Sukhorukov, and D. Loss. Quantum dot as spin filter and spin memory. *Phys. Rev. Lett.*, 85:1962, 2000.

[136] D. Rugar, R. Budakian, H. J. Mamin, and B. W. Chui. Single spin detection by magnetic resonance force microscopy. *Nature*, 430:329, 2004.

[137] P. San-Jose, Gergely Zarand, Alexander Shnirman, and Gerd Schön. Geometrical spin dephasing in quantum dots. *Phys. Rev. Lett.*, 97:76803, 2006.

[138] R. Sanchez, E. Cota, R. Aguado, and G. Platero. Spin-filtering through excited states in double-quantum-dot pumps. *Phys. Rev. B*, 74:36326, 2006.

[139] R. Sanchez, G. Platero, R. Aguado, and E. Cota. Photon-assisted tunneling in ac driven quantum dot spin pumps. *Phys. Stat. Sol.*, 203:1154, 2006.

[140] S. Sasaki, T. Fujisawa, T. Hayashi, and Y. Hirayama. Electrical pump-and probe study of spin singlet-triplet relaxation in a quantum dot. *Phys. Rev. Lett.*, 95:056803, 2005.

[141] Y. Sato, T. Kita, S. Gozu, and S. Yamada. Large spontaneous spin splitting in gate-controlled two-dimensional electron gases at normal InGaAs/InAlAs heterojunctions. *J. Appl. Phys.*, 89:8017, 2001.

[142] Y. G. Semenov and K. W. Kim. Phonon-mediated electron spin phase diffusion in a quantum dot. *Phys. Rev. Lett.*, 92:026601, 2004.

[143] T. M. Stace, A. C. Doherty, and S. D. Barrett. Population inversion of a driven two-level system in a structureless bath. *Phys. Rev. Lett.*, 95:106801, 2005.

[144] C. A. Stafford and N. S. Wingreen. Resonant photon-assisted tunneling through a double quantum dot: An electron pump from spatial Rabi oscillations. *Phys. Rev. Lett.*, 76:1916, 1996.

[145] V. N. Stavrou and Xuedong Hu. Charge decoherence in laterally coupled quantum dots due to electron-phonon interaction. *Phys. Rev. B*, 72:075362, 2005.

[146] V. N. Stavrou and Xuedong Hu. Electron relaxation in a double quantum dot through two-phonon processes. *Phys. Rev. B*, 73:205313, 2006.

[147] D. Stepanenko, G. Burkard, G. Giedke, and A. Imamoglu. Enhancement of electron spin coherence by optical preparation of nuclear spins. *Phys. Rev. Lett.*, 96:136401, 2006.

[148] T. H. Stoof and Yu. V. Nazarov. Time-dependent resonant tunneling via two discrete states. *Phys. Rev. B*, 53:1050, 1996.

[149] Charles Tahan, Mark Friesen, and Robert Joynt. Decoherence of electron spin qubits in Si-based quantum computers. *Phys. Rev. B*, 66:35314, 2002.

[150] S. Tarucha, D. G. Austing, T. Honda, R. J. van der Hage, and L. P. Kouwenhoven. Shell filling and spin effects in a few electron quantum dot. *Phys. Rev. Lett.*, 77:3613, 1996.

[151] E. Tsitsishvili, G. S. Lozano, and A. O. Gogolin. Rashba coupling in quantum dots: An exact solution. *Phys. Rev. B*, 70:115316, 2004.

[152] A. V. Tsukanov. Rabi oscillations in the four-level double-dot structure under the influence of the resonant pulse. *Phys. Rev. B*, 73:85308, 2006.

[153] M. Valín-Rodríguez, A. Puente, and L. Serra. Quantum dots based on spin properties of semiconductor heterostructures. *Phys. Rev. B*, 69:153308, 2004.

[154] Manuel Valín-Rodríguez. Renormalization of spin-orbit coupling in quantum dots due to the Zeeman interaction. *Phys. Rev. B*, 70:033306, 2004.

[155] Manuel Valín-Rodríguez, Antonio Puente, and Llorenc Serra. Spin splitting and precession in quantum dots with spin-orbit coupling: The role of spatial deformation. *Phys. Rev. B*, 69:85306, 2004.

[156] Manuel Valín-Rodriguez, Antonio Puente, Llorenc Serra, and Enrico Lipparini. Electronic spin precession in semiconductor quantum dots with spin-orbit coupling. *Phys. Rev. B*, 66:235322, 2002.

[157] W. G. van der Wiel, S. De Franceschi, J. M. Elzerman, T. Fujisawa, S. Tarucha, and L. P. Kouwenhoven. Electron transport through double quantum dots. *Rev. Mod. Phys.*, 75:1, 2003.

[158] J. H. Van Vleck. Paramagnetic relaxation times for titanium and chrome alum. *Phys. Rev.*, 57:426, 1940.

[159] Serguei Vorojtsov, Eduardo R. Mucciolo, and Harold U. Baranger. Phonon decoherence of a double quantum dot charge qubit. *Phys. Rev. B*, 71:205322, 2005.

[160] O. Voskoboynikov, O. Bauga, C. P. Lee, and O. Tretyak. Magnetic properties of parabolic quantum dots in the presence of the spin-orbit interaction. *J. Appl. Phys.*, 94(9):5891, 2003.

[161] O. Voskoboynikov, C. P. Lee, and O. Tretyak. Spin-orbit splitting in semiconductor quantum dots with a parabolic confinement potential. *Phys. Rev. B*, 63:165306, 2001.

[162] Y. Y. Wang and M. W. Wu. Control of spin relaxation in semiconductor double quantum dots. *Phys. Rev. B*, 74:165312, 2006.

[163] W. M. Witzel, R. de Sousa, and S. Das Sarma. Quantum theory of spectral-diffusion-induced electron spin decoherence. *Phys. Rev. B*, 72:161306(R), 2005.

[164] L. M. Woods, T. L. Reinecke, and Y. Lyanda-Geller. Spin relaxation in quantum dots. *Phys. Rev. B*, 66:161318(R), 2002.

[165] W. Yang and K. Chang. Spin relaxation in diluted magnetic semiconductor quantum dots. *Phys. Rev. B*, 72:75303, 2005.

[166] L.-X. Zhang, P. Matagne, J. P. Leburton, R. Hanson, and L. P. Kouwenhoven. Single-electron charging and detection in a laterally coupled quantum-dot circuit in the few-electron regime. *Phys. Rev. B*, 69:245301, 2004.

[167] D. M. Zumbühl, J. B. Miller, C. M. Marcus, D. Goldhaber-Gordon, J. S. Harris, K. Campman, and A. C. Gossard. Conductance fluctuations and partially broken spin symmetries in quantum dots. *Phys. Rev. B*, 72:81305(R), 2005.

[168] I. Žutić, J. Fabian, and S. Das Sarma. Spintronics: fundamentals and applications. *Rev. Mod. Phys.*, 76:323, 2004.